

Rochester Institute of Technology  
**RIT Digital Institutional Repository**

---

[Theses](#)

---

4-1-2007

**Longitudinal dynamic modeling and control of powered parachute aircraft**

John Chambers

Follow this and additional works at: <https://repository.rit.edu/theses>

---

**Recommended Citation**

Chambers, John, "Longitudinal dynamic modeling and control of powered parachute aircraft" (2007).  
Thesis. Rochester Institute of Technology. Accessed from

**LONGITUDINAL DYNAMIC MODELING  
AND CONTROL OF  
POWERED PARACHUTE AIRCRAFT**

By  
**JOHN R. CHAMBERS**

A Thesis Submitted in Partial Fulfillment of the Requirement for  
Master of Science in Mechanical Engineering

Approved by:

*Department of Mechanical Engineering Committee*

**Dr. Kevin Kochersberger** - Thesis Advisor

**Dr. Agamemnon Crassidis**

**Dr. Wayne Walter**

**Dr. Edward Ilense** - Department Representative

**Rochester Institute of Technology**

**Rochester, New York 14623**

**April 2007**

**PERMISSION TO REPRODUCE THE THESIS**

**Title of Thesis**

**LONGITUDINAL MODELING AND CONTROL OF  
POWERED PARACHUTE AIRCRAFT**

I, JOHN R. CHAMBERS, hereby grant permission to the Wallace Memorial Library of Rochester Institute of Technology to reproduce my thesis in the whole or part. Any reproduction will not be for commercial use or profit.

April 2007

# **Abstract**

Powered parachutes (PPC) represent a very unique class of aircraft which have thus far seen limited use beyond recreational flight. Their slow flight and large payload characteristics make them a practical platform for applications such as aerial spraying and surveillance. The portability of the units when not airborne, fast transition to flight readiness, inherent stability, and simplicity of control enhance their appeal for use as Unmanned Aerial Vehicles (UAV).

The aircraft fly using only three control inputs consisting of two steering lines and a throttle for control of climb and descent. One of the more interesting characteristics that distinguish PPC from conventional aircraft is the pendulum stability which is a consequence of suspending the majority of the aircraft weight so far from the wing surface and which introduces an appreciable amount of lag into the system. Another interesting phenomenon is their speed stability which causes the aircraft to fly at a relatively constant speed whether it is climbing, descending, or flying straight-and-level. The current study seeks to examine the effects of throttle on the longitudinal dynamics of PPC, using a small-scale aircraft. A dynamic model has been derived using analytical methods and computer-simulated in MATLAB and Simulink, developed by The Mathworks. The validity of the model was then verified using data recorded from the small-scale PPC. Effects of parameters such as aircraft weight and thrust were examined and related to flight characteristics such as airspeed and climb rate. Finally, a control system was developed to deal with the aforementioned lag and demonstrate accurate altitude-hold capability for a powered parachute.

## **Acknowledgements**

I would like to acknowledge the generous support of the United States Air Force Research Lab (AFRL) at Eglin Air Force Base, Florida in providing the small-scale powered parachute aircraft through Educational Partnership Agreement # 06-086-MN-01. Additionally, I must thank the RIT Mechanical Engineering department for their contribution of data acquisition hardware, and Dr. Kevin Kochersberger for his donation of a parafoil wing. Without their support, I would not have been able to acquire the equipment necessary for my research. I must also thank my family for their unconditional support and encouragement throughout my entire career at RIT; without whom I never could have come so far. Also, in addition to his equipment donation, I must again thank Kevin Kochersberger for his academic advisement and enthusiasm during the entire research process.

# Table of Contents

<b>Abstract .....</b>	<b>ii</b>
<b>Acknowledgements .....</b>	<b>iii</b>
<b>Table of Contents .....</b>	<b>iv</b>
<b>List of Figures .....</b>	<b>vii</b>
<b>List of Tables .....</b>	<b>ix</b>
<b>Nomenclature .....</b>	<b>x</b>
<b>1.0 Introduction .....</b>	<b>1</b>
<b>    1.1 Background and Motivation .....</b>	<b>4</b>
1.1.1 Proposed Uses .....	7
1.1.1.1 Aerial Spraying Applications .....	7
1.1.1.2 High Resolution Photography .....	8
1.1.1.3 Tactical Unmanned Aerial Vehicles .....	8
1.1.1.4 Ground Penetrating Radar .....	9
1.1.1.5 RF Relay .....	9
<b>    1.2 Literature Review .....</b>	<b>10</b>
1.2.1 Autonomous Glided Parafoils .....	10
1.2.2 Unmanned Powered Parachutes .....	17
1.2.3 Parafoil and Control Literature.....	21
<b>    1.3 Objectives of Current Investigation .....</b>	<b>27</b>
<b>2.0 Equipment and Design .....</b>	<b>29</b>
<b>    2.1 Powered Parachute Aircraft .....</b>	<b>29</b>
2.1.1 Small-Scale Powered Parachute Aircraft .....	29

2.1.2 Instrumentation and Data Acquisition .....	31
2.1.3 Propeller Performance and Thrust Characteristics .....	33
2.1.4 Fuselage Drag Measurements .....	35
<b>2.2 Parafoil .....</b>	<b>38</b>
2.2.1 Parafoil Lift and Drag Characteristics .....	40
2.2.1.1 Parafoil Lift.....	41
2.2.1.2 Parafoil Drag.....	42
2.2.1.3 Parafoil L/D Ratio.....	43
<b>3.0 Analytical Dynamic Model .....</b>	<b>45</b>
<b>3.1 General Physical Properties .....</b>	<b>45</b>
3.1.1 General Dimensions and Properties .....	45
3.1.2 Fuselage Moment of Inertia.....	47
3.1.3 Apparent Mass Effects .....	49
3.1.4 Parafoil Moment of Inertia .....	51
3.1.5 Parafoil Performance .....	52
3.1.6 Summary of Physical Properties .....	53
<b>3.2 Simplified Model .....</b>	<b>54</b>
3.2.1 Simplified Model Development .....	54
3.2.2 Adjustment for Sensor Location .....	56
<b>3.3 Full Non-Linear Model .....</b>	<b>58</b>
3.3.1 Advanced Model Development.....	58
<b>4.0 Computer Simulation of Models .....</b>	<b>65</b>
<b>4.1 Simulation Method .....</b>	<b>65</b>
<b>4.2 Simulation Results .....</b>	<b>71</b>
4.2.1 Climb Rate.....	72

4.2.2 Step Input of Thrust .....	74
4.2.2.1 Altitude Response .....	74
4.2.2.2 Speed Response .....	77
<b>5.0 Flight Tests of the Small-Scale Powered Parachute .....</b>	<b>80</b>
<b>5.1 Steady State Flight .....</b>	<b>80</b>
5.1.1 Flight Airspeed .....	80
5.1.2 Climb Rate .....	82
<b>5.2 Step Input of Thrust .....</b>	<b>85</b>
<b>5.3 Comparison of Experimental Data to Analytical Simulation .....</b>	<b>89</b>
5.3.1 Method of Comparison .....	89
5.3.2 Results .....	89
<b>6.0 Control System Development and Simulation .....</b>	<b>95</b>
<b>6.1 Development of Control System .....</b>	<b>95</b>
<b>6.2 Control System Analysis .....</b>	<b>98</b>
<b>7.0 Conclusions .....</b>	<b>103</b>
<b>7.1 General Conclusions .....</b>	<b>103</b>
<b>7.2 Challenges Faced .....</b>	<b>104</b>
<b>7.3 Recommendations for Future Work .....</b>	<b>105</b>
<b>References .....</b>	<b>106</b>
<b>Appendix A: Simulated Thrust Step Response Plots .....</b>	<b>108</b>
<b>Appendix B: Experimental Thrust Step Response Plots .....</b>	<b>120</b>

# List of Figures

Figure 1-1: Typical Powered Parachute Aircraft .....	1
Figure 1-2: Conventional Steering Line Arrangement .....	2
Figure 1-3: “Fly-bar” Steering Arrangement .....	2
Figure 1-4: Illustration of PPC Oscillation Due to Rapid Throttle Increase .....	4
Figure 1-5: NASA X-38 CRV Prototype in Flight Under Parafoil .....	11
Figure 1-6: Modified Buckeye PPC .....	12
Figure 1-7: CQ-10A Snowgoose .....	18
Figure 1-8: Griffon Free Body Diagram .....	19
Figure 1-9: Griffon Thrust vs. Engine RPM Calibration .....	19
Figure 1-10: Griffon in Flight .....	20
Figure 1-11: Parafoil Aerodynamic Properties vs. Angle of Attack .....	24
Figure 1-12: DHL A-300 After TOC Landing .....	25
Figure 1-13: Illustration of MD-11 PCA Using Existing Autopilot for Control Input..	26
Figure 2-1: Small-Scale PPC Fuselage Views .....	30
Figure 2-2: Small-Scale PPC Hand-Launch .....	31
Figure 2-3: Pitot-Static System .....	32
Figure 2-4: RPM Sensor .....	33
Figure 2-5: Powered Parachute Mounted on Wind Tunnel Balance .....	34
Figure 2-6: Small-Scale PPC Thrust Profile .....	35
Figure 2-7: Multiple Tests for Fuselage Drag .....	36
Figure 2-8: Small-Scale PPC Drag Profile with Trendline .....	36
Figure 2-9: Uninflated Parafoil Hanging Inverted .....	38
Figure 2-10: Parafoil in Flight .....	39
Figure 2-11: Parafoil Geometry from Lissaman et. al. ....	39
Figure 3-1: Fuselage CG and Parafoil Connection Point Locations .....	46
Figure 3-2: Rigid Body Simplification .....	54
Figure 3-3: Modeling Axis System .....	55
Figure 3-4: Generalized Coordinates of Advanced Model .....	59
Figure 3-5: Overall Advanced Model .....	60
Figure 4-1: Simulation Axis System .....	65
Figure 4-2: Simulink Block Diagram of PPC Model .....	68
Figure 4-3: Simulink Block Diagram of PPC Model with Sensor Location Correction	70
Figure 4-4: Theoretical Climb Rates .....	72
Figure 4-5: Simulation Climb Rates with 0.25 N Thrust Intervals and Trendline .....	74
Figure 4-6: Altitude Response to Simulated Step Input- Level Flight to Climb .....	75
Figure 4-7: Altitude Response to Simulated Step Input- Descent to Level Flight .....	76
Figure 4-8: Altitude Response to Simulated Step Input- Descent to Climb .....	77
Figure 4-9: Speed Response to Simulated Step Input- Descent to Climb .....	78
Figure 4-10: Speed Response to Simulated Step Input- Level Flight to Zero Thrust ...	78
Figure 5-1: Airspeed During 60 Seconds of Flight .....	81
Figure 5-2: Climb Rate vs. Thrust Graph .....	83
Figure 5-3: Estimation of Sink Rate .....	84
Figure 5-4: Experimental Thrust Step Increase .....	86

Figure 5-5: Experimental Thrust Step Decrease .....	87
Figure 5-6: Experimental vs. Theoretical Climb Rate Comparison .....	90
Figure 5-7: Experimental vs. Theoretical Thrust Step Increase .....	91
Figure 5-8: Experimental vs. Theoretical Thrust Step Decrease .....	92
Figure 6-1: Basis for Control System Development .....	96
Figure 6-2: Simulink Control System Implementation .....	97
Figure 6-3: Controlled Altitude Change from 5 to 7 m .....	99
Figure 6-4: Controlled Altitude Change from 50 to 80 m .....	100
Figure 6-5: Altitude Response to Horizontal Wind Gust .....	101

## List of Tables

Table 3-1: Small-Scale PPC Physical Properties .....	53
Table 4-1: Theoretical Climb Rates .....	73
Table 5-1: Experimental Climb Rate vs. Thrust .....	82

# Nomenclature

AGP- Autonomous Glided Parachute

AOA- Angle of Attack

APP- Autonomous Powered Parachute

CG- Center of Gravity

COTS- Commercial Off The Shelf

DOF- Degree(s) of Freedom

GN&C- Guidance, Navigation, & Control

HMMWV- High Mobility Multipurpose Wheeled Vehicle (synonyms: Humvee)

PCA- Propulsion Controlled Aircraft System

PPC- Powered Parachute (synonyms: Powered Parafoil, Powered Paraglider)

RIT- Rochester Institute of Technology

RPM- Revolutions Per Minute

TOC- Throttles Only Control

UAV- Unmanned Aerial Vehicle

$C_L$ - Coefficient of Lift

$\bar{q}$  - Dynamic Pressure [Pa]

$\rho$ - Air Density [kg/m<sup>3</sup>]

$\gamma$  – Flight Path Angle [radians]

$\theta$ - Pitch Attitude [radians]

L- Lift [N]

$D_f$ - Fuselage Drag [N]

$D_p$ - Parafoil Drag [N]

AR- Aspect Ratio

b- Parafoil Span [m]

c- Parafoil Chord Length [m]

S- Uninflated Parafoil Planform Area [m<sup>2</sup>]

I- Moment of Inertia [kg·m<sup>2</sup>]

m- Mass [kg]

T- Thrust [N]

W- Weight [N]

l- Distance from Parafoil to Overall Aircraft CG [m]

h- Distance from Fuselage CG to Overall Aircraft CG [m]

## **1.0 Introduction**

The *Powered Parachute* (PPC) is an aircraft which derives lift from a ram-air inflated canopy, under which the fuselage is suspended. Their parachutes are inflated by the dynamic pressure of the air flowing past them and have a cross section in the shape of an airfoil, allowing them to create lift. This capability differentiates these “parafoils” from conventional parachutes which are used to simply create drag. Thus far, powered parachutes have been utilized almost exclusively for recreation, but certain properties make them an attractive platform for unmanned aerial vehicle (UAV) and sensing applications.



*Figure 1-1 – Typical Powered Parachute Aircraft*

Powered parachutes have existed in their current form since 1983, when the basic concept was introduced at the Sun & Fun aviation event by the ParaPlane Corporation. They represent aircraft that are somewhere between balloons and fixed wing aircraft when control is considered. Not having conventional control surfaces, the direction of a powered parachute is altered by the pilot pushing on either a left or right steering bar that pulls down on a line attached to the trailing edge of the canopy. The increased drag causes the aircraft to turn, and power must be added to maintain altitude. The

steering bars can also be used in unison, unlike conventional aircraft, which will droop both trailing ends of the canopy together and cause a sudden increase in lift. This maneuver is performed during landing, when the pilot wishes to flare the aircraft to arrest descent rate for a smooth touchdown.

An alternate steering configuration which is used on some small-scale aircraft is known as a “fly-bar.” In



*Figure 1-2 – Conventional Steering Line Arrangement*

this simpler design, the parafoil is connected to the ends of a horizontal bar, as seen in figure 1-3. This bar can be angled toward either side of the aircraft, changing the direction of the lift vector and making the aircraft turn. Using this steering arrangement, it is not possible to

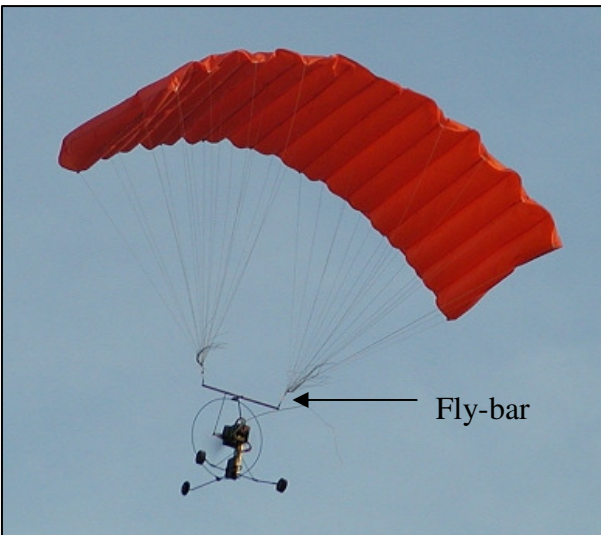


*Figure 1-3 - “Fly-bar” Steering Arrangement*

flare the parachute during landing. Aircraft using each of the two steering systems behave identically in response to thrust inputs; therefore, this investigation of the effects of thrust on longitudinal dynamics will apply to PPC using both steering types.

One very interesting aspect of powered parachutes is their tendency to fly at a constant airspeed. Typical powered parachutes will climb, cruise and descend somewhere around 26 – 32 MPH, and cannot be flown at any other speed. Not only are the aircraft *speed stable*, but they have *pendulum stability* as well, due to the mass of the airframe suspended significantly below the canopy. This allows the aircraft to maintain a safe roll attitude and effectively turn in a coordinated manner when the steering pedals are deflected.

The use of a powered parachute in surveillance and imaging applications has a unique benefit of providing a low-speed, low-cost, and stable platform capable of lifting payloads of up to 600 lbs using COTS technology. Although typically limited to wind speeds of less than 10 MPH, these aircraft are inherently very stable and must only contend with gusts that would disturb a flight trajectory. In an autonomous configuration, the ability to lift a 400 lb. payload is realized in a small, trailerable package that can be set-up and launched by a single person using 500 feet of available runway. Set-up time from trailer to launch configuration is under 15 minutes.

Given the possibilities of using these aircraft in a variety of roles for which they are better suited than conventional fixed-wing airplanes or rotorcraft, this preliminary study of PPC dynamics was deemed necessary. The following sections in this chapter will begin to outline the challenges of PPC longitudinal control, as well as speculate on some potential uses of this technology. Literature related to this topic will be reviewed and the objectives of this investigation will be discussed in greater detail.

## 1.1 Background and Motivation

There are few aircraft other than lighter-than-air vehicles that have the payload carrying capability, short field take-off, and slow speed ranges afforded by a powered parachute. One of the challenges of flying these aircraft is the necessity of controlling altitude with thrust, and direction with asymmetric drag. These controls are not at all common on other aircraft, requiring a new look at air vehicle dynamics to understand how control is manifested. With the large majority of the vehicle mass suspended far below the lifting surface, a pendulum effect is created that induces a large phase lag to control inputs. Additionally, a pendulum oscillation can be introduced by swift, high amplitude throttle inputs, as is roughly illustrated in figure 1-4.

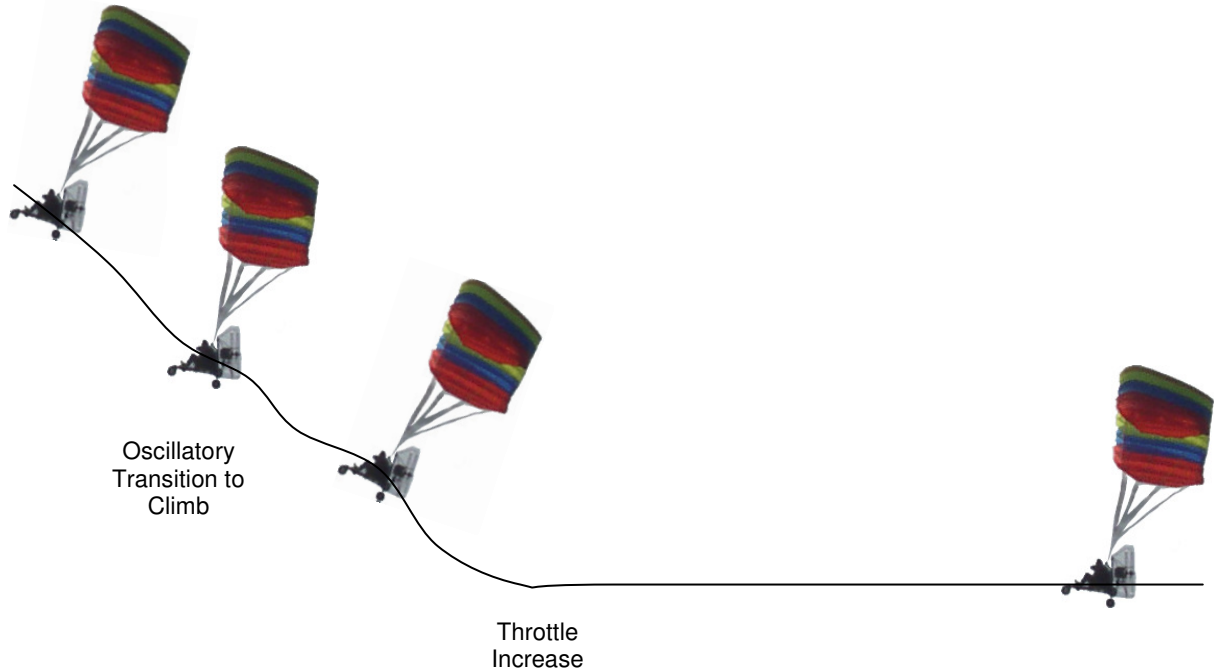


Figure 1-4 – Illustration of PPC Oscillation Due to Rapid Throttle Increase

For successful, controlled flight of a PPC, a unique approach to aircraft modeling must be used. After accurately modeling the vehicle dynamics, a successful control scheme can be implemented that allows the aircraft to maintain altitude by throttle input. Because of the inherent phase lags in the structural dynamics and the tendency of the large mass below the canopy to swing as a pendulum, the challenge to this control scheme will be to accurately measure rates as feedback signals in the control scheme. One-meter altitude resolution is expected when using radar or laser altimetry as the primary vertical position sensor.

Applications that require accurate vertical positioning include crop dusting, high resolution and close range imaging, proximity sensing of targets and detection of substances and organisms that are altitude-specific. The use of radar or laser altimetry combined with barometric sensing can provide the target 1 m accuracy.

A benefit of the powered parachute for unmanned aircraft use is their unique ability to glide to the ground in a relatively safe manner, even if all control systems are disabled. This is particularly desirable in urban environments where a failure of any large UAV would likely result in collateral damage to structures on the ground. Powered parachutes, on the other hand, would be unlikely to land with a vertical speed above 10 mph, making severe damage to any ground edifice or even the airframe itself very unlikely.

These aircraft could provide a robust platform for use in military applications such as low-altitude reconnaissance and bomb damage assessment. The parafoil wing would likely be unaffected by moderate small-arms fire in combat situations. With a small amount of armor

protecting the fuselage, a powered parachute could prove to be a very resilient unmanned aircraft. The nature of these units would allow soldiers to carry man-portable surveillance PPC with the wing folded up and placed inside of a backpack along with the fuselage. Additional uses of powered parachute aircraft have been proposed, and will be addressed in the following section.

### 1.1.1 Proposed Uses

Many uses of powered parachutes have been considered, most of which require the use of the control techniques being developed in this document. The missions outlined below are particularly well suited to powered parachutes, as opposed to conventional fixed-wing aircraft and rotorcraft, due to the PPC's unique flight characteristics.

#### 1.1.1.1 Aerial Spraying

Aerial application, the spraying of various fertilizers and pesticides, is one use for which the powered parachute could prove very useful. The large payload capabilities, coupled with the slow, constant-speed flight of PPC allow for a low-turbulence spraying platform with a long endurance time. Low turbulence operation is particularly useful in electrostatic spraying, in which the sprayed material is given a static charge to aid in deposition on both the upper and lower surfaces of plant leaves [1]. Helicopters have previously been used for electrostatic aerial application because of their low-speed flight abilities, but their rotors produce large amounts of turbulence. Fixed-wing aircraft have also been used for this purpose, but are unable to match the slow flight characteristics of helicopters and PPC. It is surmised that a powered parachute would be able to provide the low speed operation that is unattainable in most fixed-wing aircraft as well as allowing for larger payloads and lower turbulence than rotorcraft.

### 1.1.1.2 High-Resolution Photography

The powered parachute can provide a slow-moving, low altitude platform for use in high-resolution photography. These aircraft are most useful in low wind conditions that can often be found shortly after dawn or just before dusk, though they can withstand some degree of wind. The PPC would fulfill a role somewhere between lighter-than-air vehicles and fixed-wing aircraft by providing a level of stability nearly equal to that of a lighter-than-air vehicle, while retaining more maneuverability and resistance to wind.

### 1.1.1.3 Tactical Unmanned Aerial Vehicles

It has long been the desire of every infantry unit to reconnoiter beyond the next hill without exposing themselves to enemy fire. This dream is quickly becoming a reality with the use of tactical unmanned aerial vehicles that are able to assist land forces in the “Close Battle.” Aircraft such as this are able to support commanders in Urban Operations, Reconnaissance, Surveillance, Target Acquisition (RSTA) Operations and Battle Damage Assessment (BDA) [2]. The light-weight, collapsible wing of a powered parachute would be well suited for such missions, allowing for man-portable units that could be deployed on the battlefield within minutes. Such aircraft would be similar to tactical UAV that have been used by the military in the past, such as the *Pointer* Hand Launched system. This aircraft has a 9 foot wingspan and 6 foot fuselage length, weighing just 8.5 lbs with its payload [2]. A powered parachute of similar capability and payload could be designed to take up far less space when packed and would likely weigh less than its fixed-wing counterpart. In addition, a powered parachute based tactical UAV would likely be far more resilient to small arms fire.

#### 1.1.1.4 Ground Penetrating Radar

Ground penetrating radar (GPR) is an emerging technology that allows operators to observe underground anomalies. Technical advancements in GPR such as the use of Ultra-Wide Bandwidth (UWB) signals could be used to enable GPR imaging from an airborne platform [3]. It has been proposed by some that because of the powered parachute's slow flight abilities and large wing area, a PPC could possibly be used for GPR if an accurate fixed altitude could be maintained. Advancements in PPC control systems and flexible radar antenna usage could allow a powered parachute with a ground penetrating radar system to detect low depth targets such as land mines.

#### 1.1.1.5 Radio Frequency Relay

Because of the low speed flight and high payloads afforded by the powered parachute, it serves as an ideal platform for missions requiring long endurance times such as a radio frequency relay. The PPC is able to retain a virtually static position in low altitude flight with sustained winds less than 10-20 mph. The payload of the aircraft could be customized to each mission by swapping electronic capabilities for increased fuel and endurance time.

## 1.2 Literature Review

While there is very little literature available today that has been written directly on the topics of modeling or control of powered parachutes, there is some information available to aid us in the present study. The literature that is directly related parafoil based UAV can be broken into two categories, the first describes advances in autonomous glided parafoils (AGP), while the second is composed of the few papers that address unmanned powered parachutes. The next two sections in this chapter will outline the work that has been published in these areas.

A third section details other works that may be of some use in PPC modeling and control. This third section includes analyses of parafoil lift, drag, and moment characteristics, as well as information on throttle only control (TOC) of conventional aircraft to be used for comparison purposes.

### 1.2.1 Autonomous Glided Parafoil Literature

Some of the most notable projects to examine glided parafoil dynamics were done for the development of the NASA X-38 crew return vehicle. The project ran from 1995 to 2002, before being cancelled due to budget constraints [4]. The aircraft was to be a lifeboat for the International Space Station, which would deploy a parafoil wing after re-entry and autonomously glide to a designated landing area. Numerous papers have been written to document this work and the many tests which were conducted for the project.

Strahan [5] discusses the results of tests for the autonomous Guidance, Navigation, and Control (GN&C) for the X-38 crew return vehicle. The control algorithms and avionics were utilized on 3 test beds: 1) A modified Buckeye powered parafoil, 2) A “weight tub” that was dropped from another aircraft, and 3) the V131-R, the outer shape of which was virtually identical to

the space recovery vehicle. The main points addressed in the paper are the flight test objectives relating to this GN&C system, a high-level description of the design, and some details of the overall GN&C test results. Issues with radar/laser altimetry are discussed in some detail, as they pertain to use for the triggering of a landing flare.



Figure 1-5 – NASA X-38 CRV Prototype in Flight Under Parafoil

Soppa et al. [6] examine the portions of the X-38 project that were completed by German engineers and the European Space Agency (ESA). This paper goes into some issues not addressed in Strahan's article, which may be pertinent to autonomous PPC design work. More figures are given in this paper, such as wing loading and maximum turn rate. Wing loading figures, in particular, may be very useful for preliminary design of a powered parachute vehicle. Soppa also lists project challenges, performance parameters, and assumptions used. None of this model specific information is particularly applicable to the current work, mainly because his inputs for the longitudinal model are symmetric parafoil trailing-edge deflections, while the input for the present study is throttle position.



Figure 1-6 – Modified Buckeye PPC [7]

Some of the most impressive experimental research regarding the X-38 project was conducted by Hur et. al. [7]. The authors of this paper utilize Texas A & M's modified Buckeye powered parafoil to develop both the longitudinal and lateral/directional models for the vehicle. All forces considered are either inertial or aerodynamic; aircraft thrust is not taken into

account. The authors utilize an 8 degree of freedom system, monitoring 3 positions for the parafoil, 3 attitudes for the parafoil, and 2 DOF for the pitch and yaw motions of the vehicle relative to the parafoil. Relative roll motion between the vehicle and parafoil is ignored.

The Observer/Kalman Filter Identification (OKID) method is used to obtain the dynamic models. As stated in the paper, “OKID is a time domain technique which identifies a discrete input/output mapping from known input data records.” The equations of motion from the ‘Parafoil Dynamic Simulator’ are used to apply OKID to the powered parafoil system. Control inputs are applied simultaneously for longitudinal commands, and differentially for lateral/directional commands. Throttle inputs are not considered in the dynamic models.

In a related paper, Lund [8] details the testing of the same Buckeye powered parafoil which had been modified for use as an unmanned aerial vehicle. The aircraft was developed into a test bed for the parafoil guidance, navigation and control (PGNC) algorithms and sensors designed for the autonomous parafoil recovery of NASA’s X-38 aircraft.

The powered parachute was able to climb to target altitudes where the engine was shut off. Data was then gathered as the aircraft descended during unpowered flight conditions. The system’s specifications and major components were given, however, only a few select test results were included. The authors also made mention of their initial parafoil test methods, without giving many test results in this area either. Additionally, the paper outlined the flight restrictions imposed on the aircraft and mentioned the documents that were prepared in order to obtain a certificate of authorization (COA) from the FAA.

For a broader look at autonomous glided parachutes (AGP), beyond the X-38 project, Hattis and Benney [9] give a general description of the status of AGP, as of 1996. The authors touch briefly on the proposed uses of AGP as well as their performance characteristics. The

body of the paper consists of an in depth analysis of the precision guided airdrop software developed by Draper Laboratory. It focuses on the laboratory's design objectives and challenges, as well as giving an overview of the GN&C system.

Design challenges are listed, including the limited control authority of a parafoil. The author states that the lift-to-drag ratio changes very little with the angle of attack. This would prove to simplify a PPC dynamic model, however the accuracy of this claim becomes suspect when examining the work of Ware and Hassel [10], which will be reviewed in section 1.1.3. The authors also mention the limited longitudinal control afforded to a glided parafoil, a challenge that is alleviated in PPC by the addition of thrust to the aircraft.

Another important design challenge that was mentioned is the lack of availability of off-the-shelf sensors for this type of application. This is, of course, a study into powered parafoil dynamics, not a sensor development project.

One more design challenge cited in the paper is the lack of accurate parafoil dynamics models available in open literature. Hattis and Benney attribute this to both the fundamental non-linearity of parafoil performance characteristics and to the difficulty of collecting good empirical data, except in full scale flight. Draper Labs acquired their raw parafoil data from the Army and NASA before developing their 6 degree-of-freedom canopy models.

One of the shortcomings acknowledged by the authors is that their 6-DOF model did not take relative motions of the canopy and payload into account. If this relative motion is excited to

high amplitude near or within controller bandwidth, it could affect the accuracy of the system. The author goes on to state that these effects would most likely only occur with large parafoils that can produce these high amplitude, low frequency oscillations.

Slegers and Costello [11] develop and test another 6-DOF model for a parafoil-payload system, using a model predictive approach. The authors also fail to take relative motion between the canopy and payload into account, though the model does fare well when compared with experimental data.

Strickert [12], on the other hand, presents a comprehensive study into the relative motions of parafoil and payload. The author uses simulation heavily, incorporating a variety of computer programs to obtain and test the dynamic model of a parachute/payload system. A program called SIMPACK, distributed by a company called INTEC is first used to obtain a mathematical model of the system's characteristics. The Mathworks' MATLAB was then used to simulate the model's response to control inputs. A third computer program called FITLAB was used to compare the simulation to data taken from an experimental parachute system, which was dropped repeatedly. Video cameras were used to monitor the relative motion of the parachute and payload as the platform descended.

The computer model that was developed took relative yaw, roll, pitch, and lateral displacement into account, making it much more complete than most parachute/payload models. The simulation agreed very favorably with experimental results in both its dynamics

and displacement amplitudes. Minor differences between the model and flight test data are attributed to turbulence and gusts, which the model did not take into account.

The computer model also made it possible to “switch off” various aspects of the model to determine their influences. It was found that actuator force contributed to relative yaw the most, while yaw moments of the parafoil and load had less effect, though not negligible.

Strickert goes on to state that because parachute systems vary so much in configuration and geometry, it is unlikely that the results given would be usable for any other applications. Because the simulation was designed in a modular manner, it is possible that the system could be reworked for other applications.

## 1.2.2 Unmanned Powered Parafoil Literature

Very few studies into unmanned powered parachutes have been published thus far. A few papers on working unmanned PPC are described in this section, though none of them share any meaningful insight into the dynamics or control systems of these aircraft.

Messinger [13] briefly introduces his own product, the Remote Aerial Video Assessment Link (RAVAL). The RAVAL is a small powered parachute based UAV with a single radio down-link for transmitting video, navigation, and flight data. The design incorporates a GPS based autopilot and flight control unit with software written in ‘C’. The autopilot controls both heading and altitude, using feedback control loops to adjust throttle position to obtain the desired altitude.

The author gives a list of possible applications for the technology, which include: drug interdiction, border control, communications repeaters and transponders, search and rescue, GPS mapping, and environmental monitoring, among others. He cites the ability to deploy the aircraft from remote locations such as mountainous terrain, the top of a car, or another aircraft as one of its more significant advantages over existing UAV.

The CQ-10A Snowgoose is another autonomously guided, powered parafoil based UAV that was designed for US Special Operations Command. It is meant to be used for leafleting and resupply operations and is operational today. It was designed by Mist Mobility Integrated Systems Technology Inc. (MMIST) of Canada.



*Figure 1-7 – CQ-10A Snowgoose  
Courtesy of MMIST*

The design utilizes three existing COTS systems: 1) MMIST's Sherpa parafoil guidance system, 2) the Rotax 914 UL aircraft engine, and 3) a Performance Designs, Inc. parafoil system. The performance specifications state a 14,000 ft operational ceiling and approximately 550 lb payload. The aircraft can either be ground or air launched, but ground launch requires

the use of a HMMWV [14]. Because the manufacturers of the CQ-10A are under contract with the United States military, few details about the aircraft's specifications and capabilities are available.

Papers by Yamauchi and Rudakevych [15],[16] describe the "Griffon," a man-portable UAV utilizing the "PackBot" ground-mobile robotics platform and a parafoil wing. The Griffon was developed under a phase I small business innovation research (SBIR) project. It weighs 57 pounds, and does not fly autonomously; it is remotely piloted.

The parafoil used is an extreme sports traction kite with slight modifications. The default angle of flight was adjusted, and the kite was converted to a four control-line configuration. The chosen kite was a "Razor," manufactured by Ozone, with a wing area of 11 square meters.

The authors utilized a similar approach to that which will be used in the present research. A simplified free-body diagram, as shown in figure 1-8, was given as the starting point for design of the powered parachute fuselage. Torques were summed about the center of gravity and the motor was placed slightly below the parafoil attachment point, yet well above the center of mass.

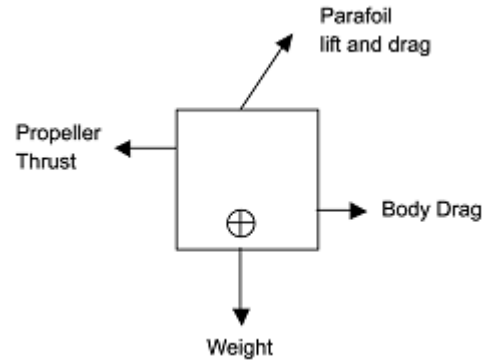


Figure 1-8 – Griffon Free Body Diagram [16]

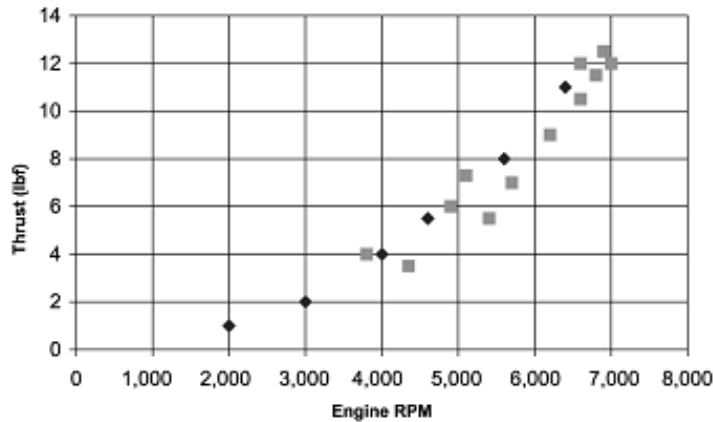


Figure 1-9 – Griffon Thrust vs. Engine RPM Calibration [16]

The aircraft's thrust was measured and plotted against motor RPM, as will be done in the current investigation. The tests presented by Yamauchi were stated to be for verification of adequate thrust to lift the given payload. The testing presented

later in this paper is not only done in a wind tunnel for accurate dynamic thrust measurements, it will be used for comparison of an analytical dynamic model to the measurements taken by our test aircraft's data acquisition system.

The Griffon was flight tested in June of 2003, and achieved an altitude of 200 feet and flight speeds in excess of 20 miles per hour, with a 2.2 HP engine. The author did state that the parafoil wing limits the aircraft's usability in windy conditions.



*Figure 1-10 – Griffon in flight [16]*

No additional information was given on any attempts at control algorithms, nor was any flight test data. Phase II of the SBIR was not funded, so it is unlikely that additional information will be published on this project.

### 1.2.3 Parafoil & Control Literature

Additional literature pertaining to parafoil aerodynamics is useful for the study of powered parachute flight. Reliable aerodynamic data for these types of wings is relatively hard to locate due to the challenges presented in testing a flexible airfoil. The large size of a parafoil and its rigging makes a very large wind tunnel a necessity. Inducing changes in angle-of-attack poses additional problems for experimentation. Information on the leading literature in this area follows, along with basic information on the current state of Throttles-Only-Control (TOC).

Colley [17] outlines the history of parachutes and makes predictions about the future of parafoil development. One of his main focuses is the use of guided parafoils in the military today. The paper serves as a general review of parafoil issues, but does not provide insight into any areas directly pertaining to the current topic.

Iosilevskii [18] examines the longitudinal model for a gliding parachute; more specifically, the response to downward deflections of canopy's trailing edge. The author determines the limits that exist on the location of the center of gravity and the lift coefficient for a gliding parachute as they relate to trailing edge trim.

The model is not particularly useful in our situation because under normal PPC flying conditions, the trailing edge is not manipulated for longitudinal control. On a powered parachute aircraft, throttle input is utilized for this task.

Kalro and Tezduyar [19] present a parallel finite element computational method for three-dimensional analysis of the fluid-structure interaction around a ram-air type parachute. The fluid flow solver is governed by the Navier-Stokes equations for incompressible flows. Two separate iterative techniques are utilized, one more suited to time based analysis, and another which is used for finding steady-state equilibrium characteristics of the system. Two parallel computational methods are used, one for analyzing the flow around the parachute structure, and another for analyzing movements of the canopy structure itself.

A parachute represents a very complex system encompassing interactions between canopy, suspension lines, payload, and the surrounding air. Deformations of the canopy and changes in orientation between the canopy and payload make it necessary to change the shape of the parachute model as time progresses.

If a time based simulation is desired, it is helpful to iterate both the fluid and structure models on the same time scale. If an equilibrium solution is desired, it can be useful to iterate the structural model many more times than the fluid model. This can be done without much extra computational power because of the relative simplicity of the structural model, as compared to that of the fluid.

Future improvements that were stated include better damping models for time-accurate calculations and more realistic models for the parachute fabric.

Ware and Hassel [10] provide some of the most useful information regarding parafoil aerodynamics. The 1969 NASA Technical Memorandum SX-1923 examines ram-air-inflated, flexible parafoils with aspect ratios from 1.0 to 3.0. The authors tested a variety of large scale parafoils of both constant-wing-area and constant-wing-chord series. According to the memorandum, all parafoils were statically, longitudinally, and laterally stable about the confluence point of the suspension lines. The maximum lift-drag ratio obtained was approximately 2.5 when suspension line drag was included. When subtracting suspension line drag, the parafoil L/D ratios ranged from 2.7 to 4.4.

Contrary to one assumption of Hattis and Benney [9], Ware and Hassel provide graphs showing that the lift and drag coefficients, as well as their ratio can change fairly dramatically with relatively small changes in parafoil angle of attack (see figure 1-11). This poses a formidable problem in powered parachute modeling, due to the momentary changes in angle of attack that the aircraft can exhibit during transient dynamic motion. Altering the angle of attack of a parafoil for aerodynamic testing would likely require the skills of a parachute rigger and would make taking measurements a daunting task. The lack of parafoil data resulting from this fact has proven to be the most difficult challenge for the present study to overcome.

Figure 1-10 (below) shows the dramatic changes in lift, drag, and moment properties that can occur with changes in angle-of-attack of only a few degrees. It is useful to note that the equilibrium flight position of a well designed parafoil would be at the angle-of-attack resulting in the greatest L/D ratio. Small AOA changes occurring in this area would likely

result in large changes in the parafoil's aerodynamic coefficients. Figure 1-11 shows aerodynamic coefficients of a parafoil with aspect ratio 2.5 at a velocity of 12.5 m/s, conditions similar to those encountered in flight testing for the current investigation.

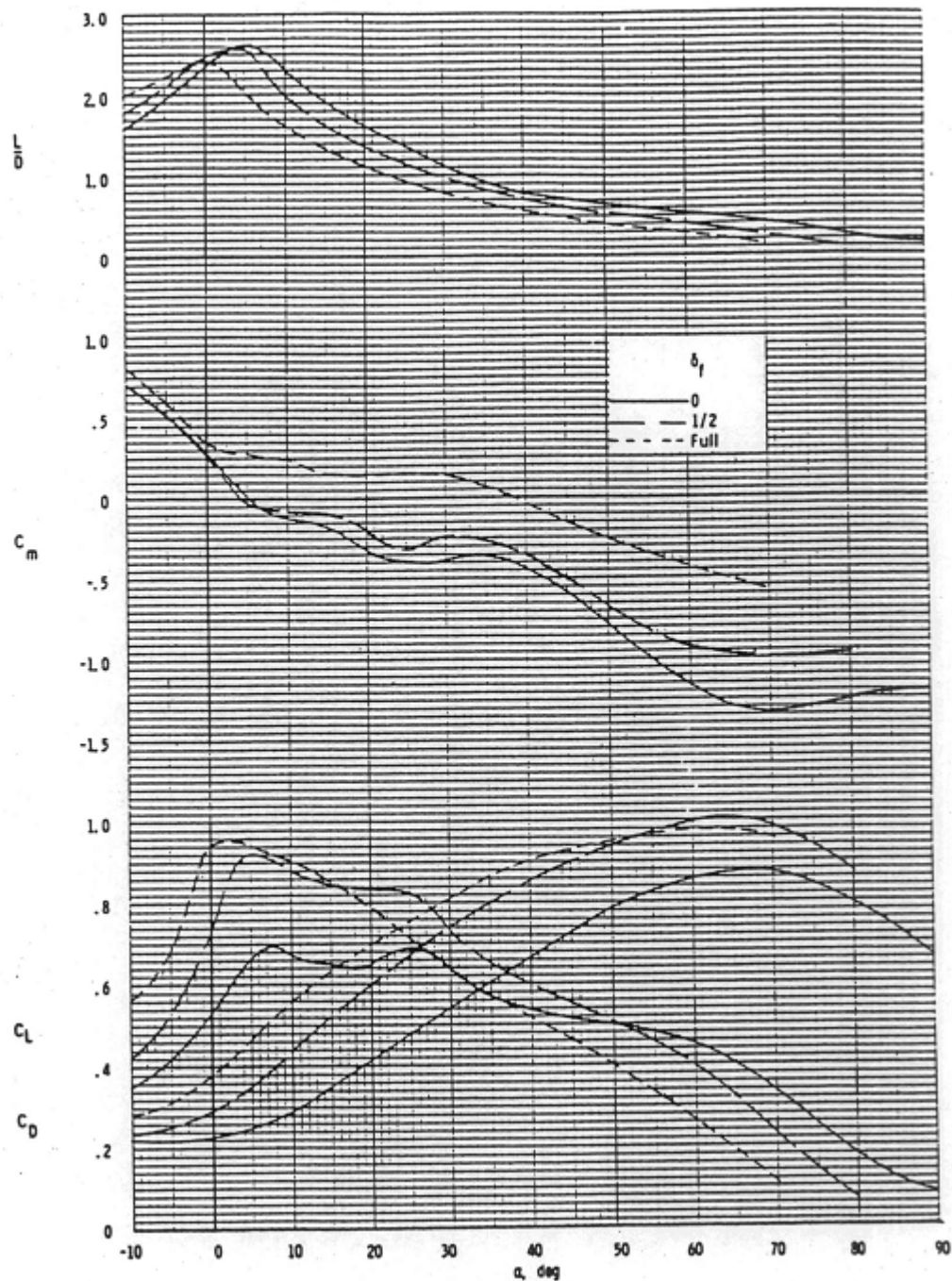


Figure 1-11 – Parafoil Aerodynamic Properties vs. Angle of Attack [10]

Another very important parafoil work is that of Lissaman et. al. [20], in which the topic of parafoil “apparent mass” is discussed. The authors consider theoretical additions to the mass and inertia of a parafoil due to a bubble of air that is carried along when the parachute moves. These effects can be quite important when considering large, lightly loaded bodies such as this, and will be discussed in greater detail in Chapter 3.

The final category of literature to be considered is that which discusses previous work pertaining to Throttles Only Control (TOC). A 2004 INTERpilot article gives a pilot-friendly discussion of TOC for multi-engine aircraft [21]. Figure 1-12 shows an Airbus A-

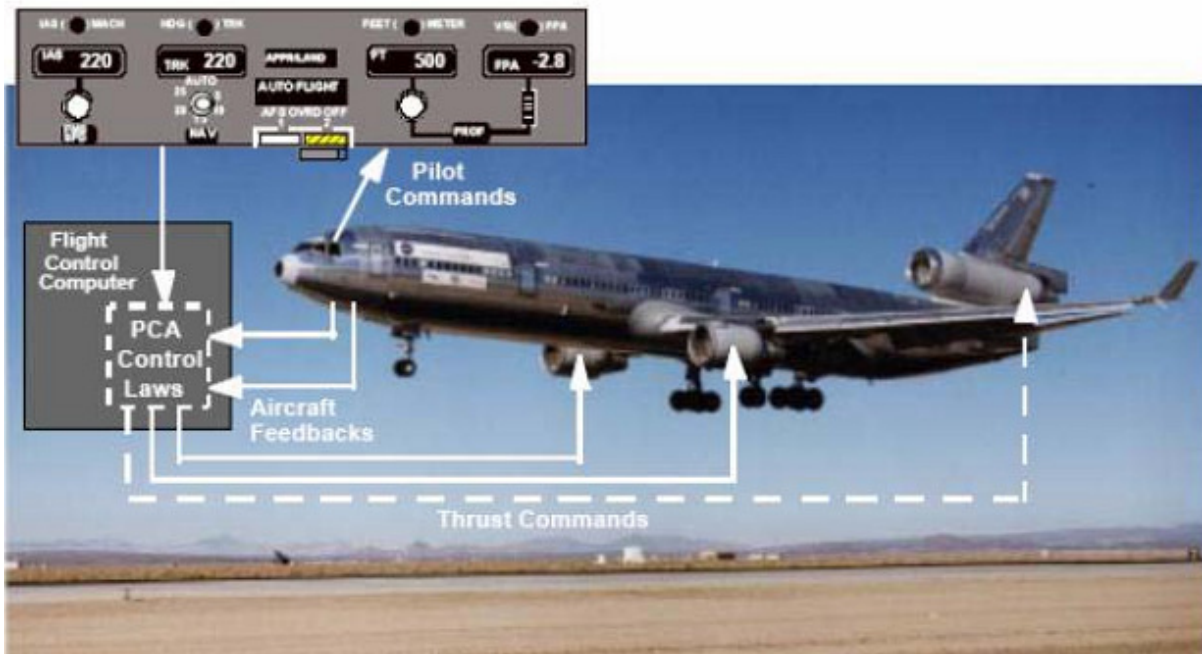


Figure 1-12 – DHL A-300 After TOC Landing [21]

300 that was able to make a safe landing using throttles for control after a missile attack in Baghdad, Iraq. The aircraft was controlled by adjusting the throttles in a rather rudimentary manner to induce pitch, yaw, and roll. The throttles can be used differentially to generate sideslip, which will result in a roll rate through dihedral

effect, according to Burcham et. al.. Pitch control is more complex and includes influences from aircraft speed stability, thrust offset from CG, vertical thrust component, and Phugoid motion [22].

Both TOC articles mention future Propulsion Controlled Flight Systems (PCA) such as the one illustrated in figure 1-13, which successfully piloted an MD-11 using only throttle adjustments through the existing autopilot system.



*Figure 1-13 – Illustration of MD-11 PCA Using Existing Autopilot for Control Input [21]*

TOC of a powered parachute aircraft is far simpler than with a conventional aircraft, as will be shown in this study. PPC are able to maneuver far better than any fixed wing aircraft using changes in thrust for longitudinal control. Accurate altitude manipulation is quite achievable with the unique aircraft configuration that we will be focusing on.

## **1.3 Objectives of Current Investigation**

Many of the applications mentioned in section 1.1.1 require an ability to fly a powered parachute at an accurate altitude above the ground. Since the PPC does not have the conventional control surfaces found on most aircraft, a novel technique must be employed to accurately maintain altitude. The research presented in this paper addresses a longitudinal control system suited for powered parachutes.

Until very recently, the powered parachute was used almost exclusively for recreational purposes. For this reason, there is very little published information characterizing the longitudinal dynamics of these aircraft. There has, however, been considerable research done on lateral/directional control of glided parachutes. Coupling this research with a well developed longitudinal control system would form the basis for a fully autonomous powered parachute with highly accurate control capability.

The current investigation will examine the dynamic characteristics of a small-scale powered parachute in flight, using logged data. Step inputs of thrust and their effect on altitude will be the focus for observation of the dynamic response of these aircraft. Steady-state climb rates at various throttle settings will also be obtained for later comparison against a theoretical dynamic model. Additional testing of this small-scale aircraft in the RIT wind tunnel will allow for calibration of propeller RPM data to the more usable form of dynamic thrust.

In parallel to this experimental investigation, a mathematical dynamic model will be developed using conventional methods of analytical dynamics. Once this model is customized to the specifications of the small-scale aircraft, it will be verified using the data obtained during flight testing. This will be done through simulation using The MathWorks' MATLAB.

After the verification of the validity of the longitudinal model, MATLAB will again be used to simulate a longitudinal control system. The control system will use feedback of the system's dynamic states and will demonstrate accurate altitude-hold capabilities for powered parachute aircraft.

## **2.0 Equipment and Design**

The following sections outline the equipment used for the study of the dynamic behavior of powered parachute aircraft. The main fuselage and data acquisition system are discussed, as is the parafoil wing.

### **2.1 Powered Parachute Aircraft**

This section contains information on the powered parachute fuselage. This represents the heart of the aircraft and requires a good deal of explanation. Section 2.2 will discuss the other major component of the PPC aircraft; the parafoil wing.

#### **2.1.1 Small-Scale PPC Fuselage**

A small-scale powered parachute was adapted for data acquisition purposes. The machine was originally constructed for UAV research at Eglin Air Force Base in Florida and was adapted for its current purpose at the Rochester Institute of Technology. The majority of the original electronics were removed and the steering system was modified to better suit a new parafoil. Data acquisition hardware was added to measure the flight characteristics of the aircraft as well as possible with a small budget.

The aircraft weighs 1.9 kg (4.2 lb) in its flight-ready configuration with an overall height of 1.4 m (55 inches) from the landing gear to the top of the parafoil. The aircraft achieves a flight speed of approximately 7 m/s (15.7 mph) with a maximum sustained climb rate of around 1 m/s (197 ft/min).

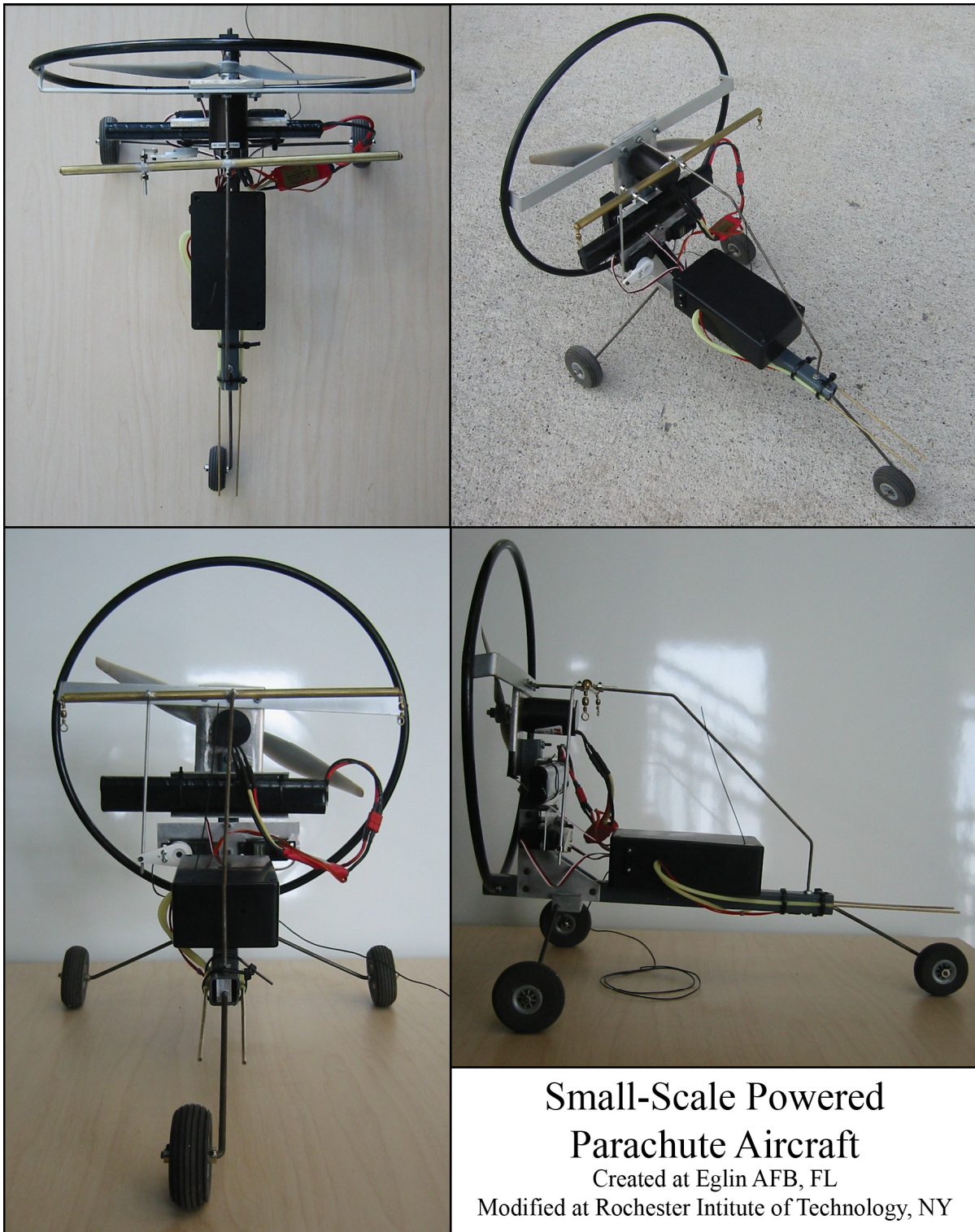


*Figure 2-1 – Small-Scale PPC Fuselage Views*

The model is powered by a 30 amp JETI PHASOR brushless motor with a 30 cm (12 in) propeller. The batteries are 10-cell nickel-metal hydride units with a rated capacity of 1700 mah. This setup afforded a maximum sustainable thrust of approximately 10 N (2.24 lb).

During flight tests, the aircraft was hand-launched and was able to clear a 50 foot obstacle in a horizontal distance of less than 350 feet. Testing consisted of multiple 3-5 minute flights where characteristics such as climb and decent rates were observed. A number of throttle step inputs were also performed using various initial flight conditions. Data was logged to a flight recorder for subsequent analysis.



Figure 2-2 – Small-Scale PPC hand-launch

### 2.1.2 Instrumentation and Data Acquisition

The data acquisition hardware for this project consists of a COTS product manufactured by Eagle Tree Systems of Bellevue, Washington. The “Seagull Pro Wireless Dashboard Flight System” is a small unit with fairly impressive specifications. The unit monitors airspeed, altitude, propeller RPM, temperature, and receiver channels. An additional add-on sensor

was used to monitor G-force in the standard aircraft x- and z-axes (fore-aft and up-down, respectively), to an accuracy of 0.1 G's.

Airspeed was monitored using a pitot-static system that was mounted to the forward beam of the fuselage, above the front landing gear. The brass tubes shown in figure 2-3 allow for measurement of both static and dynamic pressure in the airflow perpendicular to the tubes.

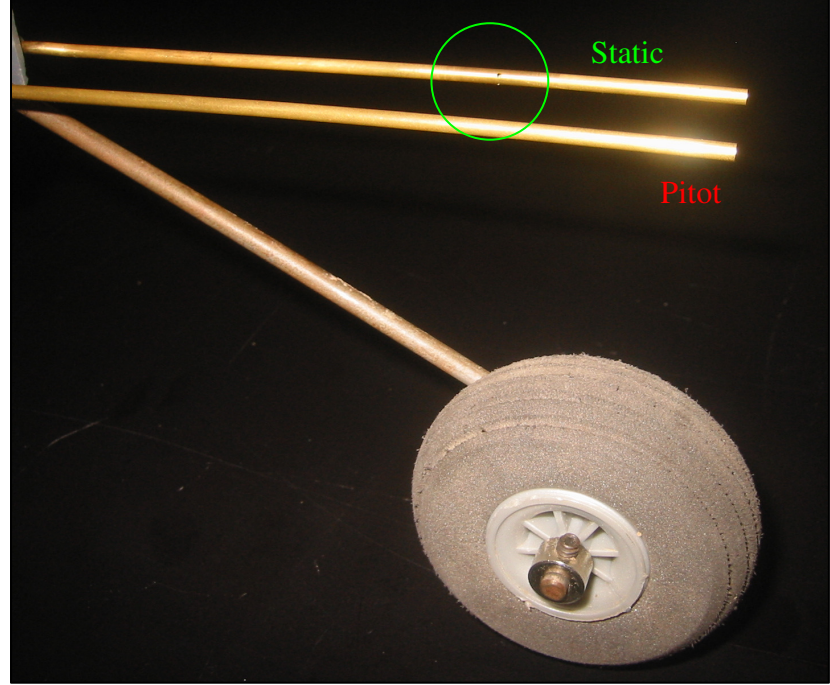


Figure 2-3 – Pitot-Static System

The data acquisition system translates these pressures into airspeed with a resolution of 0.45 m/s (1 mph).

The static pressure measurement is also used to obtain a surprisingly accurate altitude as a differential from the initial altitude when the system is powered up. The resolution of altitude measurements is 0.3 m (1 ft), with an accuracy of approximately 1 m (3.3 ft). Altitude measurements with this level of accuracy are quite impressive for a barometric sensing device.

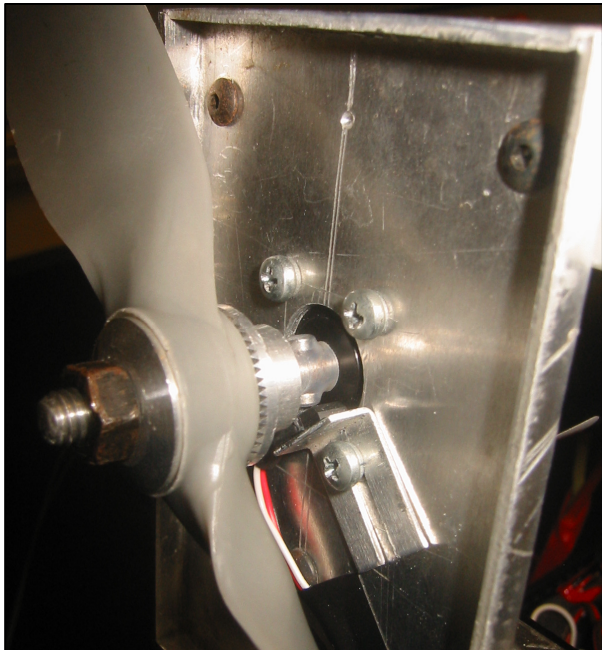


Figure 2-4 – RPM Sensor

Propeller RPM was measured using a magnetic sensor mounted to the propeller shaft itself. The simple sensor counted revolutions using two diametrically opposed magnets on the propeller shaft, as shown in figure 2-4. Because two magnets were mounted at 180 degrees from each other, perfect balance of the propeller was preserved. Propeller RPM measurements were chosen as the simplest and most accurate way to determine thrust.

The temperature sensor was useful for calculating the local air density, allowing for a more accurate flight model. Monitoring of servos was helpful when examining flight data to obtain a better idea of the flight profile and to be sure that the longitudinal flight characteristics were observed only in straight flight.

### 2.1.2 Propeller Performance and Thrust Characteristics

Obtaining propeller performance information was essential to this project so that the RPM data that was logged during flight could be converted into thrust values. *Dynamic thrust data was obtained* in RIT's low speed wind tunnel. The tunnel has a test section that measures 2'x 2'x 4' and is capable of simulating the flight speed of the powered parachute aircraft.

The PPC was mounted to a balance, as shown in figure 2-5. Thrust and drag measurements were accurate to approximately 0.45 N (0.1 lb) using this device. Because the pitot-static system of the flight data recorder was used for wind tunnel velocity measurements, no calibration of airspeed measurements was necessary.

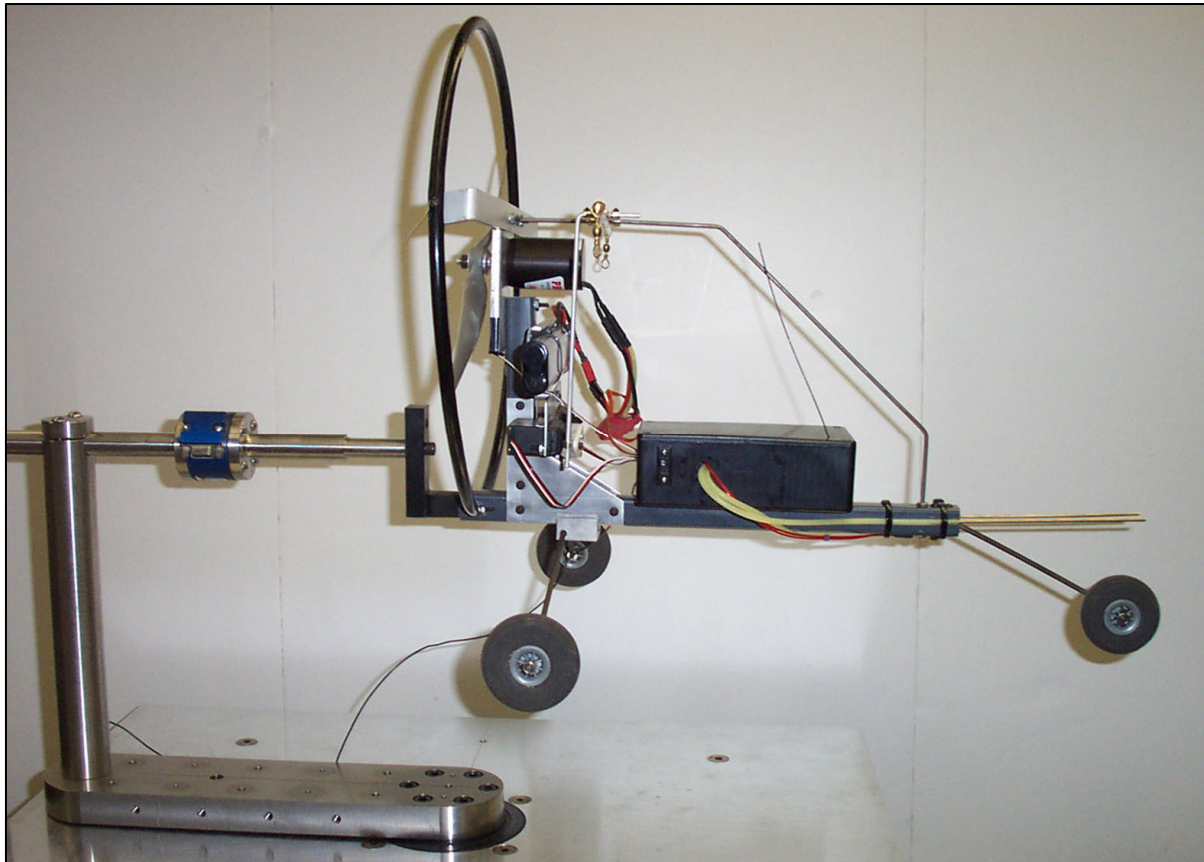


*Figure 2-5 – Powered Parachute Mounted on Wind Tunnel Balance*

A thrust curve was created while the air flowed through the wind tunnel at the constant flight speed that had been observed in previous test flights. A quadratic trendline was fit to the data (see figure 2-6, below), resulting in an equation that could easily convert propeller RPM to thrust, in Newtons:

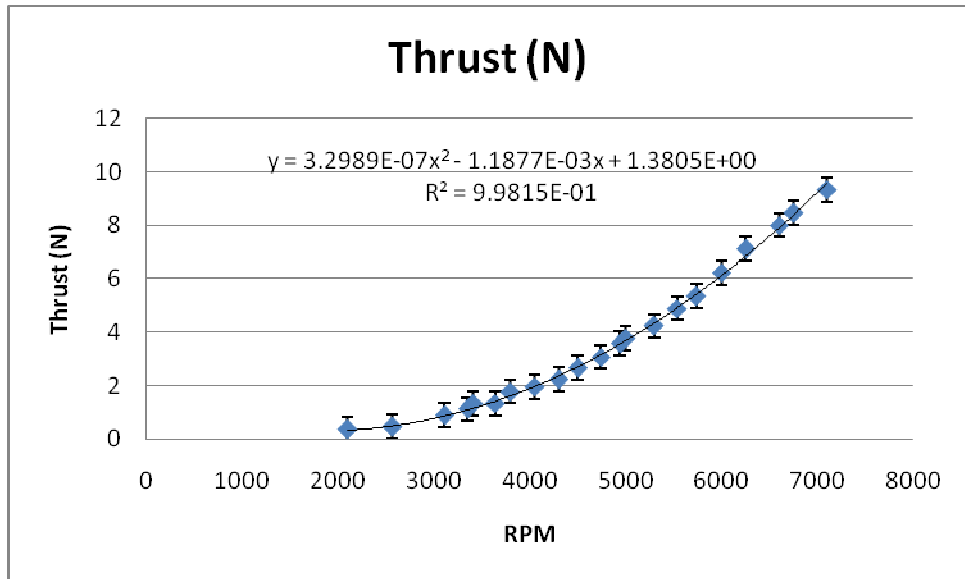


Figure 2-6 – Small-Scale PPC Thrust Profile

$$\text{Thrust (N)} = 3.2989 \times 10^{-7} \cdot \text{RPM}^2 - 1.1877 \times 10^{-3} \cdot \text{RPM} + 1.3805 \quad (\text{eq. 2-1})$$

Again, this represents the actual thrust output of the motor and propeller with the fuselage moving at its steady-state flight speed. This approach was taken because dynamic thrust values are not the same as the static thrust created by a propeller spinning in stationary air.

### 2.1.2 Fuselage Drag Measurements

Fuselage drag measurements were taken at a variety of airspeeds to determine the aerodynamic drag for the fuselage alone. The data obtained in a number of tests agreed favorably, adding to the degree of confidence in our results. Vertical error bars show the uncertainty of the measurement equipment as stated in the previous section.

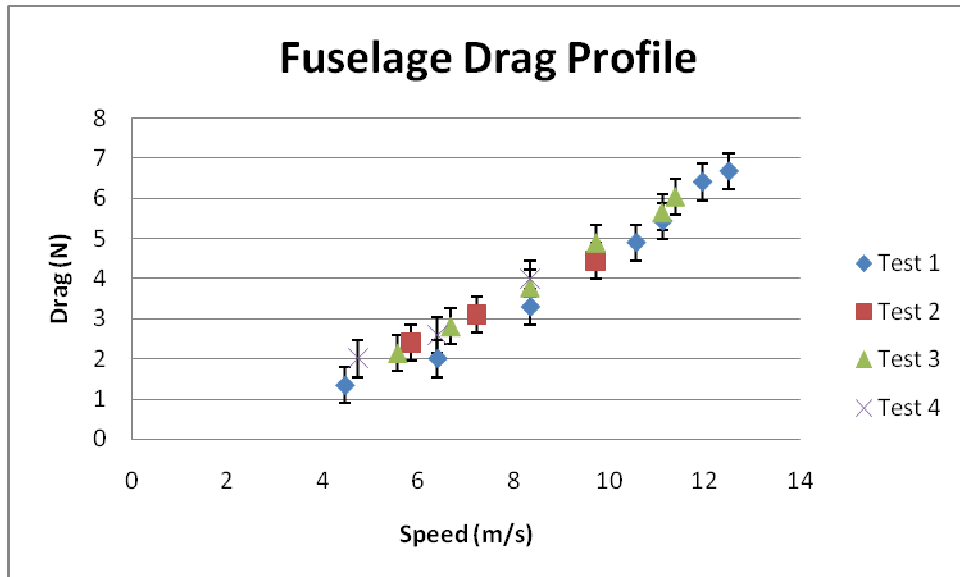


Figure 2-7 – Multiple Tests for Fuselage Drag

After considering the equipment uncertainty, it is clear that the data collected during multiple tests for fuselage drag shows a good degree of precision. By fitting a polynomial to the consolidated data we obtain a relationship for drag as a function of airspeed, as shown in figure 2-8.

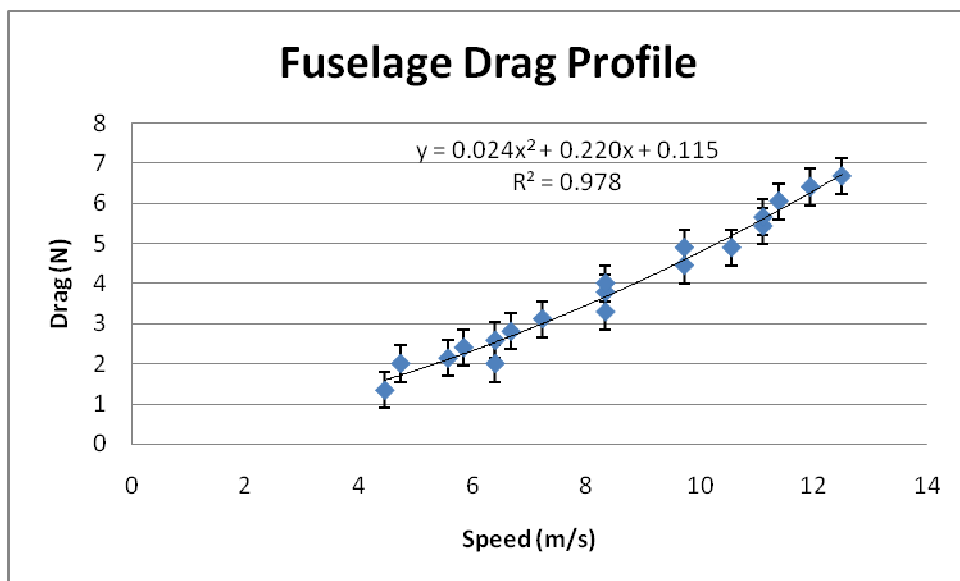


Figure 2-8 – Small-Scale PPC Drag Profile with Trendline

The fuselage drag as a function of airspeed is then equal to:

$$\text{Fuselage Drag (N)} = 0.024 \cdot [\text{Speed(m/s)}]^2 + 0.249 \cdot \text{Speed(m/s)} \quad (\text{eq. 2-2})$$

## 2.2 Parafoil

The parafoil used for experimental research was constructed by Sea Breeze Parachutes of Anna Maria, FL. It is a ram-air-inflated canopy constructed of nylon, with no steering lines. Steering is achieved through the previously mentioned “fly-bar” arrangement.

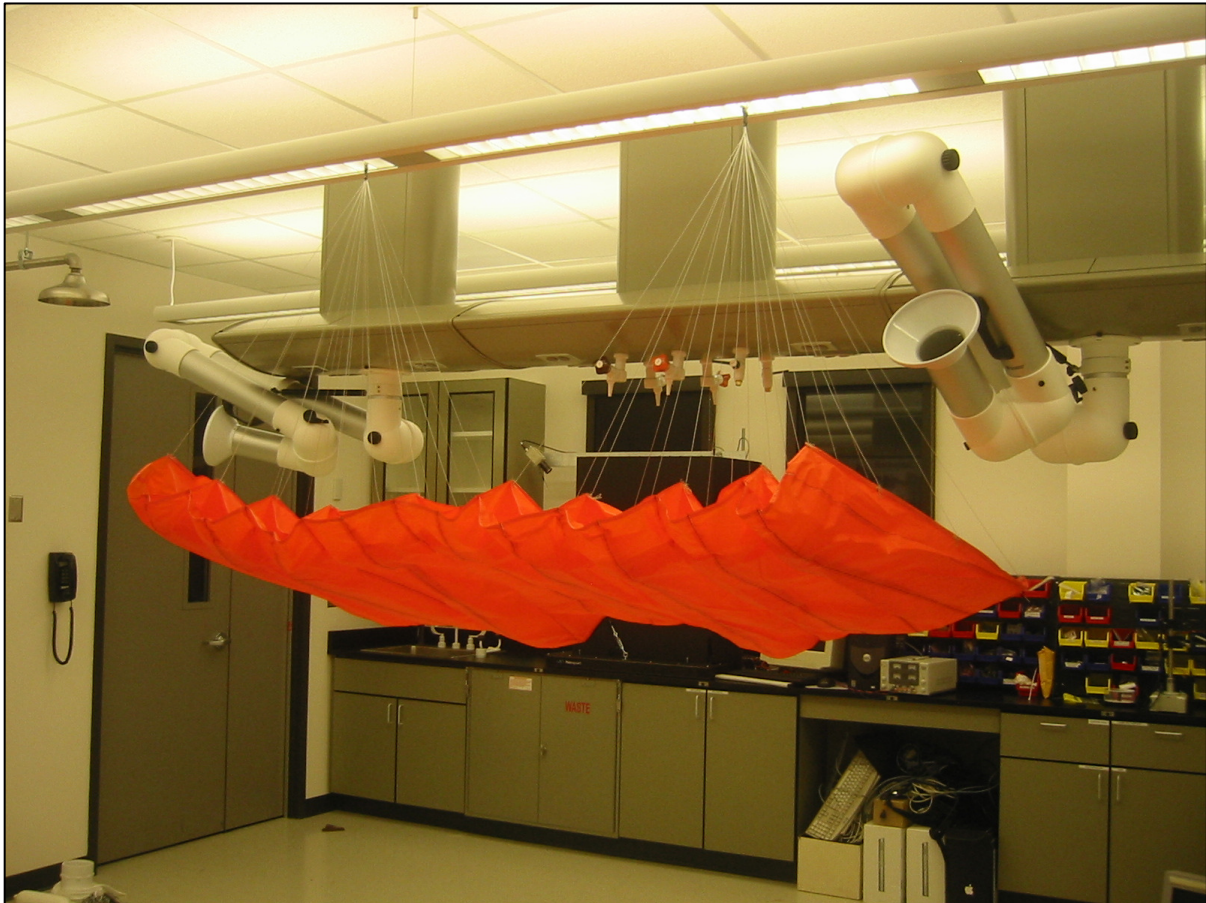


*Figure 2-9 – Uninflated Parafoil Hanging Inverted*

The parafoil has an uninflated span of 2.08 m (82 in), a chord of 0.787 m (31 in), and a planform area of  $2.64 \text{ m}^2$  ( $2,542 \text{ in}^2$ ). The line lengths are approximately 0.914 m (36 in), a value which will be used as an estimate of the distance from the airfoil to the fuselage in later calculations.

Upon inflation of a parafoil wing such as this, the parachute becomes arched quite noticeably (see figure 2-10). This fact tends to decrease the stability of the aircraft, though the stabilizing effects of the PPC's pendulum nature far outweigh the decrease in stability due to anhedral.



Figure 2-10 –Parafoil in Flight

A useful parameter in some parafoil calculations is the arch height of the wing. This can be quantified as the measurement of the height of the center of the wing above the tips, while in flight. For the given parafoil, the arch height is equal to 0.33 m (13 in).

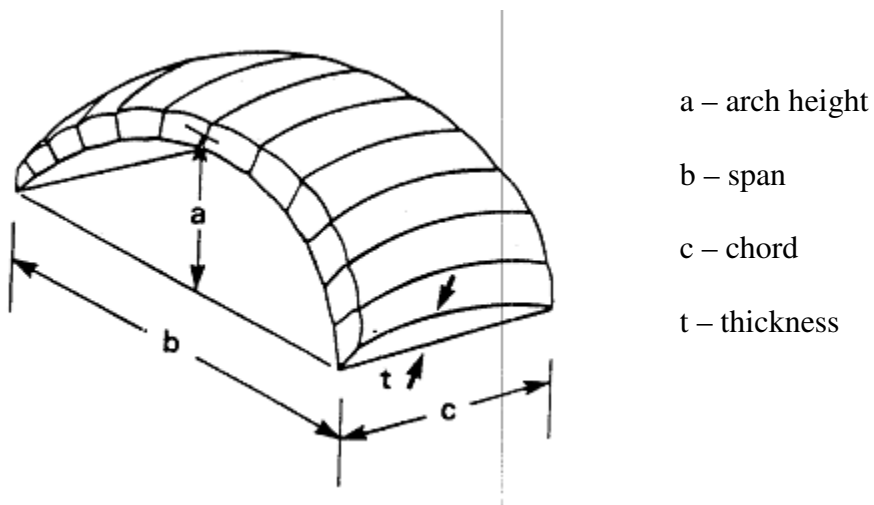


Figure 2-11 –Parafoil Geometry from Lissaman et. al.

The arch height can be converted into a non-dimensional parameter that is useful for some parafoil calculations: the arch-to-span ratio. This parafoil, with an arch measurement of 0.33m and a span of 2.08m has an arch-to-span ratio of 0.16. Lissaman et. al. use an arch-to-span ratio of 0.15 as representative of the majority of conventional parafoils [20].

### 2.2.1 Parafoil Lift and Drag Characteristics

Estimation of the lift and drag characteristics of the parafoil has been the most challenging aspect of this project. Good parafoil data for chutes constructed with different airfoil cross-sections is simply not available. To determine the exact characteristics of this parachute would require a large scale wind tunnel, as well as some very painstaking work in re-rigging the parachute to adjust different angles-of-attack. Additionally, to fully make use of this data would require monitoring the relative motion between the parafoil and canopy during flight testing. While this situation would be ideal, the equipment obtained for this study is simply not up to this task.

It was originally hoped that the lift and drag curves contained in the NASA Technical Memorandum SX-1923 by Ware and Hassell [10], could be used to represent the flight test parafoil. It later became apparent that the parafoil which had been obtained for this project had far different characteristics than those constructed by Ware and Hassel, so a different approach became necessary.

It was decided that general estimates of parafoil lift and drag would have to be used in the simulations developed. Because of the nature of the aircraft, it has been assumed that the angle-of-attack of the parafoil remains constant. Though this assumption may not be entirely accurate for the moments just after a rapid throttle increase, it does represent the parafoil's characteristics fairly well. This is because a parafoil wing tends to "kite" in the wind, quickly changing its position to equalize line tensions and return to its equilibrium state. While this assumption may be slightly detrimental to the model's accuracy just after a large thrust increase, it has proven to represent the parafoil dynamics quite well.

The lift and drag estimates that follow utilize this constant AOA assumption, making parafoil lift and drag functions of airspeed alone.

### 2.2.1.1 Parafoil Lift

Airfoil lift, as given by Anderson [23] is:

$$L = C_L \cdot \bar{q} \cdot A$$

$$\bar{q} = \frac{1}{2} \rho \cdot v^2 \quad (\text{eq. 2-3 \& 2-4})$$

Where L is the lift force,  $C_L$  is the lift coefficient, A is the planform area,  $\rho$  is the air density, and v is the air speed. Equation 2-4 represents the dynamic pressure of the airflow. Because of the previous assumption that the parafoil remains at a constant angle-of-attack, the value of  $C_L$  also remains constant.

We are able to see from equations 2-3 and 2-4 that lift is only a function of airspeed squared, with our constant AOA assumption. The expression for lift can therefore be simplified to contain a single constant representing the other constant values given in equation 2-6.

$$L = K \cdot v^2$$

$$K = \frac{1}{2} \rho \cdot C_L \cdot A \quad (\text{eq. 2-5 \& 2-6})$$

Setting the lift equal to the aircraft weight, and substituting the aircraft's constant flight speed into the equation, we obtain a value of K, thus yielding a simple quadratic equation for lift as a function of airspeed.

$$L = K \cdot v^2$$

$$(9.81 \text{ m/s}^2) \cdot (1.921 \text{ kg}) = K \cdot (7 \text{ m/s})^2 \quad (\text{eq. 2-7})$$

$$K = 0.385 \text{ kg/m}$$

$$L = 0.385 \frac{\text{kg}}{\text{m}} \cdot v^2 \quad (\text{eq. 2-8})$$

### 2.2.1.2 Parafoil Drag

The drag created by the parafoil is equal to the total drag on the aircraft minus the drag created by the fuselage. When in straight and level flight, it is safe to assume that the aircraft's total drag is equal to the thrust of the aircraft, though the forces are in opposite

directions. By subtracting the fuselage drag from the straight and level thrust output, we can obtain an estimate of the drag imparted on the vehicle by the parafoil.

Using a flight speed of 7 m/s and equation 2-2, the drag of the fuselage is equal to:

$$D_f = 0.024 \cdot (7m/s)^2 + 0.249 \cdot (7m/s)$$
$$D_f = 2.05N \quad (\text{eq. 2-9})$$

*The total drag of the aircraft in straight and level flight is 7.32 N, as will be shown in Chapter 5.* By subtracting the fuselage drag from the total drag, we come to a figure of 5.27 N for the drag of the parafoil and lines during straight and level flight. This value can then be used to determine the lift-to-drag ratio of the parafoil.

Determination of parafoil drag for simulation purposes will be done using equation 2-8 in conjunction with the L/D ratio of section 2.2.1.3.

### 2.2.1.3 Parafoil L/D Ratio

Parafoil L/D changes with angle of attack, as shown by Ware and Hassell [10]. Because of our constant AOA assumption, we can calculate the L/D Ratio during straight and level flight and utilize that for other flight conditions. Since we have a fairly good idea of aircraft lift as a function of velocity, we can use the L/D ratio to determine a similar relationship for drag.

The parafoil lift during straight and level flight has already been stated as equal to the total aircraft weight of 18.85 N. In the previous section, the parafoil drag was determined to be 5.27 N. The L/D ratio is then simply computed as:

$$\frac{L}{D} = \frac{18.85N}{5.27N}$$

$$\frac{L}{D} = 3.6 \quad (\text{eq. 2-10})$$

This L/D value is somewhat higher than the parafoils tested in NASA's SX-1923 [10] once line drag is considered, but an L/D ratio of 3.6 is certainly plausible.

Parafoil moment has been neglected because any moment created at the chute simply changes tensions in the parafoil lines, effectively changing the L/D ratio. No moments can be transmitted through the connection between the parafoil and fuselage.

Additionally, the parafoil L/D value of equation 2-10 can be directly related to the kiting angle of the parachute, in the following manner:

$$\text{Kiting } \alpha = \tan^{-1} \left( \frac{L}{D} \right) \quad (\text{eq. 2-11})$$

This represents the angle that the central parachute lines make with the horizon in straight-and-level flight, or with the incident air in other flight conditions.

## **3.0 Analytical Dynamic Model**

Analytical methods were utilized in order to develop a dynamic model to represent the flight of a powered parachute. Some assumptions had to be made in order to develop a model able to represent the complex dynamics of a powered parachute, while still retaining adaptability to different PPC aircraft. Physical properties of the scale-model powered parachute were measured and two different approaches were used to model the system.

### **3.1 General Physical Properties**

This section will outline the determination of various physical parameters for the small-scale powered parachute aircraft. Properties of the aircraft will be established so that flight data can be compared to a simulation of the dynamic model developed later in this chapter.

#### **3.1.1 General Dimensions and Properties**

Many of the physical properties of the small-scale PPC were mentioned in chapter two, and the information that is pertinent to the testing of an analytical model will be restated below.

The mass of the aircraft fuselage is equal to 1.662 kg. Since the aircraft is electrically powered, this mass will remain constant throughout flight. The parafoil canopy has a mass of 0.259 kg. The total physical mass of the aircraft is then 1.921 kg in a flight-ready configuration.

The distance from the center of mass of the fuselage to its parafoil connection point is 0.11 m. The canopy is located an additional 0.91 m above the parafoil connection point. These measurements are shown in figure 3.1, below. The fuselage CG was experimentally located by balancing the aircraft on points that were inline with the center of gravity.

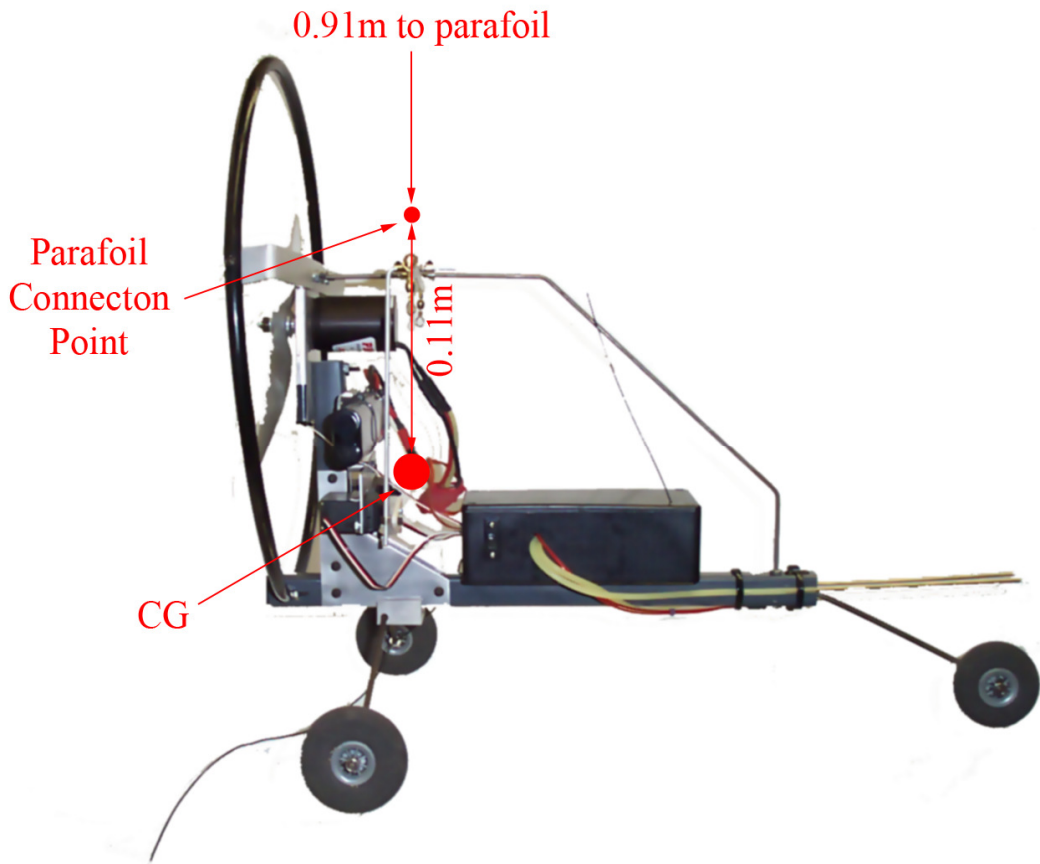


Figure 3.1 –Fuselage CG and Parafoil Connection Point Locations

It is also necessary to determine the location of the overall center-of-gravity of the entire aircraft. This can be determined by treating the system as two point masses, one at the fuselage CG and one at the location of the parafoil, 1.024 m above the fuselage CG. The following equation can be used to determine the position, R, of the overall aircraft CG.

$$R = \frac{1}{M} \sum m_i \cdot r_i \quad (\text{eq. 3-1})$$

Where M is the total mass of the system, and  $m_i$  and  $r_i$  are the masses and positions of the individual system components.

To determine the distance of the aircraft's overall CG from the fuselage CG we need only consider the mass of the parafoil and distance to it from the fuselage CG, along with the entire mass of the aircraft. It should be noted that for this calculation, the total parafoil mass will be used, including the apparent mass effects that will be discussed in section 3.1.3.

$$\begin{aligned} R &= \frac{1}{M} \sum m_i \cdot r_i \\ R &= \frac{1}{1.938 \text{ kg}} (0.276 \text{ kg} \cdot 1.0244 \text{ m}) \\ R &= 0.1459 \text{ m} \end{aligned} \quad (\text{eq. 3-2})$$

This is the distance from the fuselage CG to the overall aircraft CG, denoted on figure 3-2 as h. The distance from the overall aircraft CG to the parafoil, denoted as l in figure 3-2 is then equal to 0.8785 m.

### 3.1.2 Fuselage Moment of Inertia

The moment of inertia of the fuselage is another value that needed to be obtained. This was done by timing the period of the pendulum motion of the fuselage swinging below the parafoil attachment points shown in figure 3-1. This, along with other known measurements,

provides sufficient information to calculate the moment of inertia of the fuselage about these parafoil connection points.

The period of the swinging fuselage was determined by timing 10 full cycles of the pendulum motion and dividing this overall time by 10. This simple experiment was conducted a variety of times to obtain an average period of 0.9876 seconds. The period was then used in the following physical pendulum equation, given by Tipler [24].

$$I = \frac{T^2 \cdot M \cdot g \cdot D}{4\pi^2} \quad (\text{eq. 3-3})$$

Where T is the period, M is the mass, g is the universal gravitational constant, and D is the distance between the center of mass and pivot point

Substituting the values for T, M, g, and D, we obtain the mass moment of inertia of the fuselage about the parafoil connection point.

$$I = \frac{(0.9876s)^2 \cdot (1.6624kg) \cdot (9.81m/s) \cdot 0.11m}{4\pi^2} \quad (\text{eq. 3-4})$$

$$I = 0.04432 \text{ kg}\cdot\text{m}^2$$

The inertia of the fuselage about its center of mass can then be found using the parallel axis theorem, as shown in equation 3-5.

$$\begin{aligned}
 I_{\text{@ connection point}} &= I_{\text{@ fuselage CG}} + M \cdot d^2 \\
 0.04432 \text{ kg-m}^2 &= I_{\text{@ fuselage CG}} + (1.6624 \text{ kg}) \cdot (0.11 \text{ m})^2 \\
 I_{\text{@ fuselage CG}} &= 0.0242 \text{ kg-m}^2
 \end{aligned} \tag{eq. 3-5}$$

This number, again, represents the mass moment of inertia of the fuselage about its own CG, located 0.11 m below the parafoil connection point on the fuselage. From here we can again apply the parallel axis theorem to determine the fuselage moment of inertia about the overall center-of-gravity of the aircraft, which is located 0.146 m above the fuselage CG.

$$\begin{aligned}
 I_{\text{@ overall CG}} &= I_{\text{@ fuselage CG}} + M \cdot d^2 \\
 I_{\text{@ overall CG}} &= (0.0242 \text{ kg-m}^2) + (1.6624 \text{ kg}) \cdot (0.146 \text{ m})^2 \\
 I_{\text{@ overall CG}} &= 0.0596 \text{ kg-m}^2
 \end{aligned} \tag{eq. 3-6}$$

### 3.1.3 Apparent Mass Effects

A large object moving in a fluid tends to carry a certain amount of this fluid along with it. When an object such as a parafoil moves through the air, it brings with it a bubble of air; the mass of which can sometimes be greater than that of the object itself. This phenomenon is known as “apparent mass.” The exact effects of this fluid that is trapped adjacent to the body are very difficult to quantify. There have, however, been attempts at estimating these apparent mass effects that have achieved some degree of accuracy.

Apparent mass, according to Lissaman [20], can have a strong effect on the aerodynamics of lightly loaded flight vehicles, such as parafoils. Through studies, he has developed relationships that yield estimates of mass and inertia components for parafoils which are caused by apparent mass. Because these may affect the dynamics of our powered parachute aircraft, the theoretical mass and inertia components have been calculated below.

Lissaman gives the following equation for the moment of inertia of a parafoil about the y-axis (conventional right-hand aircraft axis system shown in figure 3-3).

$$I_B = \frac{0.038\rho \cdot AR}{1+AR} \left[ 1 + \frac{\pi}{6} (1+AR) \cdot AR \cdot arch^2 \cdot t^2 \right] \cdot c^3 \cdot S \quad (\text{eq. 3-7})$$

Where  $\rho$  is the air density,  $AR$  is the parafoil aspect ratio,  $arch$  is the arch-to-span ratio,  $t$  is the airfoil thickness,  $c$  is the wing chord, and  $S$  is the planform area of the wing.

The arch-to-span ratio for the experimental parafoil is equal to 0.16, as stated in chapter 2. The aspect ratio is equal to 2.65, and the planform area is  $1.64\text{m}^2$ . Substituting these values and standard sea-level air density into the equation given above, we can obtain a value for the moment of inertia of the parafoil due to apparent mass effects.

$$\begin{aligned} I_B &= \frac{0.038 * (1.29\text{kg/m}^3) \cdot 2.65}{1+2.65} \left[ 1 + \frac{\pi}{6} (1+2.65) \cdot 2.65 \cdot (0.16)^2 \cdot (0.1\text{m})^2 \right] \cdot (0.787\text{m})^3 \cdot (1.64\text{m}^2) \\ I_B &= 0.0285 \text{ kg-m}^2 \end{aligned} \quad (\text{eq. 3-8})$$

The added mass that affects motion in the x-z plane can also be computed as shown by Lissaman et. al..

$$\begin{aligned} m_x &= 0.666 \cdot t^2 \cdot b \cdot \rho \\ m_x &= 0.666 \cdot (0.1m)^2 \cdot (2.0828m) \cdot (1.23kg / m^3) \\ m_x &= 0.017 \text{ kg} \end{aligned} \quad (\text{eq. 3-9})$$

This represents the additional “mass” that must be acted upon to induce any forward or vertical acceleration of the aircraft.

### 3.1.4 Parafoil Moment of Inertia

The total moment of inertia of the parafoil is equal to the inertial component due to apparent mass effects plus the physical inertia of the chute. For the physical moment of inertia calculation, the parafoil was treated as if it were a flat plate rotated about its centroid. The physical moment of inertia of the parafoil was then calculated using equation 3-10, where m and c represent the mass and chord length of the parafoil.

$$\begin{aligned} I &= \frac{m \cdot c^2}{12} \\ I &= \frac{(0.254 \text{ kg}) \cdot (0.787m)^2}{12} \\ I &= 0.0131 \text{ kg-m}^2 \end{aligned} \quad (\text{eq. 3-10})$$

Summing the physical and apparent inertias of the parafoil about its own CG yields a value of  $0.0416 \text{ kg-m}^2$ . From here, we can employ the parallel axis theorem to determine the moment of inertia of the parafoil when rotated about the overall aircraft CG.

$$\begin{aligned} I_{\text{@ overall}}_{\text{CG}} &= I_{\text{@ parafoil}}_{\text{CG}} + M \cdot d^2 \\ I_{\text{@ overall}}_{\text{CG}} &= (0.0416 \text{ kg-m}^2) + (0.276 \text{ kg}) \cdot (0.87851 \text{ m})^2 \\ I_{\text{@ overall}}_{\text{CG}} &= 0.2841 \text{ kg-m}^2 \end{aligned} \quad (\text{eq. 3-11})$$

### 3.1.5 Parafoil Performance

The properties of the parafoil were examined in Section 2.2. The lift and drag characteristics that will be used for simulation of our dynamic model are reiterated below:

$$L = 0.385 \cdot v^2 \quad (\text{eq. 3-12})$$

$$\frac{L}{D} = 3.6 \quad (\text{eq. 3-13})$$

Using these two equations, we can calculate the parafoil drag in the following manner:

$$\begin{aligned} D &= \frac{0.385 \cdot v^2}{3.6} \\ D &= 0.107 \cdot v^2 \end{aligned} \quad (\text{eq. 3.14})$$

### 3.1.6 Summary of Physical Properties

In summary, the physical properties of the small-scale powered parachute are given below:

Fuselage Mass	1.662 kg
Parafoil Mass	0.259 kg
Total Physical Mass	1.921 kg
Apparent Mass	0.017 kg
Theoretical Total mass	1.938 kg
Fuselage Inertia @ Parafoil Attachment	0.0443 kg·m <sup>2</sup>
Fuselage Inertia @ Fuselage CG	0.0242 kg·m <sup>2</sup>
Fuselage Inertia @ Overall Aircraft CG	0.0596 kg·m <sup>2</sup>
Apparent Inertia of Parafoil @ Parafoil CG	0.0285 kg·m <sup>2</sup>
Physical Inertia of Parafoil @ Parafoil CG	0.0131 kg·m <sup>2</sup>
Total Parafoil Inertia @ Parafoil CG	0.0416 kg·m <sup>2</sup>
Total Parafoil Inertia @ Overall Aircraft CG	0.2841 kg·m <sup>2</sup>
Total Aircraft Moment of Inertia @ Overall Aircraft CG	0.3437 kg·m <sup>2</sup>
Distance from Parafoil CG to Fuselage CG	1.024 m
Distance from Parafoil CG to Overall Aircraft CG (l)	0.8785 m
Distance from Fuselage CG to Overall Aircraft CG (h)	0.1459 m

*Chart 3.1 –Small-Scale PPC Physical Properties*

## 3.2 Simplified Model

Because of the complexity of this nonlinear system, it is advantageous to make a number of simplifications to the model to so that simulation and control analysis are more straightforward. One such simplification is to assume that the entire aircraft behaves as a rigid body, thus treating it like a conventional aircraft with the wing positioned high above the fuselage. A further simplification beyond this would be to neglect all parafoil dynamics and simply transpose the lift and drag vectors from the parafoil to the fuselage itself. Because this simplification would be useful only for climb rate data and would not address the periodic motion of the aircraft, only the rigid body assumption was tested.

### 3.2.1 Simplified model Development

One simplification of the dynamics of a powered parachute is to treat the entire aircraft like a rigid body. This assumes that the parafoil remains at a constant position in relation to the fuselage.

Additionally, it is assumed that the thrust vector remains in a constant relationship to the pitch attitude of the entire aircraft,  $\theta$ . The direction of the lift and drag are determined by the flight path angle,  $\gamma$ .

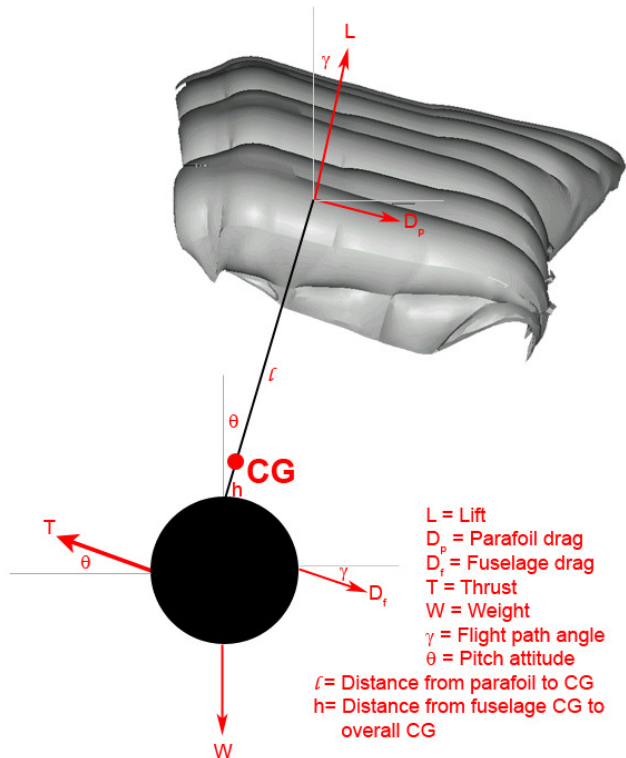
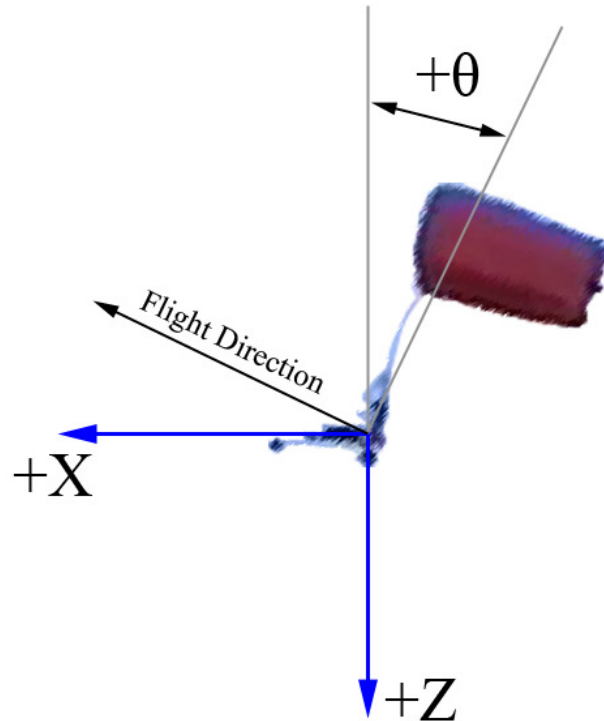


Figure 3-2 – Rigid Body Simplification

A standard aircraft axis system will be used in the derivation of the equations of motion, as shown below:



*Figure 3-3 – Modeling Axis System*

Using this axis system, the flight path angle,  $\gamma$ , is equal to:

$$\gamma = \tan^{-1} \left( \frac{\dot{z}}{\dot{x}} \right) \quad (\text{eq. 3-15})$$

The use of this model still allows for simple pendulum motion of the entire aircraft and has potential to represent the aircraft dynamics with a good degree of accuracy. Examination of

video footage of powered parachutes in flight shows that this estimation is fairly typical of these aircraft under normal flight conditions.

The equations of motion of the aircraft can be derived by summing the forces and moments shown in figure 3-2:

$$\sum F_x = T \cdot \cos(\theta) - [D_f + D_p] \cdot \cos(\gamma) - L \cdot \sin(\gamma) = m \cdot \ddot{x} \quad (\text{eq. 3-16})$$

$$\sum F_z = W + [D_f + D_p] \cdot \sin(\gamma) - T \cdot \sin(\theta) - L \cdot \cos(\gamma) = m \cdot \ddot{z} \quad (\text{eq. 3-17})$$

$$\begin{aligned} \sum_{\text{clockwise} = +} M_{CG} &= h \cdot [T - W \cdot \sin(\theta) - D_f \cdot \cos(\gamma - \theta)] + \\ &+ l \cdot [D_p \cdot \cos(\gamma - \theta) + L \cdot \sin(\gamma - \theta)] = I_{CG} \cdot \ddot{\theta} \end{aligned} \quad (\text{eq. 3-18})$$

The subscript ‘CG’ in equation 3-18 denotes the summation of moment and inertia about the overall aircraft center of gravity. The lift and drag are derived from calculations made in earlier sections.

### 3.2.2 Adjustment for Sensor Location

The equations of motion in section 3.2.1 describe the movement of the CG of the entire aircraft, which is located slightly above the main fuselage. In most cases it is useful to translate the motion of the overall CG into motion at the fuselage, which is often the location of the aircraft’s sensors. This can be done fairly simply, first by determining the changes in displacement in the x- and z-directions which are due to changes in angular displacement. It

is then possible to translate the point at which we will calculate accelerations. Since this is a rigid body, these acceleration components will be functions of theta alone.

$$\begin{aligned}\Delta x &= hs \cdot \sin(\theta) \\ \Delta z &= -hs \cdot [1 - \cos(\theta)]\end{aligned}\quad (\text{eq. 3-19 \& 3-20})$$

These equations relate angular displacement to the resulting changes in linear displacement. The constant,  $hs$ , represents the vertical distance from the aircraft CG to the sensors in the fuselage, which in our case is equal to 0.20 m. The time derivatives of these equations are then taken to determine the effects of the aircraft's angular motion on the linear velocity and acceleration of the fuselage.

$$\begin{aligned}\Delta \dot{x} &= hs \cdot \cos(\theta) \cdot \dot{\theta} \\ \Delta \ddot{x} &= hs \cdot \cos(\theta) \cdot \ddot{\theta} - hs \cdot \sin(\theta) \cdot \dot{\theta}^2\end{aligned}\quad (\text{eq. 3-21 \& 3-22})$$

$$\begin{aligned}\Delta \dot{z} &= -hs \cdot \sin(\theta) \cdot \dot{\theta} \\ \Delta \ddot{z} &= -hs \cdot \sin(\theta) \cdot \ddot{\theta} - hs \cdot \cos(\theta) \cdot \dot{\theta}^2\end{aligned}\quad (\text{eq. 3-23 \& 3-24})$$

During simulation, these effects can be added to the respective displacement, velocity, and acceleration terms computed for the overall center of gravity of the aircraft.

### **3.3 Full Nonlinear Model**

This section outlines the development of a 4 degree-of-freedom model that has potential to accurately represent the dynamics of powered parachutes with any fuselage configuration. Though the simplified model of section 3.2 will be shown to represent the dynamics of our experimental model with a good degree of accuracy, it may not accurately represent all aircraft of this type. If the thrust line is located sufficiently far from the fuselage CG, especially below it, thrust inputs may result in a larger degree of relative motion between the fuselage and parafoil. Also, aircraft utilizing long parafoil risers may be more accurately represented using a model such as this, though the simplified model may suffice for both of these cases.

It must be noted that the development of this model is somewhat incomplete and it has not been validated through simulation. It has, however, been included because this model represents the next logical step in highly accurate longitudinal control of PPC with adaptability to any aircraft of this type.

#### **3.3.1 Advanced Model Development**

It was determined that a 4 degree-of-freedom model might yield a more accurate representation of the longitudinal dynamics of this aircraft in some circumstances. In this model, two translational DOF refer to the position of the connection point between the parafoil lines and fuselage or risers. Two additional rotational DOF refer to the angular positions of the parafoil lines and the riser/body system. The motion of each of the two

major bodies composing the aircraft, the fuselage and parafoil, can be described using Lagrange's Equation and these four general coordinates.

Figure 3-4 shows the generalized coordinates for the derivation of Lagrange's equations of motion:

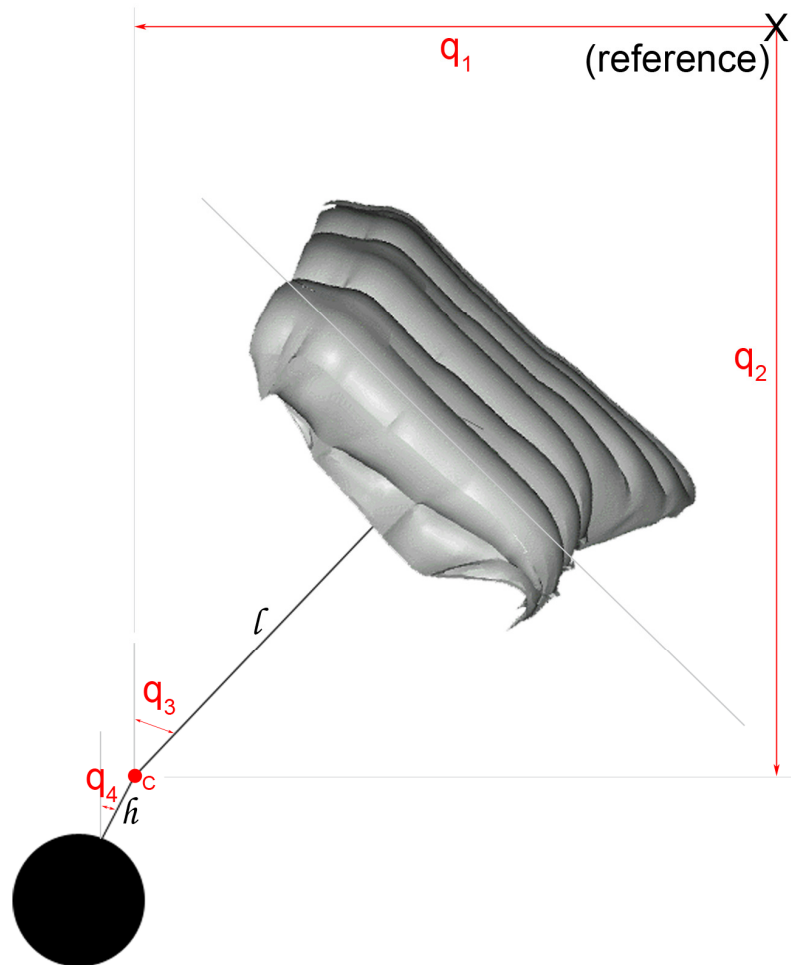


Figure 3-4 – Generalized Coordinates of Advanced Model

The overall model, including external forces is shown below, in figure 3-5:

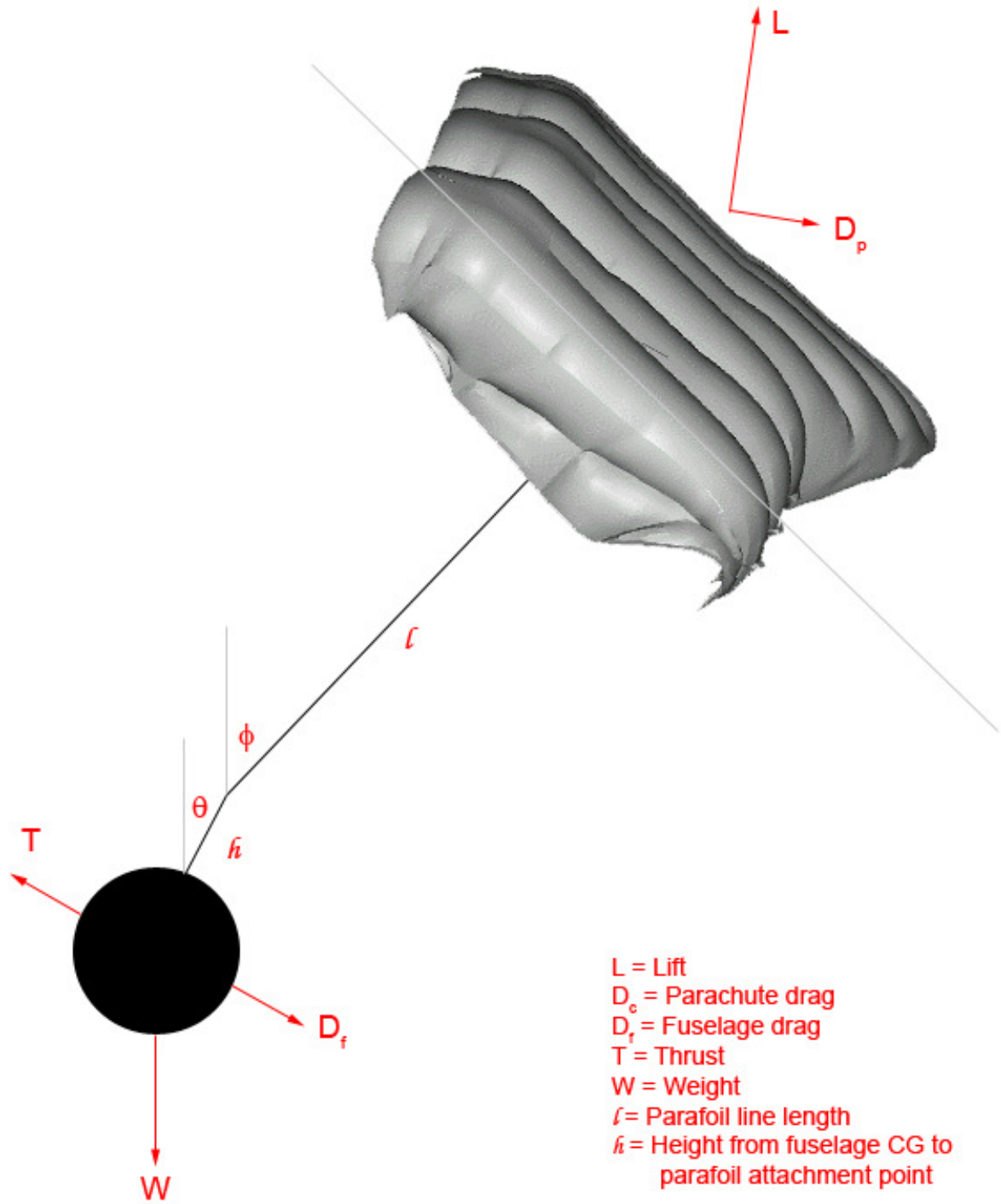


Figure 3-5 – Overall Advanced Model

Derivation of the equations of motion was done in the following manner:

The position vectors pointing to the parafoil and fuselage,  $\mathbf{r}_p$  and  $\mathbf{r}_f$  respectively, were defined using the general coordinates as follows:

$$\begin{aligned}\mathbf{r}_p &= [q_1 - l \cdot \sin(q_3)]\mathbf{i} + [q_2 - l \cdot \cos(q_3)]\mathbf{k} \\ \mathbf{r}_f &= [q_1 + h \cdot \sin(q_4)]\mathbf{i} + [q_2 + h \cdot \cos(q_4)]\mathbf{k}\end{aligned}\quad (\text{eq. 3-25 \& 3-26})$$

These vectors were then used to obtain the kinetic energy of the system, as described by Meirovitch [25].

$$\dot{\mathbf{r}}_i = \frac{d\mathbf{r}_i}{dt} = \frac{\partial \mathbf{r}_i}{\partial q_1} \dot{q}_1 + \frac{\partial \mathbf{r}_i}{\partial q_2} \dot{q}_2 + \frac{\partial \mathbf{r}_i}{\partial q_3} \dot{q}_3 + \frac{\partial \mathbf{r}_i}{\partial q_4} \dot{q}_4 + \frac{\partial \mathbf{r}_i}{\partial t} \quad (\text{eq. 3-27})$$

$$\begin{aligned}\dot{\mathbf{r}}_p &= (\dot{q}_1)\mathbf{i} + (\dot{q}_2)\mathbf{k} + (-l \cdot \cos(q_3) \cdot \dot{q}_3)\mathbf{i} + (l \cdot \sin(q_3) \cdot \dot{q}_3)\mathbf{k} \\ \boxed{\dot{\mathbf{r}}_p &= [\dot{q}_1 - l \cdot \cos(q_3) \cdot \dot{q}_3]\mathbf{i} + [\dot{q}_2 + l \cdot \sin(q_3) \cdot \dot{q}_3]\mathbf{k}}\end{aligned}\quad (\text{eq. 3-28})$$

$$\begin{aligned}\dot{\mathbf{r}}_f &= (\dot{q}_1)\mathbf{i} + (\dot{q}_2)\mathbf{k} + (h \cdot \cos(q_4) \cdot \dot{q}_4)\mathbf{i} + (-h \cdot \sin(q_4) \cdot \dot{q}_4)\mathbf{k} \\ \boxed{\dot{\mathbf{r}}_f &= [\dot{q}_1 + h \cdot \cos(q_4) \cdot \dot{q}_4]\mathbf{i} + [\dot{q}_2 - h \cdot \sin(q_4) \cdot \dot{q}_4]\mathbf{k}}\end{aligned}\quad (\text{eq. 3-29})$$

The kinetic energy is then:

$$T = \frac{1}{2} [m_{pt}(\dot{\mathbf{r}}_p \cdot \dot{\mathbf{r}}_p) + m_f(\dot{\mathbf{r}}_f \cdot \dot{\mathbf{r}}_f)] \quad (\text{eq. 3-30})$$

where  $m_{pt}$  is the total mass of the parafoil wing *including apparent mass effects*.

After computing the dot products in equation 3-30, we obtain:

$$\begin{aligned}
 T &= \frac{1}{2} \left[ m_{pt} \{ [(\dot{q}_1 - l \cdot \cos(q_3) \cdot \dot{q}_3) i + (\dot{q}_2 + l \cdot \sin(q_3) \cdot \dot{q}_3) k] \cdot [(\dot{q}_1 - l \cdot \cos(q_3) \cdot \dot{q}_3) i + (\dot{q}_2 + l \cdot \sin(q_3) \cdot \dot{q}_3) k] \} + \right. \\
 &\quad \left. + m_f \{ [(\dot{q}_1 + h \cdot \cos(q_4) \cdot \dot{q}_4) i + (\dot{q}_2 - h \cdot \sin(q_4) \cdot \dot{q}_4) k] \cdot [(\dot{q}_1 + h \cdot \cos(q_4) \cdot \dot{q}_4) i + (\dot{q}_2 - h \cdot \sin(q_4) \cdot \dot{q}_4) k] \} \right] \\
 T &= \frac{1}{2} \left[ m_{pt} \{ (\dot{q}_1)^2 + (\dot{q}_2)^2 + l^2 \cdot (\dot{q}_3)^2 - 2 \cdot l \cdot \dot{q}_1 \cdot \dot{q}_3 \cdot \cos(q_3) + 2 \cdot l \cdot \dot{q}_2 \cdot \dot{q}_3 \cdot \sin(q_3) \} + \right. \\
 &\quad \left. + m_f \{ (\dot{q}_1)^2 + (\dot{q}_2)^2 + h^2 \cdot (\dot{q}_4)^2 + 2 \cdot h \cdot \dot{q}_1 \cdot \dot{q}_4 \cdot \cos(q_4) - 2 \cdot h \cdot \dot{q}_2 \cdot \dot{q}_4 \cdot \sin(q_4) \} \right]
 \end{aligned} \tag{eq. 3-31}$$

The potential energy of the system,  $V$ , is:

$$V = -(m_f + m_p) \cdot g \cdot [q_2 - h \cdot \sin(q_4)] \tag{eq. 3-32}$$

Where  $m_p$  is the physical mass of the parafoil and  $g$  is the universal gravitational constant.

The Lagrangian, which is equal to  $T - V$ , is then:

$$\begin{aligned}
 L &= \frac{1}{2} \left[ m_{pt} \{ (\dot{q}_1)^2 + (\dot{q}_2)^2 + l^2 \cdot (\dot{q}_3)^2 - 2 \cdot l \cdot \dot{q}_1 \cdot \dot{q}_3 \cdot \cos(q_3) + 2 \cdot l \cdot \dot{q}_2 \cdot \dot{q}_3 \cdot \sin(q_3) \} + \right. \\
 &\quad \left. + m_f \{ (\dot{q}_1)^2 + (\dot{q}_2)^2 + h^2 \cdot (\dot{q}_4)^2 + 2 \cdot h \cdot \dot{q}_1 \cdot \dot{q}_4 \cdot \cos(q_4) - 2 \cdot h \cdot \dot{q}_2 \cdot \dot{q}_4 \cdot \sin(q_4) \} \right] + (m_f + m_p) \cdot g \cdot [q_2 - h \sin(q_4)]
 \end{aligned} \tag{eq. 3-33}$$

The non-potential forces existing in the system are thrust, lift, and aerodynamic drag. The non-potential force terms of Lagrange's equations of motion were found by computing the forces and moments influencing the 4 generalized coordinates. These non-potential force terms were computed as:

$$\begin{aligned}
Q_1 &= -D_c \cos(q_3) - L \sin(q_3) - D_f \cos(q_4) + T \cos(q_4) \\
Q_2 &= W + D_c \sin(q_3) - L \cos(q_3) + D_f \sin(q_4) - T \sin(q_4) \\
Q_3 &= l \cdot [D_p \cos(q_3 - \gamma_p) - L \sin(q_3 - \gamma_p)] \\
Q_4 &= h \cdot [T - D_f \cos(q_4 - \gamma_f)]
\end{aligned} \tag{eq. 3-34 – 3-37}$$

Four simultaneous differential equations can be obtained by computing the following:

$$\frac{d}{dt} \left( \frac{\partial L}{\partial \dot{q}_k} \right) - \frac{\partial L}{\partial q_k} = Q_k \tag{eq. 3-38}$$

After taking the derivatives of the Lagrangian as outlined by Meirovitch, the following equations of motion are obtained:

$$\begin{aligned}
m_{pt} [\ddot{q}_1 - l \cdot \ddot{q}_3 \cos(q_3) + l(\dot{q}_3)^2 \sin(q_3)] + m_f [\ddot{q}_1 + h \cdot \ddot{q}_4 \cos(q_4) - h(\dot{q}_4)^2 \sin(q_4)] &= \\
&= -D_p \cos(\gamma_p) - L \sin(\gamma_p) - D_f \cos(\gamma_f) + T \cos(q_4) \\
m_{pt} [\ddot{q}_2 + l \cdot \ddot{q}_3 \sin(q_3) + l(\dot{q}_3)^2 \cos(q_3)] + m_f [\ddot{q}_2 - h \cdot \ddot{q}_4 \sin(q_4) - h(\dot{q}_4)^2 \cos(q_4)] - (m_f + m_p) g &= \\
&= D_p \sin(\gamma_p) - L \cos(\gamma_p) + D_f \sin(\gamma_f) - T \sin(q_4) \\
m_{pt} [l^2 \ddot{q}_3 - l \cdot \ddot{q}_1 \cos(q_3) + l \cdot \ddot{q}_2 \sin(q_3)] &= \\
&= l [D_p \cos(q_3 - \gamma_p) - L \sin(q_3 - \gamma_p)] \\
m_f [h^2 \ddot{q}_4 + h \cdot \ddot{q}_1 \cos(q_4) - h \cdot \ddot{q}_2 \sin(q_4)] + (m_f + m_p) g \cdot h \sin(q_4) &= \\
&= h [T - D_f \cos(q_4 - \gamma_f)] \tag{eq. 3-39 – 3-42}
\end{aligned}$$

At this point, we have four coupled equations of motion for the system. It may be possible to program these equations into Simulink and run a simulation, allowing MATLAB to estimate

the solutions of the algebraic loops resulting from the equations. A more desirable technique would be to use Lagrange multipliers to effectively introduce additional, false degrees of freedom to the system. In this manner, the equations may be decoupled and simulated more accurately.

Both of these approaches have become beyond the scope of this project. It is not possible to truly evaluate the accuracy of this type of dynamic model without having additional parafoil data as well as the capability of monitoring relative motion between the canopy and fuselage during flight tests.

The simplified dynamic model developed in section 3.2 will be shown to yield a very acceptable representation the flight of our test aircraft, as is expected for most powered parachutes. For these reasons, development of this model has been taken no further. This incomplete and untested model may, however, prove useful for further study into powered parachute flight dynamics.

## **4.0 Computer Simulation of Models**

### **4.1 Simulation Method**

The simplified powered parachute dynamic model of section 3.2 was simulated using MATLAB and Simulink. The ODE45 function was utilized to evaluate the differential equations developed. The equations of motion were also used in a Simulink “Embedded MATLAB Function” block. The same axis system that was used for the derivation of the analytical model was used for the simulation:

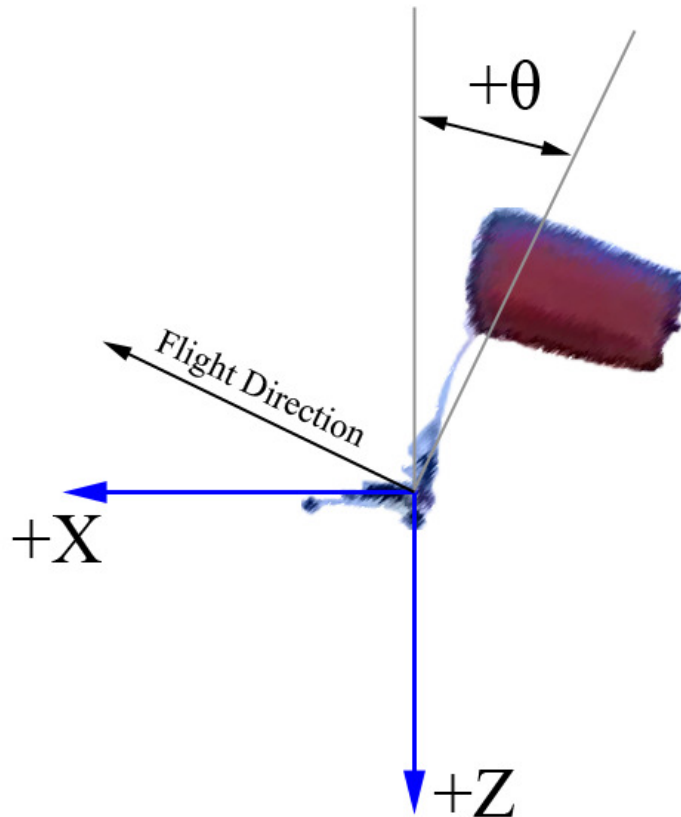


*Figure 4-1 – Simulation Axis System*

The State vectors used in the simulation are given below:

$$q = \begin{bmatrix} x \\ \dot{x} \\ z \\ \dot{z} \\ \theta \\ \dot{\theta} \end{bmatrix} \quad (\text{eq. 4-1})$$

$$\dot{q} = \begin{bmatrix} \dot{x} \\ \ddot{x} \\ \dot{z} \\ \ddot{z} \\ \dot{\theta} \\ \ddot{\theta} \end{bmatrix}$$

A MATLAB function named ‘ppcsim.m’ is used to form the dynamic model simulation by outlining the equations of motion developed in section 3.2.

```

function qdot=ppcsim(t,q)

%T is a constant thrust input
T=9.31; %Thrust [N]

m=1.938; %Total Aircraft Mass [kg] (includes apparent mass)
g=9.81; %Gravitational Constant [m/s^2]
W=m*g; %Aircraft Weight [N]
l=0.8785; %Distance from Parafoil C/4 to Overall Aircraft CG [m]
h=0.1459; %Distance from Fuselage CG to Overall Aircraft CG [m]
I=0.3437; %Aircraft moment of inertia @ CG [kg-m^2] (includes apparent inertia)

L=.385*(q(2)^2+q(4)^2); %Lift [N]
Dp=L/3.6; %Parafoil Drag [N]
Df=0.024*(q(2)^2+q(4)^2)+0.249*sqrt(q(2)^2+q(4)^2); %Fuselage Drag [N]

a=q(2); %X-dot [m/s]
c=q(4); %Z-dot [m/s]
```

```

e=q(6); %Theta-dot [radian/s]

gamma=-atan(q(4)/q(2)); %Climb angle [radians]

b=(T*cos(q(5))-Df*Dp)*cos(gamma)-L*sin(gamma))/m; %X-dot-dot [m/s^2]
d=(W+(Df+Dp)*sin(gamma)-T*sin(q(5))-L*cos(gamma))/m; %Z-dot-dot [m/s^2]
f=(h*(T-W*sin(q(5))-Df*cos((gamma)-q(5)))+l*(Dp*cos((gamma)-q(5))+L*sin((gamma)-q(5))))/I;
%Theta-dot-dot [radian/s^2]

qdot=[a;b;c;d;e;f];

```

An additional m-file, named ‘simulate’, is used to run the ODE45 solver to simulate a flight condition:

```
[t,q]=ode45('ppcsim',[Time Span],[Initial q]);
```

The function is used to simulate aircraft flight using a constant thrust input that is given in the ‘ppcsim.m’ m-file. This can be used to find steady-state flight characteristics such as climb rate, or can be used to simulate a thrust step input. To simulate a thrust step input, the initial constant thrust input was run for a considerably long time span of a few minutes. Steady state values were then obtained for the state vector, and were then used as the initial conditions for a simulation with a different constant throttle setting.

Alternatively, an ‘Embedded MATLAB Function’ block can be used in Simulink with a slightly modified version of the code above. This approach can be more useful in some situations and allows for much easier control analysis. This Simulink block diagram for the model is shown in figure 4-2.

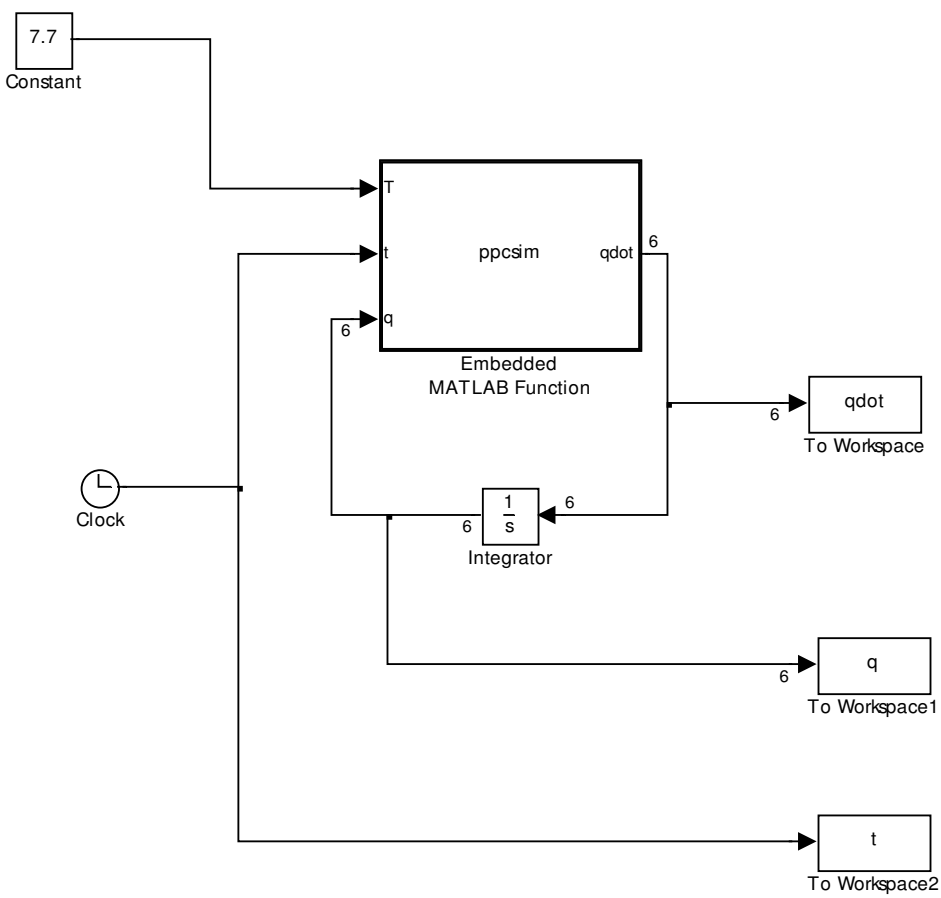


Figure 4-2 –Simulink Block Diagram of PPC Model

The code used in the ‘Embedded MATLAB Function’ block is shown below:

```

function qdot=ppcsim(T,t,q)

m=1.938; %Total Aircraft Mass [kg] (includes apparent mass)
g=9.81; %Gravitational Constant [m/s^2]
W=m*g; %Aircraft Weight [N]
l=0.8785; %Distance from Parafoil C/4 to Overall Aircraft CG [m]
h=0.1459; %Distance from Fuselage CG to Overall Aircraft CG [m]
I=0.3437; %Aircraft moment of inertia @ CG [kg-m^2] (includes apparent inertia)

```

```

L=.385*(q(2)^2+q(4)^2); %Lift [N]
Dp=L/3.6; %Parafoil Drag [N]
Df=0.024*(q(2)^2+q(4)^2)+0.249*sqrt(q(2)^2+q(4)^2); %Fuselage Drag [N]

a=q(2); %X-dot [m/s]
c=q(4); %Z-dot [m/s]
e=q(6); %Theta-dot [radian/s]

gamma=-atan(q(4)/q(2)); %Climb angle [radians]

b=(T*cos(q(5))-(Df+Dp)*cos(gamma)-L*sin(gamma))/m; %X-dot-dot [m/s^2]
d=(W+(Df+Dp)*sin(gamma)-T*sin(q(5))-L*cos(gamma))/m; %Z-dot-dot [m/s^2]
f=(h*(T-W*sin(q(5))-Df*cos((gamma)-q(5)))+l*(Dp*cos((gamma)-q(5))+L*sin((gamma)-q(5)))/I;
%Theta-dot-dot [radian/s^2]

qdot=[a;b;c;d;e;f];

```

This Simulink modeling approach also allows for easier inclusion of the effects of the sensor location into the model. Additional ‘Embedded MATLAB Function’ blocks can be added to translate the q and qdot values obtained for the aircraft CG into position, velocity, and acceleration values at the actual sensor location.

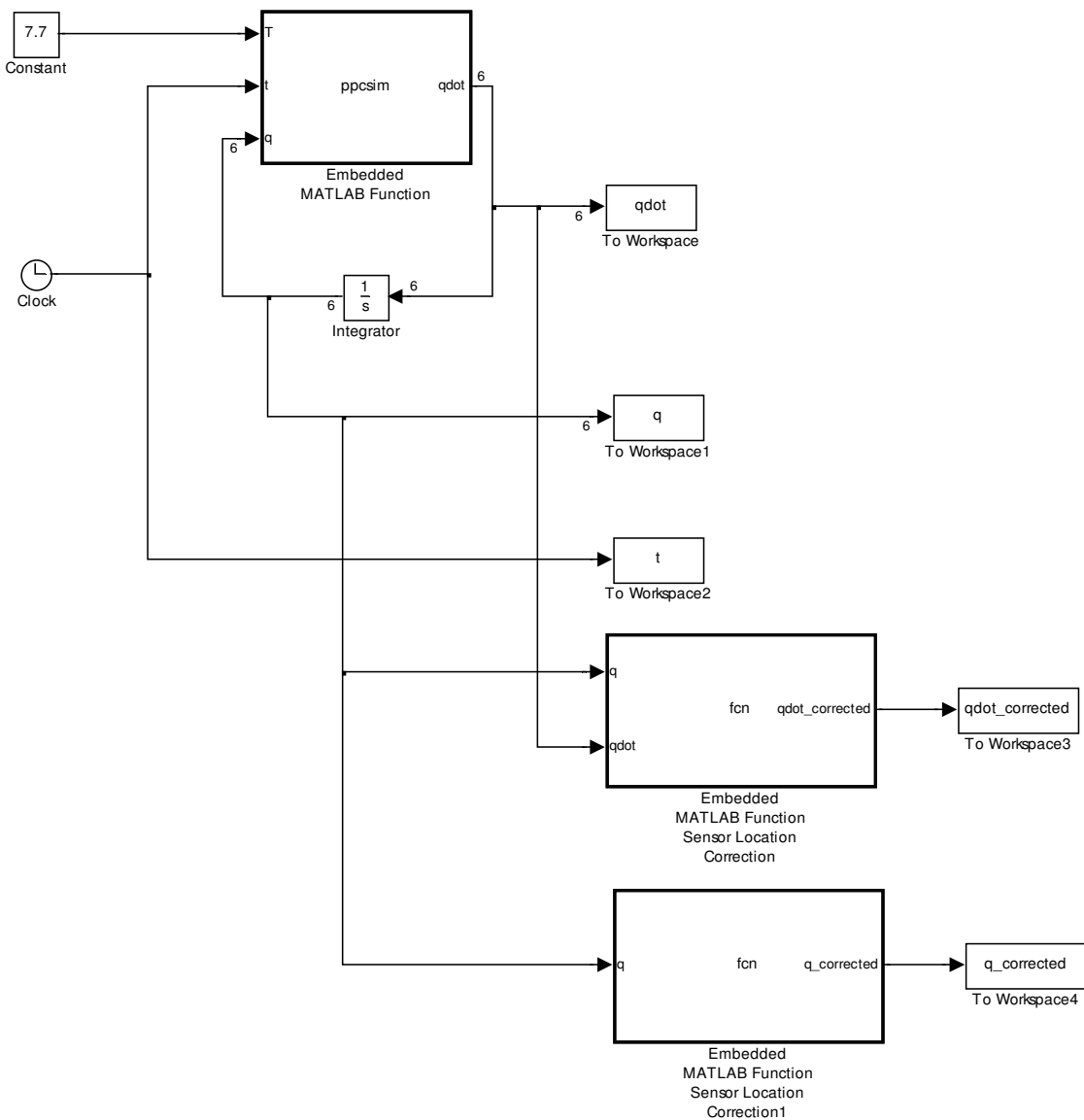


Figure 4-3 –Simulink Block Diagram of PPC Model with Sensor Location Correction

The functions contained in the additional ‘Embedded MATLAB Function’ blocks are given below:

```
function qdot_corrected = fcn(q,qdot)
h=0.20; %vertical distance between aircraft CG and sensors [m]
```

```

qdot_corrected=[0;0;0;0;0;0];

qdot_corrected(1)=qdot(1)+h*cos(q(5))*q(6);
qdot_corrected(2)=qdot(2)+h*cos(q(5))*qdot(6)-h*sin(q(5))*q(6)^2;
qdot_corrected(3)=qdot(3)-h*sin(q(5))*q(6);
qdot_corrected(4)=qdot(4)-h*sin(q(5))*qdot(6)-h*cos(q(5))*q(6)^2;
qdot_corrected(5)=qdot(5);
qdot_corrected(6)=qdot(6);

function q_corrected = fcn(q)

h=0.20;    %vertical distance between aircraft CG and sensors [m]

q_corrected=[0;0;0;0;0;0];

q_corrected(1)=q(1)+h*sin(q(5));
q_corrected(2)=q(2)+h*cos(q(5))*q(6);
q_corrected(3)=q(3)-h*(1-cos(q(5)));
q_corrected(4)=q(4)-h*sin(q(5))*q(6);
q_corrected(5)=q(5);
q_corrected(6)=q(6);

```

The outputs,  $q_{\text{corrected}}$  and  $qdot_{\text{corrected}}$  include the position, velocity, and acceleration of the sensors, which are located 0.20 m below the overall aircraft CG.

## 4.2 Simulation Results

Simulations were run both with and without apparent mass effects included in the model. Flight characteristics that could later be validated using experimental data were recorded. The steady-state climb rate and response to a throttle step input were observed and are documented in the following sections. The data will be compared to experimental results in section 5.3.

### 4.2.1 Climb Rate

The climb rate of the aircraft was plotted against thrust for the analytical model both with and without apparent mass effects included. The graph of figure 4-4 shows the results of those simulations. Climb rates were determined at seven select thrust values which will later be compared to experimental data presented in section 5.1.2. The climb rate is shown using upward as the positive direction.

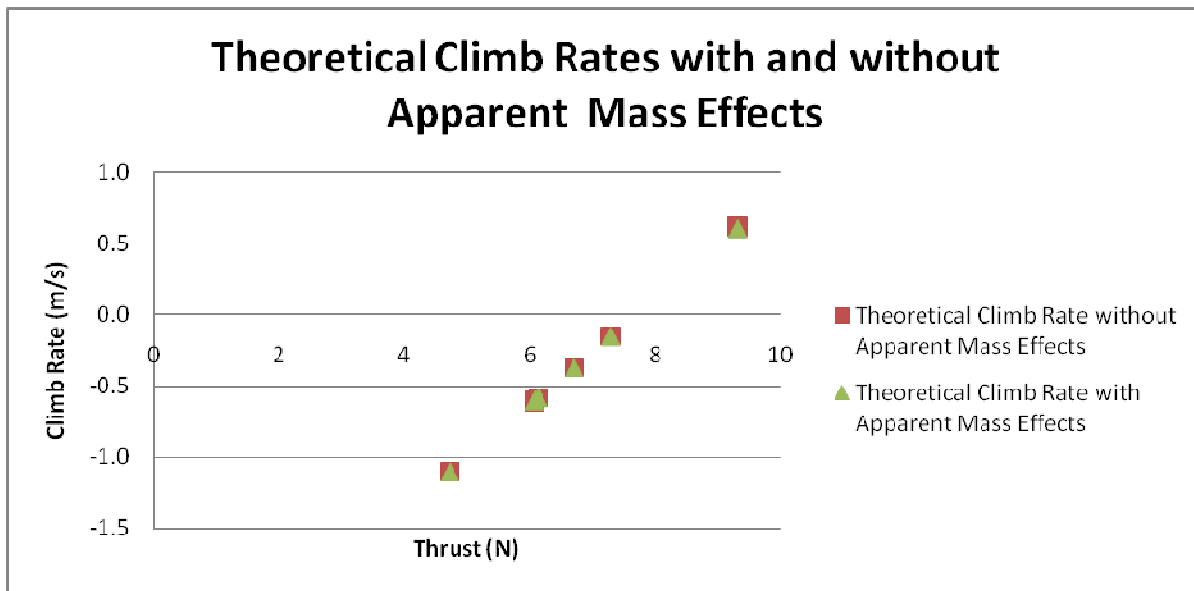


Figure 4-4 – Theoretical Climb Rates

Above, we see the linear nature of the Climb Rate vs. Thrust data. We also see that the minute additions to aircraft mass and inertia due to apparent mass have virtually no effect on the steady-state climb rate of the aircraft. This is agreeable with one's intuition, in that apparent mass is due to an aircraft carrying a sort of 'air bubble' around its wing. This air that travels with the PPC should not impart any buoyancy force onto the system, which is

itself surrounded by air. It should, therefore, have no effect on the steady state climb rate of the aircraft. In fact, when examining the climb rates to two decimal places, they are nearly identical for the cases with and without apparent mass effects, as shown in table 4-1.

Thrust (N)	Theoretical Climb Rate without Apparent Mass (m/s)	Theoretical Climb Rate with Apparent Mass (m/s)
4.728	-1.10	-1.10
6.078	-0.61	-0.60
6.084	-0.60	-0.60
6.136	-0.58	-0.58
6.707	-0.37	-0.37
7.292	-0.15	-0.15
9.31	0.62	0.60

*Table 4-1 – Theoretical Climb Rates*

When fitting a trendline to either of the theoretical climb rate data sets, we observe that the data is indeed linearly disbursed, with an  $R^2$  value greater than 0.999. This can again be seen below in figure 4-5, where the climb rates are computed for thrust values between 0.25 and 9.25 N on 0.25 N intervals.

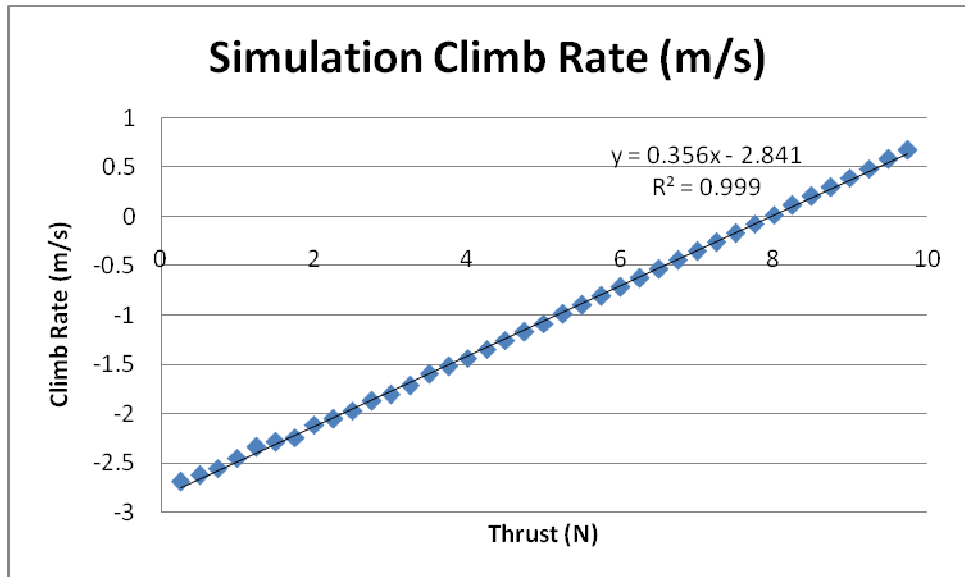


Figure 4-5 – Simulation Climb Rates with 0.25 N Thrust Intervals and Trendline

#### 4.2.2 Step Input of Thrust

A step input is not only a fundamental tool for the analysis of a dynamic system, but is also the only dynamic response whose characteristics could be validated by the experimental data collected. Step inputs of thrust were, therefore, the focus of the dynamic response simulations.

##### 4.2.2.1 Altitude Response

The results given below show the model's altitude response to a few different step inputs. The throttle steps are initiated at a time of 10 seconds and the altitude response of the aircraft fuselage is shown. Additional thrust step response graphs are given in appendix A.

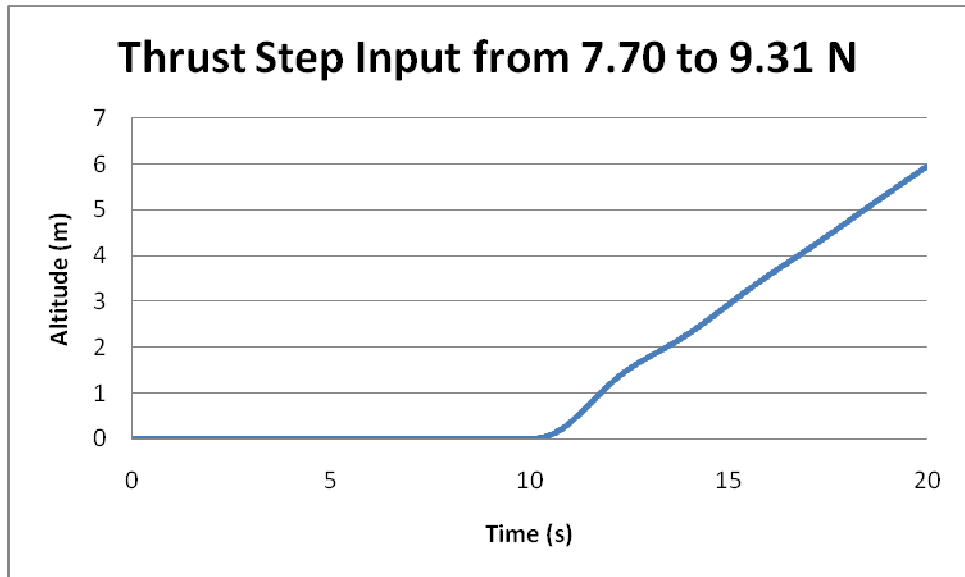


*Figure 4-6 – Altitude Response to Simulated Step Input- Level Flight to Climb*

Figure 4-6 shows a thrust step input transitioning from level flight to a climb rate of 0.6 m/s. The aircraft in level flight reacts immediately to the thrust input and within a half of a second is climbing at a rate near its steady state value. The 90% rise time in the climb rate is 0.43 seconds, so a relatively small amount of lag exists for a maneuver such as this. The slight periodicity that is noticeable after the step is representative of powered parachute flight.

Figure 4-7 shows the altitude response to a thrust input with the aircraft transitioning from a constant descent to level flight.

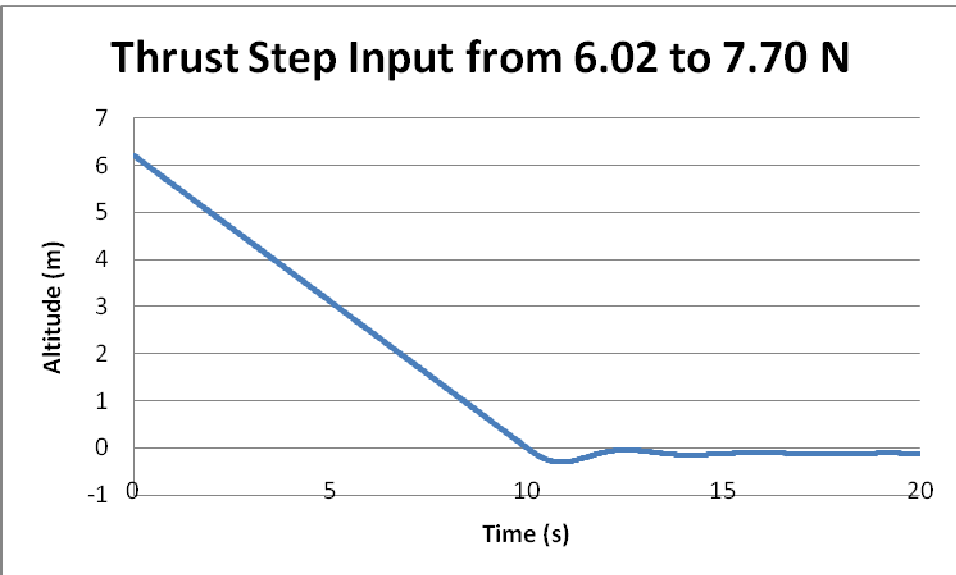


*Figure 4-7 – Altitude Response to Simulated Step Input- Descent to Level Flight*

It is interesting to note that there is overshoot of the altitude value that the step was initiated at (in this case 0 m), but the aircraft begins to settle on a steady-state value that is very close to that of the initial thrust increase. After the thrust is increased to a value necessary for level flight, the aircraft continues to descend for an additional 0.78 seconds. The total overshoot is 0.3 m beyond the altitude value at the initiation of the step, with a steady state value in level flight of -0.1 m.

Figure 4-8 shows a transition from the same constant descent to a climb.

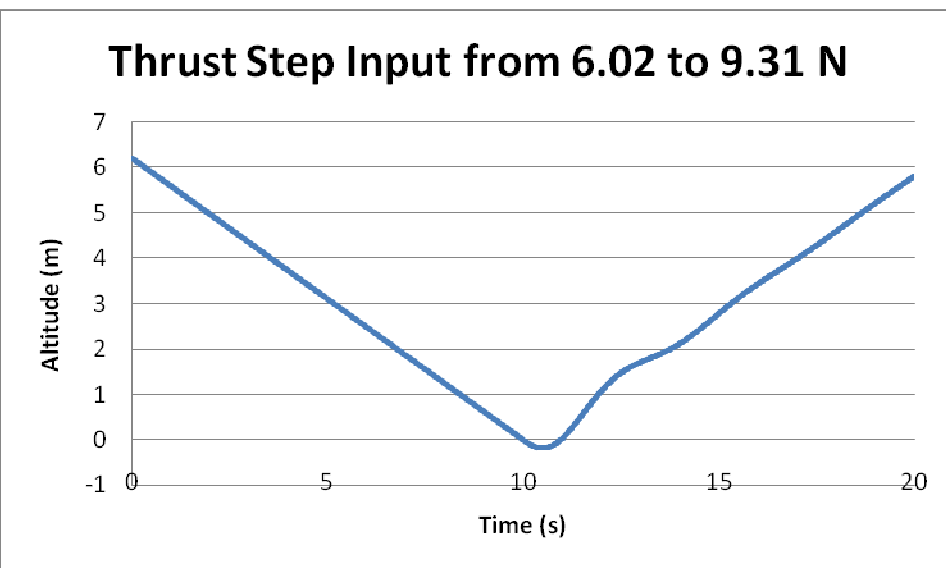


*Figure 4-8 – Altitude Response to Simulated Step Input- Descent to Climb*

The initial constant descent rate is 0.6 m/s, and a thrust step is input such that the aircraft will begin to climb at a rate of 0.6 m/s upward. In this case we note a lag of 0.47 seconds between the throttle increase and initiation of a climb. The 90% rise time in the climb rate is 0.72 seconds.

#### 4.2.2.2 Speed Response

The response in aircraft speed to a large thrust step input is shown below. The thrust is increased from 6.02 to 9.31 N causing a momentary increase in aircraft speed. This creates an oscillation in airspeed which can be seen in figure 4-9.

### Thrust Step Input from 6.02 to 9.31 N

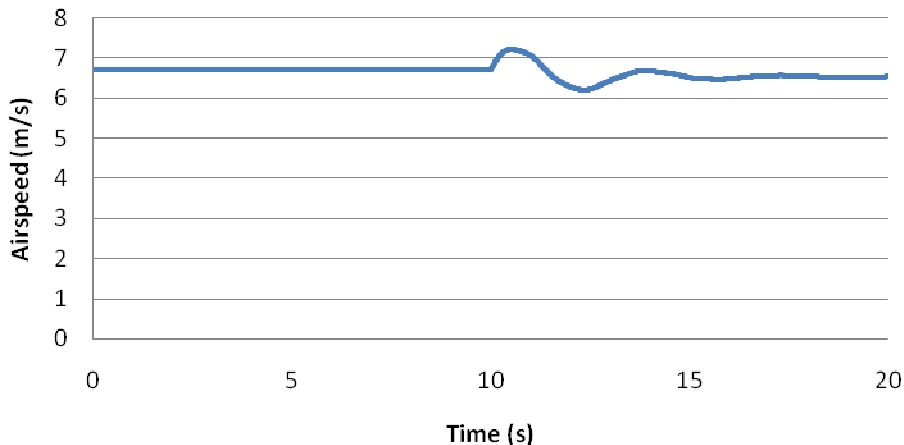


Figure 4-9 – Speed Response to Simulated Step Input- Descent to Climb

It is interesting to note that the steady state airspeed of the powered parachute is actually lower with a larger thrust value. When thrust is increased, a large portion of the aircraft thrust begins to fight against both gravity and the parafoil wing, decreasing the aircraft's flight speed. This effect can again be seen in figure 4-10 with a step decrease from a level flight value to zero thrust.

### Thrust Step Input from 7.70 to 0 N

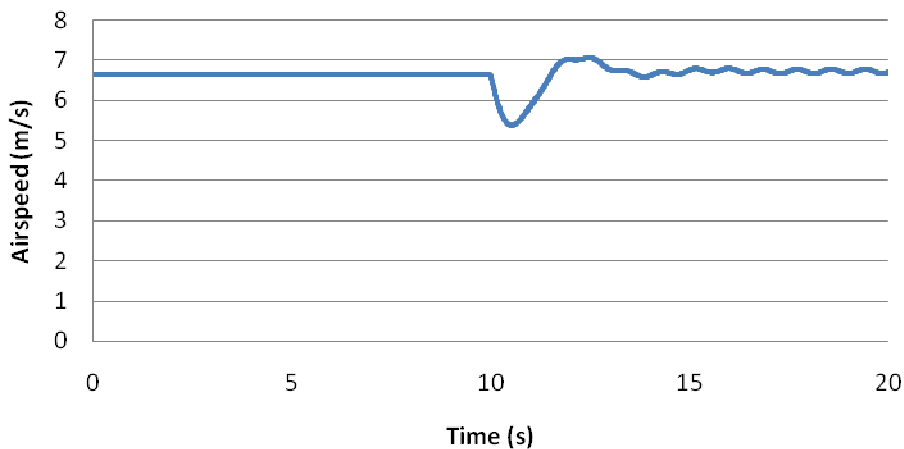


Figure 4-10 – Speed Response to Simulated Step Input- Level Flight to Zero Thrust

With a step decrease in throttle we first note a momentary decrease in airspeed before it oscillates around a slightly higher airspeed value. It is worth mentioning that with zero thrust, this airspeed oscillation continues for far longer than with any constant thrust value.

Aircraft mass is much more influential on airspeed than thrust. As the weight of the aircraft increases, the parafoil must create more lift to keep the PPC aloft. The system, therefore, does not reach equilibrium until a high enough airspeed is attained to create the required lift at the parafoil.

## **5.0 Flight Tests of the Small-Scale Powered Parachute**

Flight testing was conducted by the author using the small-scale powered parachute. Tests took place on nearly windless evenings to minimize atmospheric uncertainty in the measurements being collected. The aircraft was piloted via remote-control and performed constant climbs and descents, level flight, and a number of throttle step inputs while data was being logged.

Testing was somewhat limited by the capabilities of the aircraft and pilot. Observation of throttle pulse inputs would have been desirable; however, successful demonstration of these maneuvers would have been too difficult. For this reason, only the flight tests mentioned above were performed.

### **5.1 Steady-State Flight Properties**

The properties of steady-state flight were tested for the powered parachute aircraft. These simple tests can give a more immediate, overall idea of the validity of a dynamic model and provide information on the overall flight capabilities of the aircraft.

#### **5.1.1 Flight Airspeed**

The simplest check to begin evaluating the validity of an analytically derived dynamic model for a powered parachute is to compare the in-flight airspeed of the model to that obtained during flight testing. The airspeed of a PPC tends to be rather constant, so large fluctuations in the steady-state airspeed would be an immediate indication of a problem with the model.

While the airspeed measurements obtained by the flight data logging system did exhibit some degree of noise, the reasonably constant speed nature of these aircraft can be readily observed in flight test data. The following chart shows airspeed measurements over the duration of 60 seconds of flight.

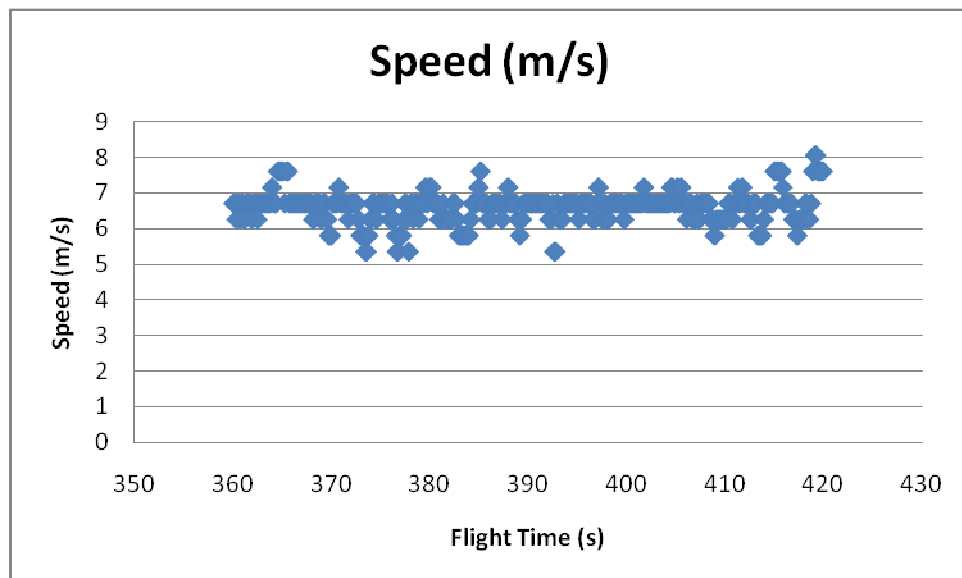


*Figure 5-1 –Airspeed During 60 Seconds of Flight*

Some noise in the airspeed data has been observed, as well as some variation in airspeed during tight turn maneuvers and sudden thrust increases. However, over 60 seconds worth of climbing, descending, and turning, the airspeed does remain rather constant, with an average value just below 7 m/s.

## 5.1.2 Climb Rate

Climb rate represents the most fundamental steady-state property of an aircraft when thrust-based longitudinal control is considered. Since throttle position is the only form of longitudinal control that is used during normal PPC flight, a relationship between thrust and climb rate can give a very good indication of the overall longitudinal characteristics of these types of aircraft. One important step in any powered parachute study is to calibrate thrust data to the resulting climb rate.

The climb rate of our aircraft can be calibrated to thrust using the data shown in table 5-1. These data points were obtained by observing constant climb and descent measurements after flights had been conducted. During a given period of time with a constant thrust input, a linear trendline was fit to the altitude data obtained, with the slope of this line yielding the aircraft climb rate.

Thrust (N)	Climb rate (m/s)
4.728	<b>-1.389</b>
6.078	<b>-0.666</b>
6.084	<b>-0.528</b>
6.136	<b>-0.510</b>
6.707	<b>-0.242</b>
7.292	<b>0.043</b>
9.310	<b>0.895</b>

Table 5-1 –Experimental Climb Rate vs. Thrust

Graphing the climb rate vs. thrust data yields a linear distribution, as given in figure 5-2. Since the data of table 5-1 was obtained through the averaging process of fitting trendlines, determining the uncertainty in these climb rate figures is somewhat difficult. A better

indication of the accuracy of this data is to observe the degree of deviation from the linear trendline in the following graph.

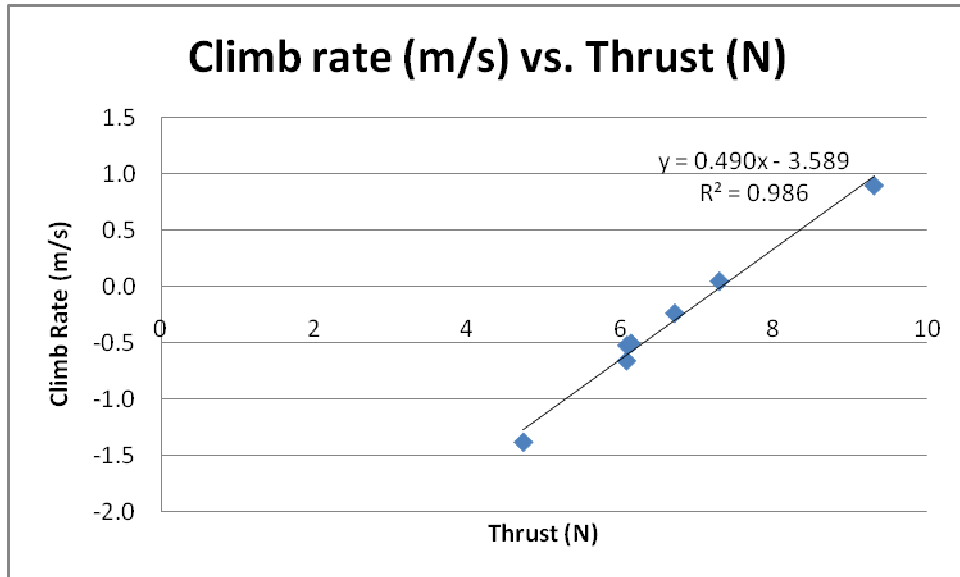


Figure 5-2 –Climb Rate vs. Thrust Graph

The linear trendline in figure 5-2 represents a useful equation which relates aircraft climb rate to thrust:

$$[\text{Climb Rate (m/s)}] = 0.490 \frac{\text{kg}}{\text{s}} \times [\text{Aircraft Thrust (N)}] - 3.589 \frac{\text{m}}{\text{s}}$$

One must also note that the value of  $R^2$  for the regression line has a value of 0.986, meaning 98.6% of the variation in climb rate vs. thrust can be adequately described by this relationship.

Utilizing this equation with the maximum sustainable thrust value gives a good indication of the aircraft's maximum climb rate. The aircraft drag can be obtained by setting the climb rate equal to zero and solving for thrust. When this is done, we obtain a value of 7.32 N for the total drag on our test aircraft in level flight. Additionally, we can obtain a rough estimate of the sink rate in unpowered flight from the equation. When the aircraft is throttled down to unpowered flight, it will descend at a rate somewhere around 3.6 m/s.

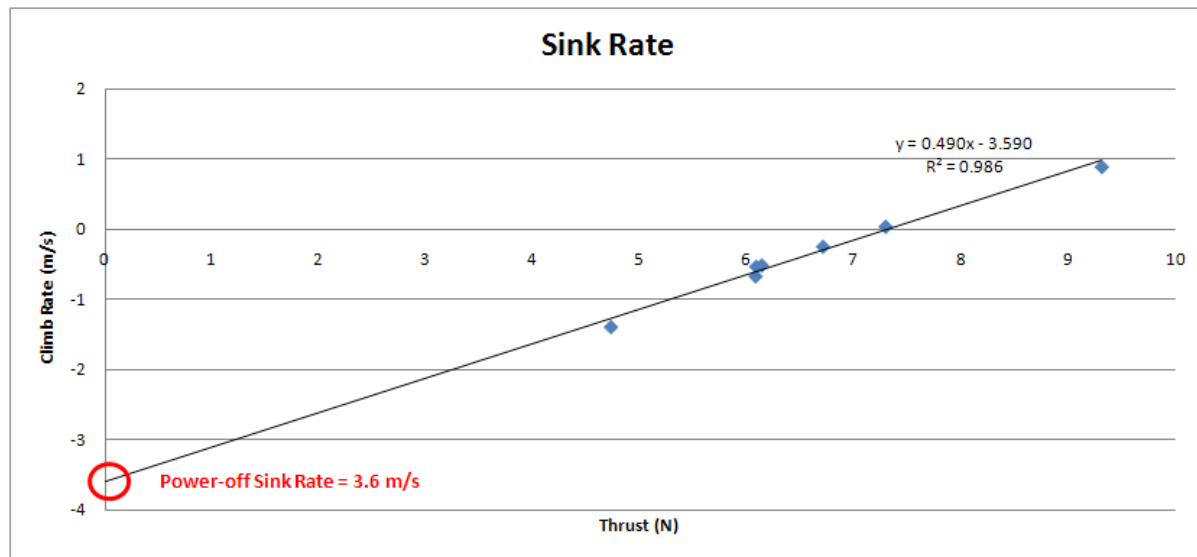


Figure 5-3 – Estimation of Sink Rate

It must be noted that this is not always an accurate portrayal of the unpowered sink rate of an aircraft because a large amount of drag is created if the propeller is windmilling, something that is not accounted for in this estimate.

## 5.2 Step-input of Thrust

A throttle step-input was chosen as the most appropriate function for the evaluation of the transient behavior of the dynamic system. The aircraft was initially flown in until reasonably steady-state conditions were reached. At that point, the throttle control was quickly increased or decreased to another constant value. The data logging system was able to successfully document the flight characteristics of the aircraft throughout the duration of this maneuver.

A few select step-input cases are shown in this section, with additional step input data displayed in Appendix B. It must be noted that the nature of the battery and motor setup limits the available electrical current during constant throttle flight. The step inputs shown exhibit a slight decay of thrust as time goes on, because of the battery's limitations. All things considered, the step inputs contained in both this section and in Appendix B are of reasonably good-quality.

The independent variable on all of the horizontal axes of the following graphs represents flight time, in seconds. The dependent variables and units are shown in the titles of each inlay. The Y G-force relates to the vertical acceleration of the aircraft, while the X G-force measures forward acceleration. Both sets of G-force values are multiplied by 100 by the data acquisition hardware.

First, a step increase in thrust will be observed:

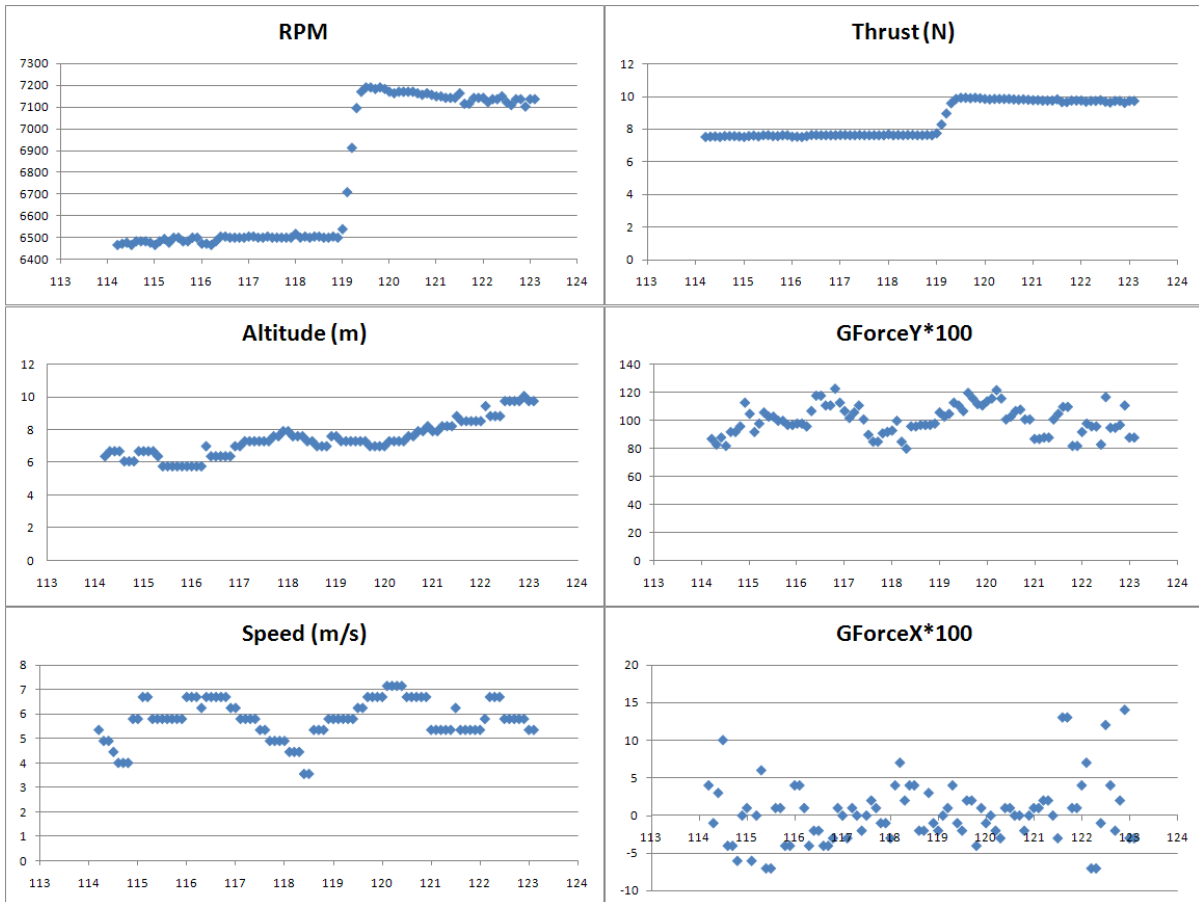


Figure 5-4 –Experimental Thrust Step Increase

Figure 5-4 shows an experimental thrust step increase from approximately 7.6 to 9.8 N. As mentioned, the RPM plot shows a slight decay due to the limitations of the battery. We are able to see a delay of approximately 1 second between the thrust step, at 119.1 seconds, and the initiation of a climb. The speed data shows little useful information beyond giving somewhat of an idea of the flight speed throughout the maneuver. The two dips in speed

prior to the step input have been attributed to atmospheric conditions and sensor noise. They should not be regarded as characteristics of the flight. The G-force graphs show the gentle nature of powered parachute flight. Even with a rapid throttle increase such as this, vertical G-force remains within about 20% of the force of gravity. Horizontal acceleration is even less pronounced with most of the variation in the graph due to electronic noise.

A thrust step decrease is shown below in figure 5-5:

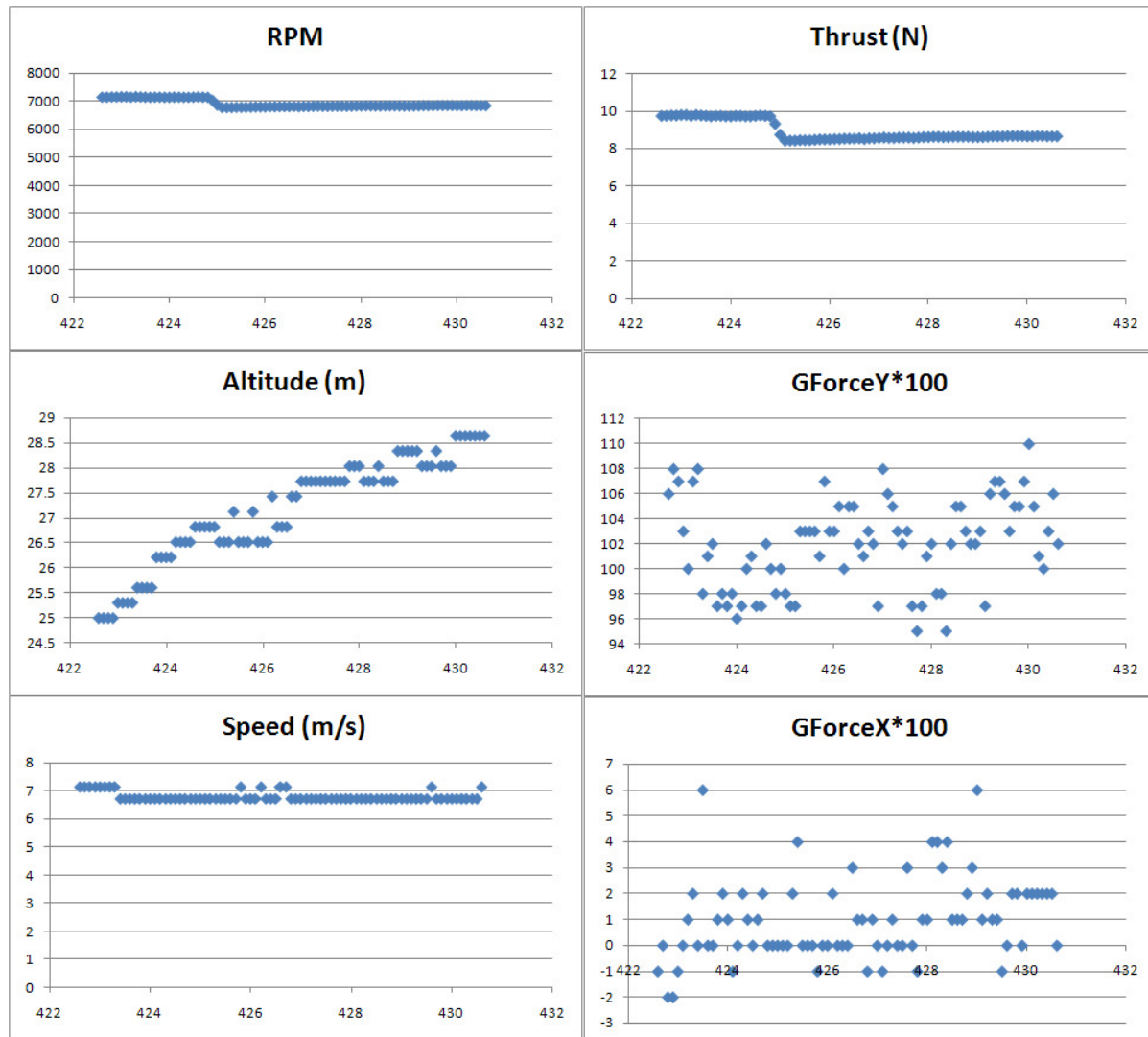


Figure 5-5 –Experimental Thrust Step Decrease

In the above graph we observe a step decrease of slightly smaller amplitude than the previous step increase. After this more gentle thrust change, the aircraft continues to climb, albeit at a slower rate. Less lag is observed in this situation with a flight pattern that generally continues without a major directional change. The aircraft seems to react almost immediately to throttle input in this case. The airspeed measurements remain very constant at a value of approximately 7 m/s. We again observe the placid flight characteristics of the aircraft from the two G-force plots.

These step responses are exemplary of the flight characteristics that have been observed for the test aircraft and will be compared to simulated results. For additional step responses of the small-scale powered parachute aircraft see Appendix B.

## **5.3 Comparison of Experimental Data to Analytical Simulation**

This section provides verification of the rigid-body analytical model that was derived and simulated in previous chapters by direct comparison to the experimental data obtained. The comparison method will first be outlined and then results will be given to prove the validity of the simplified analytical model of section 3.2.

### **5.3.1 Method of Comparison**

As was previously mentioned, this study was somewhat limited by the capabilities of the hardware used in the experimental tests. The author possessed only the bare minimum of measurements necessary to satisfactorily validate the powered parachute model.

The model will be compared in both its steady-state and transient behavior to the experimental data presented earlier in this chapter. For steady state analysis, the simulated climb rate predictions will be overlaid upon experimental data. Transient analysis will be done in the form of altitude response overlays using the representative thrust step-input data that has been reviewed in this chapter.

### **5.3.2 Results**

Shown below is a graph comparing steady-state climb rates obtained through experimental and analytical means.

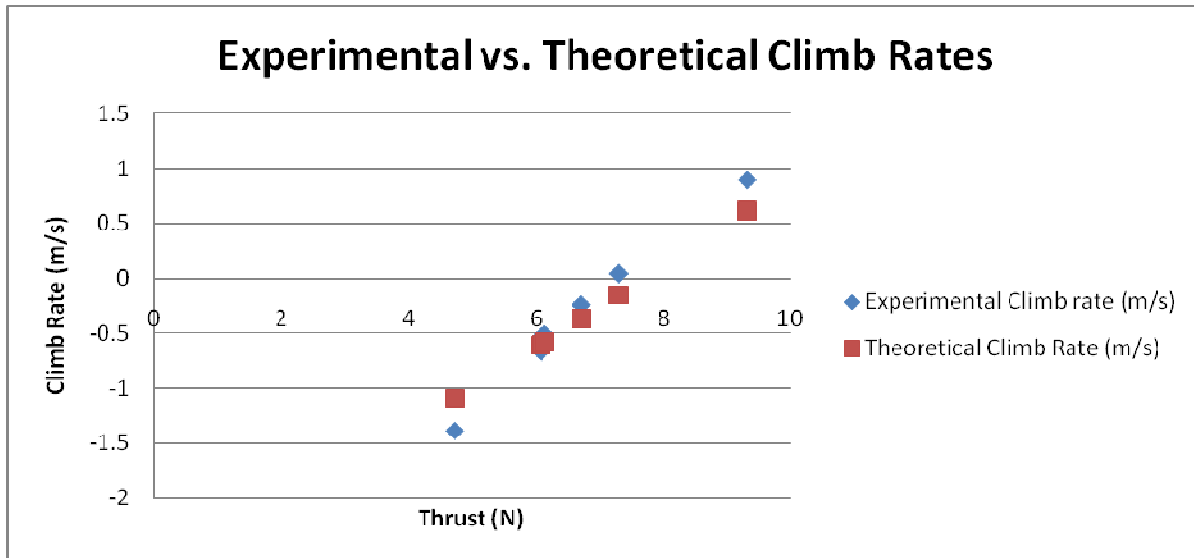


Figure 5-6 –Experimental vs. Theoretical Climb Rate Comparison

It is evident that the climb rates of the simplified analytical model in section 3.2 match up reasonably well with the experimental climb rate data presented in section 5.1.2. There is some discrepancy in the slopes of the climb rate data sets due to inaccuracies in the parafoil lift and drag estimates. The difference is due to imprecision of airspeed measurements, rather than any flaws in the approach to lift and drag estimation given in Chapter 2. Additional innaccuracy may be due to slight differences in the direction of the thrust vector of the experimental aircraft, as compared to the analytical model. The data does, however, match up in a manner that is acceptable for most control work.

The acceptability of the model is more clearly shown in transient response overlays. Figures 5-7 and 5-8 show simulation overlays on the two throttle step input responses from section 5.2. Airspeed graphs are also included for additional comparative information. For both

cases, the actual experimental thrust data was used as the simulation input, with intermediate values being interpolated.

First we see the increasing step-input of thrust:

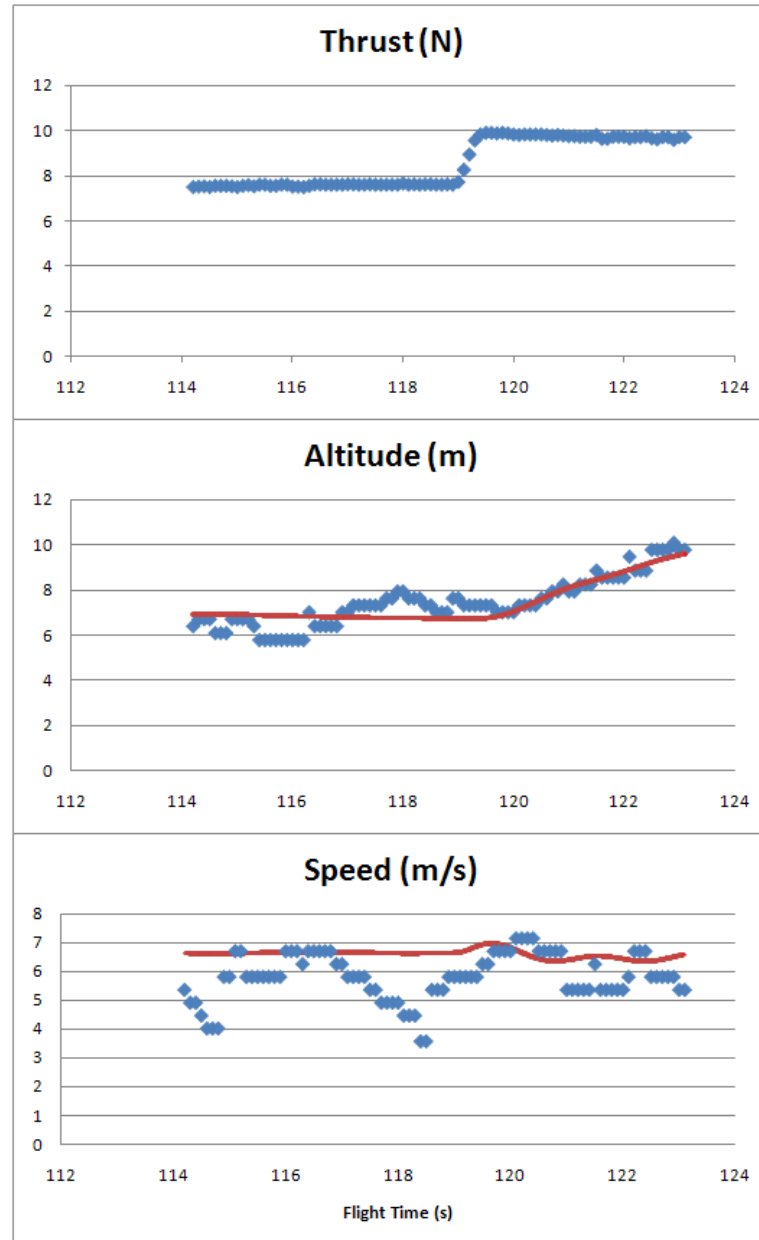


Figure 5-7 –Experimental vs. Theoretical Thrust Step Increase

The simulated altitude response matches very well with the experimental altitude data. There is some discrepancy in the initial half of the overlay, but considering the uncertainties in the altitude measurement hardware as well as atmospheric conditions, the results are quite acceptable. The experimental speed data was found to be very inaccurate at times, due to slight changes in AOA of the air incident upon the pitot tube. The magnitude of most of the experimental airspeed data entries are, however, fairly comparable to the values suggested by the analytical model.

Figure 5-8 shows a simulation overlay upon the data from the step decrease in thrust that was previously discussed.

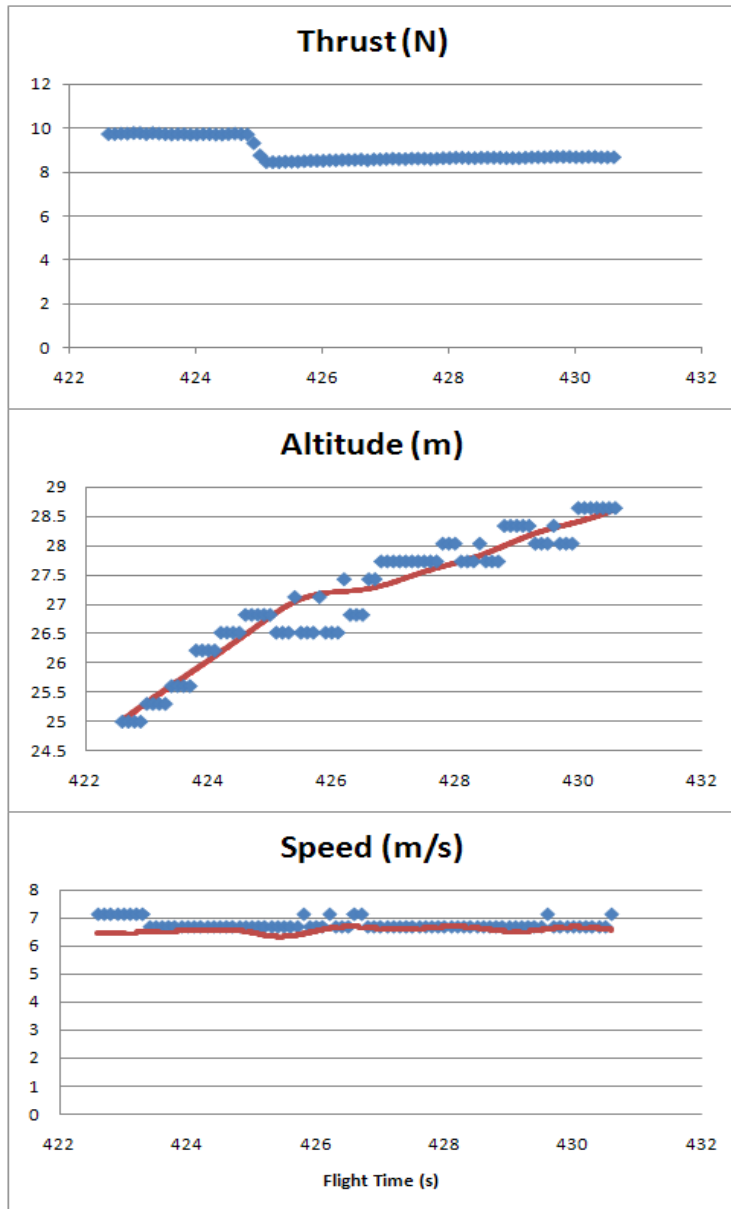


Figure 5-8 –Experimental vs. Theoretical Thrust Step Decrease

The altitude plot again matches very well within the hardware uncertainties discussed in Chapter 2. The simulated results represent the actual aircraft climb rate very well both before and after the throttle step is initiated. The airspeed data sets also match quite well for this case, with values for both analytical and experimental data remaining nearly constant

throughout the maneuver. The data acquisition hardware is not sensitive enough to pick up the nuanced speed changes suggested by the analytical model.

The results shown in this section for both the steady-state and transient responses serve as validation of the accuracy of the analytical dynamic model and simulation. Any slight differences resulting from estimations or assumptions made during the derivation of the analytical model should be well within the ability of a control system to deal with.

## **6.0 Control System Development & Simulation**

The previously derived dynamic model was used in the development and simulation of an altitude-hold control system. Once a model is obtained that satisfactorily represents the aircraft flight characteristics, control system development is fairly straight forward.

### **6.1 Control System Development**

The altitude-hold control system was developed using simple feedback loops monitoring the states that could be observed by aircraft sensors. The two parameters that are most easily obtained using available sensing electronics are altitude and vertical acceleration. The altitude measurements for a control system would preferably be obtained using radar or laser proximity sensing, perhaps in conjunction with barometric sensing. Acceleration can be obtained using a conventional accelerometer. Vertical speed is not easily obtained from the altitude data because it must be filtered so that the aircraft does not react to small changes in the profile of the ground. This averaging filter is necessary when traversing uneven terrain and vegetation. For this reason, vertical velocity feedback will not be used in the control scheme.

The basis for control system development was the Simulink model developed in Chapter 4, which includes corrections in the linear displacement, velocity, and acceleration for the difference between the locations of the aircraft CG and sensors (shown in figure 6-1).

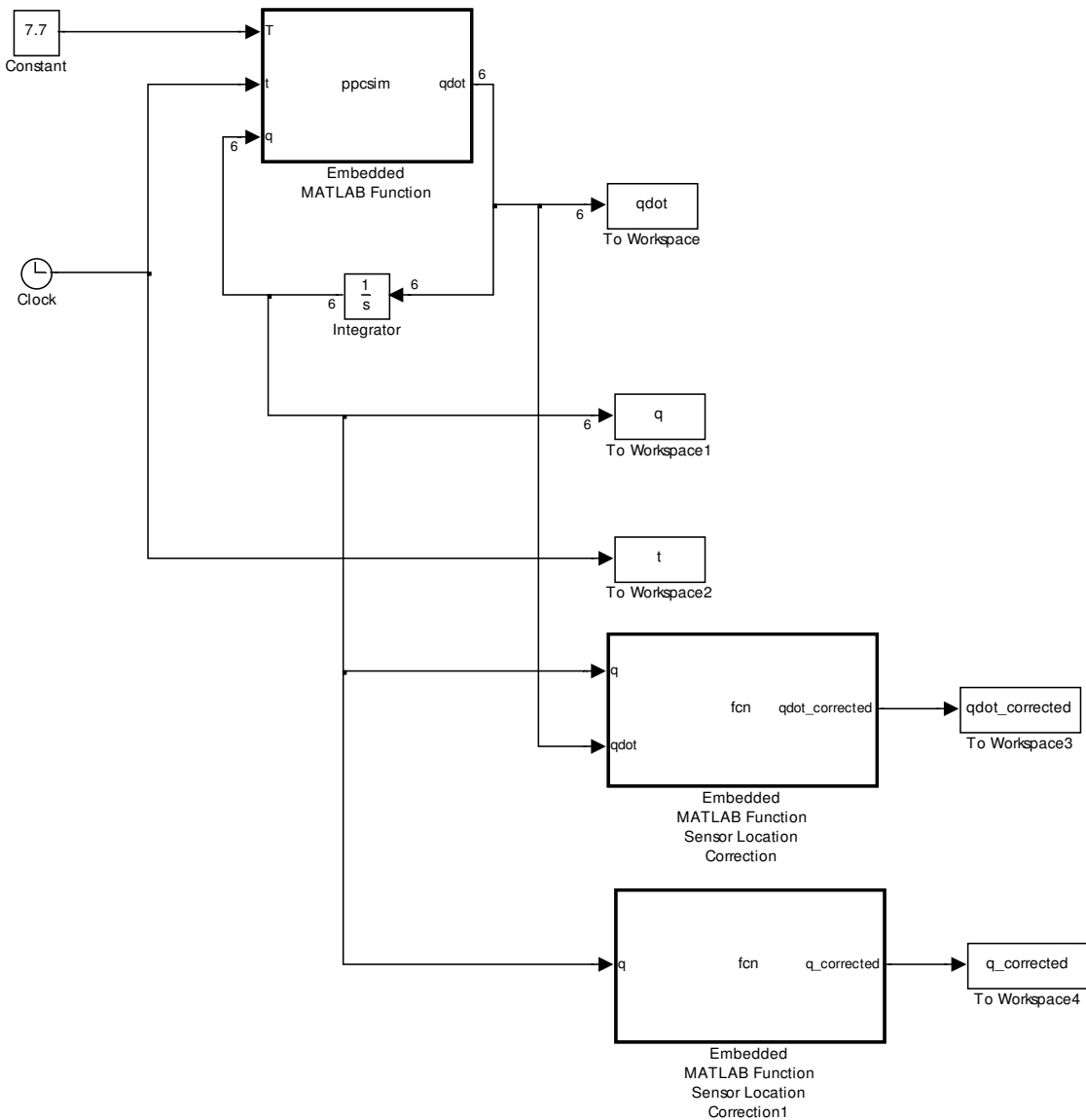


Figure 6-1 –Basis for Control System Development

From this point, feedback loops are added for altitude and vertical acceleration. An error signal is computed as the difference between the target altitude and the actual altitude measurement. These signals are then passed through gains before being summed with the constant thrust value of 7.7 N necessary for level flight. After the required thrust value is

obtained from the summation block, it must be fed through a saturation block in order to keep the thrust within the limits of the aircraft's hardware. Figure 6.2 shows how this control system is implemented in simulation:

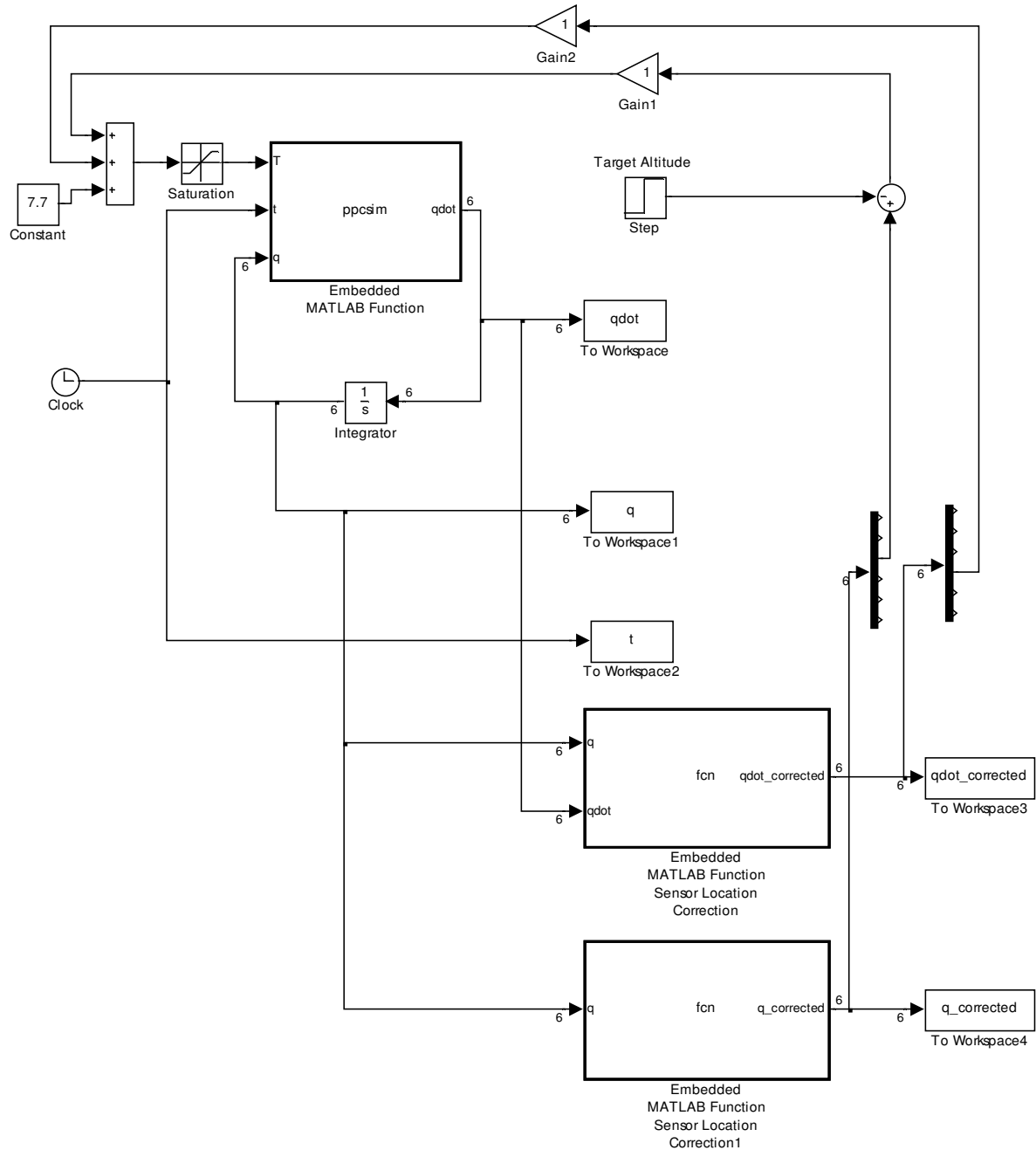


Figure 6-2 –Simulink Control System Implementation

The diagram above shows the control system in a unity-gain configuration. Performance with both feedback gains set to 1 is fairly good, and will be reviewed in the following section. The most important characteristics of a viable control system are a reasonably quick rise time toward a target altitude and no overshoot of the target.

An over-damped configuration is highly desirable in the longitudinal control of a UAV aircraft. This is mainly true if powered landings are to be attempted using the control system. When the target altitude is zero, any appreciable amount of overshoot would mean a hard landing or crash.

Because the control system is not being developed for any specific application, it has not been deemed necessary to tune the gains to meet any performance targets. Depending on the nature of the aircraft mission, gains can be adjusted to desired parameters such as rise time, settling time, and overshoot.

## 6.2 Control System Analysis

Using the control system illustrated in figure 6-2, acceptable performance is obtained using a unity-gain feedback configuration.

A plot showing a slight altitude change of 2 m using this control system is shown in figure 6-3. The small amplitude of altitude change was chosen to keep the thrust values from reaching saturation limits.

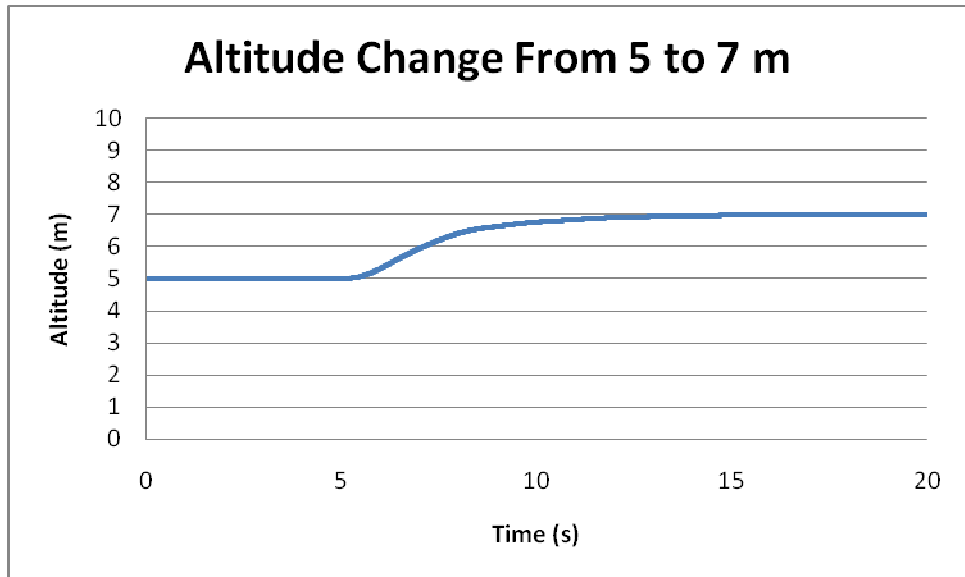


Figure 6-3 –Controlled Altitude Change from 5 to 7 m

From the initial change in target altitude (initiated at a time of 5 seconds), rise time to 90% of the altitude change is 5.2 seconds, when saturation limits on thrust are not reached. Settling time for this case, with a tolerance of 1% of the altitude change, is 10.1 seconds. The system is overdamped so there is no overshoot of the final altitude value.

Next we will consider a larger altitude change that would likely be seen in a case of an altitude adjustment command, rather than variation in the ground contour. In the following graph, the aircraft changes altitude from 50 to 80 meters. The linear nature of the climb is the result of thrust saturation limits being reached.

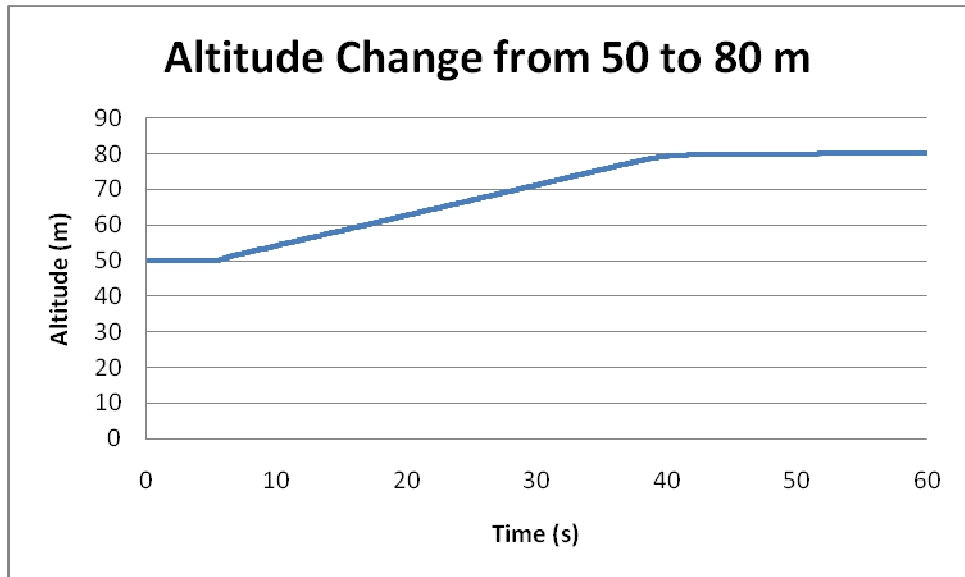


Figure 6-4 –Controlled Altitude Change from 50 to 80 m

Figure 6-4 shows a successful altitude adjustment of 30 meters, beginning at a flight time of 5 seconds. The aircraft climbs at full throttle for almost the entire maneuver, completing the climb in approximately 35 seconds. The simulation demonstrates the ability of this control system to adjust aircraft altitude to any value that the PPC is capable of obtaining, within a reasonable amount of time. Adjustments to lower altitudes are even faster because the aircraft's maximum sink rate is more than 3 times greater than its maximum climb rate. Even with this high descent rate, no overshoot of altitude targets are observed.

Simple wind gust analysis was conducted for the given control system by introducing a bias in airspeed. A Simulink 'Discrete Wind Gust Model' block was used to simulate gusts using the mathematical representation given in Military Specification MIL-F-8785C. The system was able to adequately deal with horizontal wind gusts of amplitudes approaching the aircraft's flight speed. Operation in conditions such as this would not be desirable due to the

effects of sustained wind on the aircraft's ground speed. Figure 6-5 shows a simulated altitude response to a 3.5 m/s horizontal wind gust initiated at a time of 5 seconds. The aircraft is flying in the windward direction.

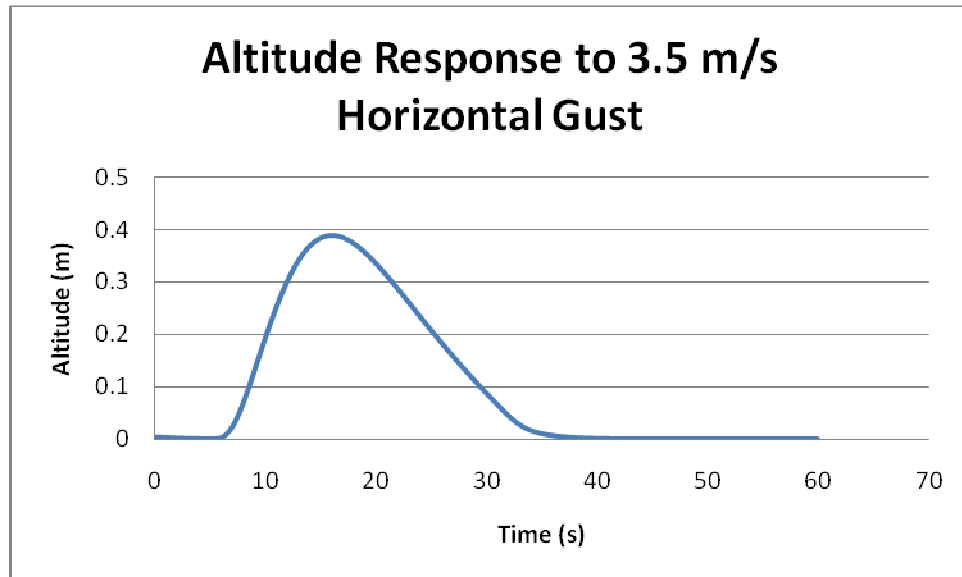


Figure 6-5 –Altitude Response to Horizontal Wind Gust

The aircraft initially climbs a small amount due to increased lift, before resuming flight at its target altitude, in this case shown as 0 m. The amplitude of the altitude disruption is reasonably small, in this case less than 0.4 m.

Vertical wind gusts are also handled in an adequate manner, though the lack of airspeed feedback introduces a steady-state altitude error for sustained vertical winds. The altitude error is, however, fairly small. With a sustained downward wind gust of 0.5 m/s, the aircraft will resume level flight in less than 20 seconds, though with an altitude error of 1.3 m.

Altitude disruption with a gust of this strength did not exceed 1.3 meters from the aircraft's

target altitude. Generally, this simulated control system was able to demonstrate altitude hold capabilities within 1-2 meters, even with mild wind gusts simulated.

## **7.0 Conclusions**

This section outlines the conclusions drawn from the research presented in this paper.

General conclusions on powered parachute dynamic modeling and control are reviewed, as are challenges that are faced when working with an aircraft of this type. Finally, recommendations are made for future work in this area.

### **7.1 General Conclusions**

It has been shown that a three degree-of-freedom analytical model represents the longitudinal flight of conventionally designed powered parachute aircraft with a good degree of accuracy. If unorthodox fuselage configurations are employed, relative motion between the fuselage and canopy may need to be taken into account.

Accurate altitude control is possible for PPC using feedback of altitude and vertical acceleration alone. For this reason, a longitudinal flight control system can be assembled using COTS components and minimal electronics. The combination of the ease of control and the simplicity of the aircraft itself provide for very robust platform with nearly unmatched stability, which can be assembled at an extremely low cost.

These aircraft are able to fulfill a role between lighter-than-air and conventional aircraft, possessing many of the desirable qualities of both. Due to their simplicity of control, the powered parachute is likely to see far more use in the burgeoning field of unmanned aerial vehicles in the near future. Because the theory and experiments presented here are fully

scalable, the modeling and control techniques used in this paper can be applied to PPC of any size.

## 7.2 Challenges Faced

The most daunting challenge faced in the development of a longitudinal control system for a PPC is determination of the aerodynamic characteristics of the parafoil. Parafoil wings are often too large for most wind tunnels and their non-rigid structure defies conventional methods for adjusting angle-of-attack. In addition, the non-standard, somewhat unscientific design techniques employed for most parafoils makes it nearly impossible to obtain a parafoil wing with a given airfoil cross section in order to analytically determine aerodynamic characteristics.

We have, however, shown a number of assumptions that can be made to simplify the parafoil analysis. If a parafoil is tested by towing it behind a vehicle while attached to force measurement hardware, accurate lift and drag data can be obtained for different airspeeds. With the constant angle-of-attack assumption that was justified in Chapter 2, this data can be used to accurately portray the aerodynamic characteristics of a given parafoil wing when used on a PPC.

The greatest challenge facing a powered parachute aircraft in general is its vulnerability to high wind conditions. When considering the powered parachute as an option for development of any UAV system, the atmospheric conditions that the aircraft will encounter must be seriously considered. PPC are sensitive to wind gusts because of their light wing

loadings. In addition to this, sustained winds approaching the aircraft flight speed would render the aircraft unable to move in a windward direction.

## 7.3 Recommendations for Future Work

It is recommended that future work in longitudinal control of powered parachutes is begun by using the 3-DOF simplified model developed in this paper. This model will be sufficient for most PPC aircraft and should always be considered before adding additional complexity to the flight model. If it is found that a large degree of relative motion exists between the fuselage and canopy, it may be more advantageous to modify the aircraft fuselage configuration than to attempt to mathematically represent the dynamics of the PPC in its current form. If a 4-DOF model is still desired, some recommendations for further model development can be found in section 3.3.

For the development of a fully autonomous aircraft system using a powered parachute, an attempt should be made at combining this longitudinal work with the lateral/directional models developed for glided parafoil systems. After the lateral/directional model is modified slightly for the addition of motor torque, it should be possible to couple the two models in order to form a full dynamic model for the flight of a powered parachute aircraft.

## **References**

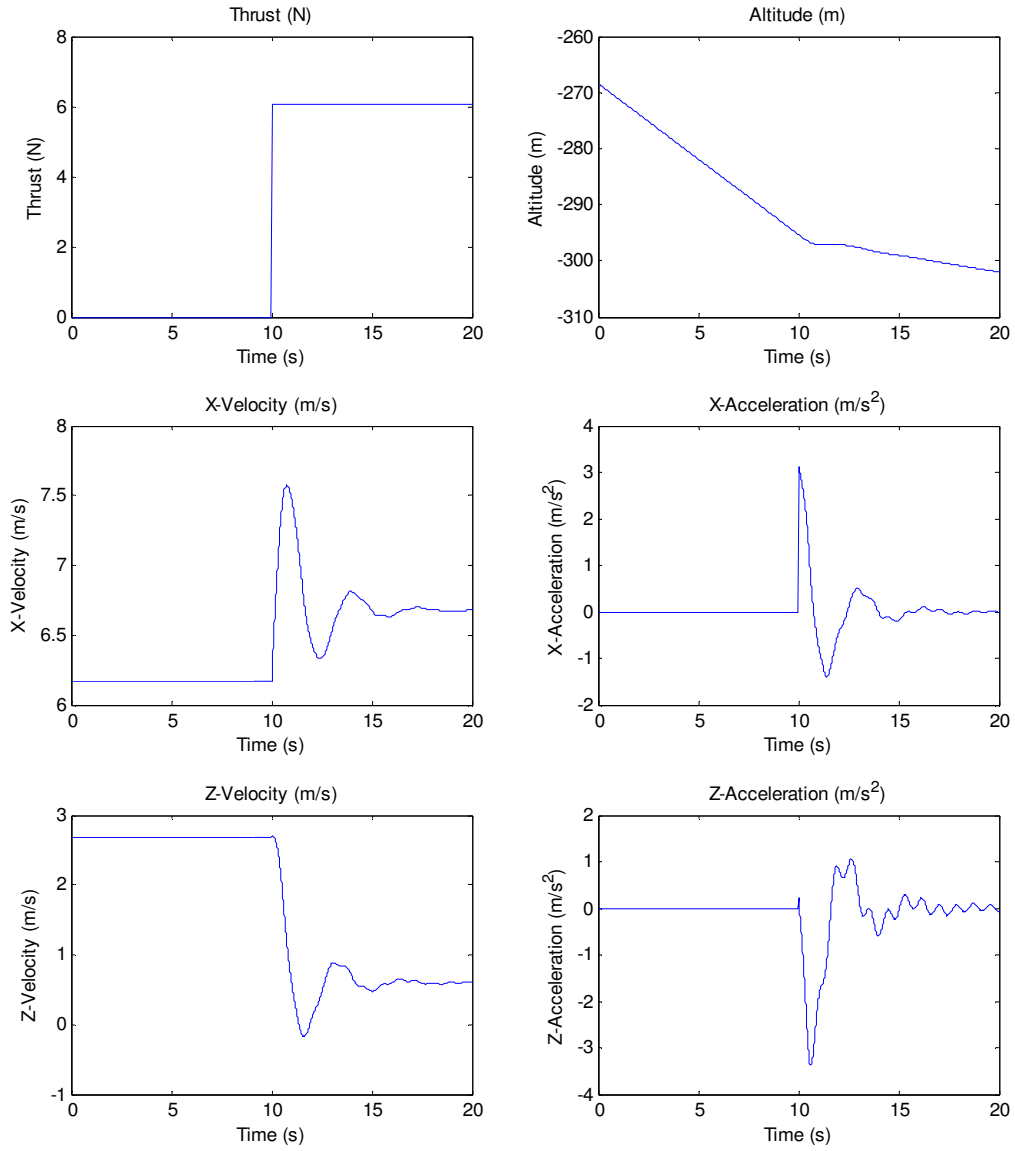
1. Inculet, I.I. and J.K. Fischer, *Electrostatic Aerial Spraying*. IEEE Transactions on Industry Applications, 1989. **25**(3): p. 558-62.
2. HOWARD, S.P., *SPECIAL OPERATIONS FORCES AND UNMANNED AERIAL VEHICLES: SOONER OR LATER?* 1995, SCHOOL OF ADVANCED AIRPOWER STUDIES: MAXWELL AIR FORCE BASE, ALABAMA.
3. Gregorwich, W. *Airborne ground penetrating radar system*. 1996. Snowmass, CO, USA: IEEE, Los Alamitos, CA, USA.
4. Aftergood, S. X-38. 2002 8/5/2002 [cited 9/20/2006]; Available from: <http://www.fas.org/spp/guide/usa/launch/x-38.htm>.
5. Strahan, A.L. *Testing of Parafoil Autonomous GN&C for X-38*. in *17th AIAA Aerodynamic Decelerator Systems Technology Conference and Seminar*. 2003. Monterey, California: American Institute of Aeronautics and Astronautics Inc., Reston, VA 20191, United States.
6. Soppa, U., T. Gorlach, and A.J. Roenneke, *German contribution to the X-38 CRV demonstrator in the field of guidance, navigation and control (GNC)*. Acta Astronautica, 2005. **56**(8): p. 737-749.
7. Hur, G.-B. and J. Valasek. *System Identification of Powered Parafoil-Vehicle from Flight Test Data*. in *AIAA Atmospheric Flight Mechanics Conference and Exhibit*. 2003. Austin, Texas: American Institute of Aeronautics and Astronautics Inc., Reston, VA 20191, United States.
8. Lund, D.W. *Unmanned powered parafoil tests for guidance, navigation, and control development*. 2004. Chicago, IL, United States: American Institute of Aeronautics and Astronautics Inc., Reston, VA 20191, United States.
9. Hattis, P.D. and R. Benney. *Demonstration of precision guided ram-air parafoil airdrop using GPS/INS navigation*. 1996. Cambridge, MA, USA: Inst of Navigation, Alexandria, VA, USA.
10. Ware, G.M. and J.L. Hassell, *Wind-Tunnel Investigation of Ram-Air-Inflated All-Flexible Wings of Aspect Ratios 1.0 to 3.0*. 1969, National Aeronautics and Space Administration: Hampton, VA.
11. Slegers, N. and M. Costello. *Model predictive control of a parafoil and payload system*. 2004. Providence, RI, United States: American Institute of Aeronautics and Astronautics Inc., Reston, VA 20191, United States.
12. Strickert, G., *Study on the relative motion of parafoil-load-systems*. Aerospace Science and Technology, 2004. **8**(6): p. 479-488.
13. Messinger, M., "Remote" control. Unmanned Systems, 1994. **12**(3): p. 31-2.
14. Ricci, W.S., et al. *Operational testing of the CQ-10A*. 2004. Anaheim, CA, United States: Association for Unmanned Vehicle Systems International, Arlington, VA 22206, United States.
15. Yamauchi, B. *PackBot: A versatile platform for military robotics*. 2004. Orlando, FL, United States: International Society for Optical Engineering, Bellingham, WA 98227-0010, United States.

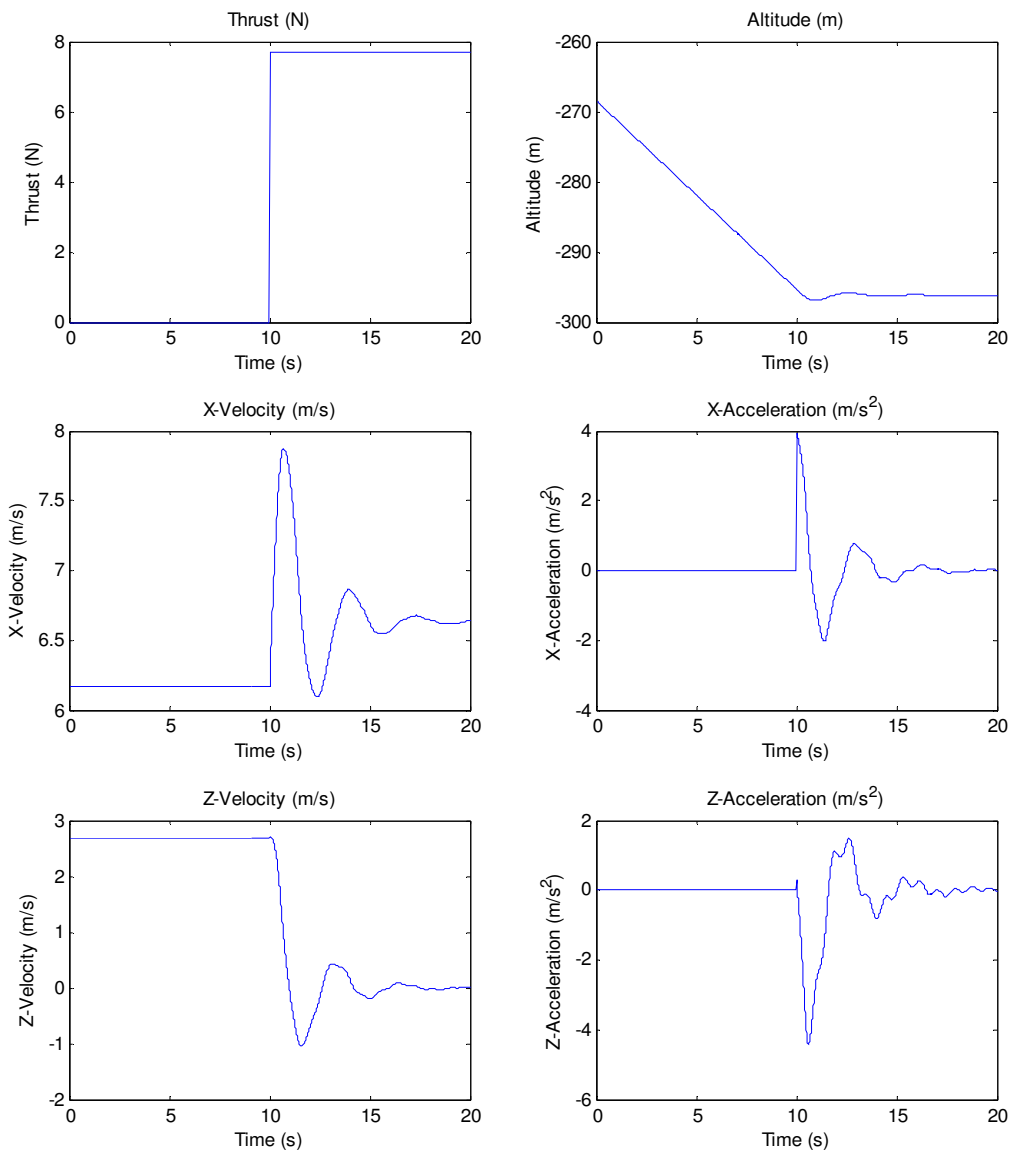
16. Yamauchi, B. and P. Rudakevych, *Griffon: A man-portable hybrid UGV/UAV*. Industrial Robot, 2004. **31**(5): p. 443-450.
17. Colley, D.P., *Unraveling the mysteries of parachutes*. Compressed Air, 1996. **101**(1): p. 12-16.
18. Iosilevskii, G., *Center of gravity and minimal lift coefficient limits of a gliding parachute*. Journal of Aircraft, 1995. **32**(6): p. 1297-1302.
19. Kalro, V. and T.E. Tezduyar, *A parallel 3D computational method for fluid-structure interactions in parachute systems*. Computer Methods in Applied Mechanics and Engineering, 2000. **190**(3-4): p. 321-332.
20. Lissaman, P.B.S. and G.J. Brown, *Apparent Mass Effects on Parafoil Dynamics*, in *12th RAeS/AIAA Aerodynamic Decelerator Systems Technology Conference and Seminar*. 1993, American Institute of Aeronautics and Astronautics: London, England.
21. Lutz, T. and B. Greeves, *THROTTLES ONLY CONTROL (TOC) 10 Steps to a Survivable Landing Following Loss of Normal Flight Control*, in *Interpilot*. 2004. p. 32-34.
22. Burcham, F.W.J., et al., *Preliminary Flight Results of a Fly-by-Throttle Emergency Flight Control System on an F-15 Airplane*. 1993, National Aeronautics and Space Administration.
23. Anderson, J.D., *Fundamentals of Aerodynamics*. 3rd ed. 2001, New York, NY: McGraw-Hill.
24. Tipler, P.A., *Physics for scientists and engineers*. 3rd ed. 1995: Worth Publishers.
25. Meirovitch, L., *Methods of Analytical Dynamics*. 1970, Mineola, New York: Dover Publications, Inc. 524.

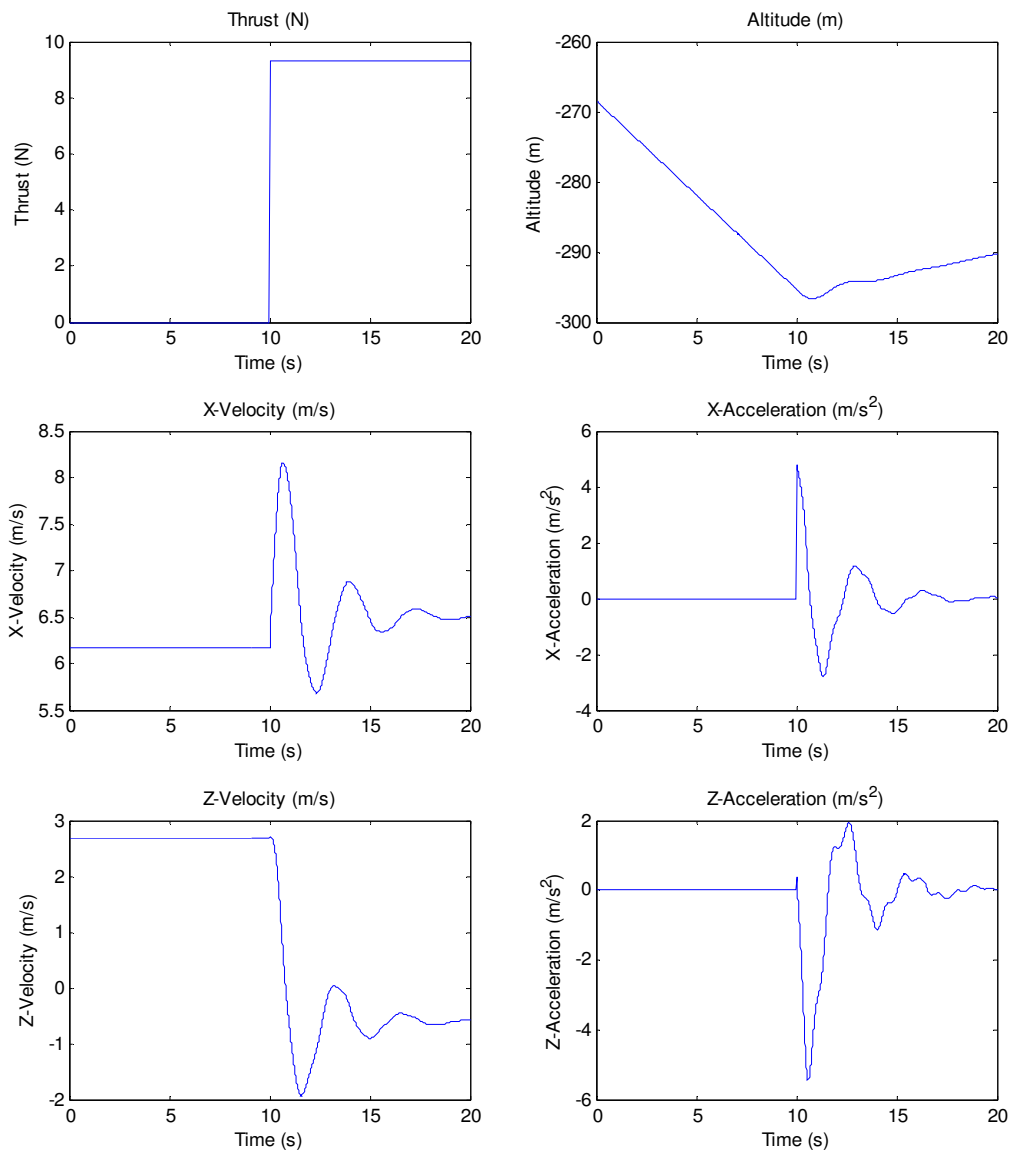
## Appendix A

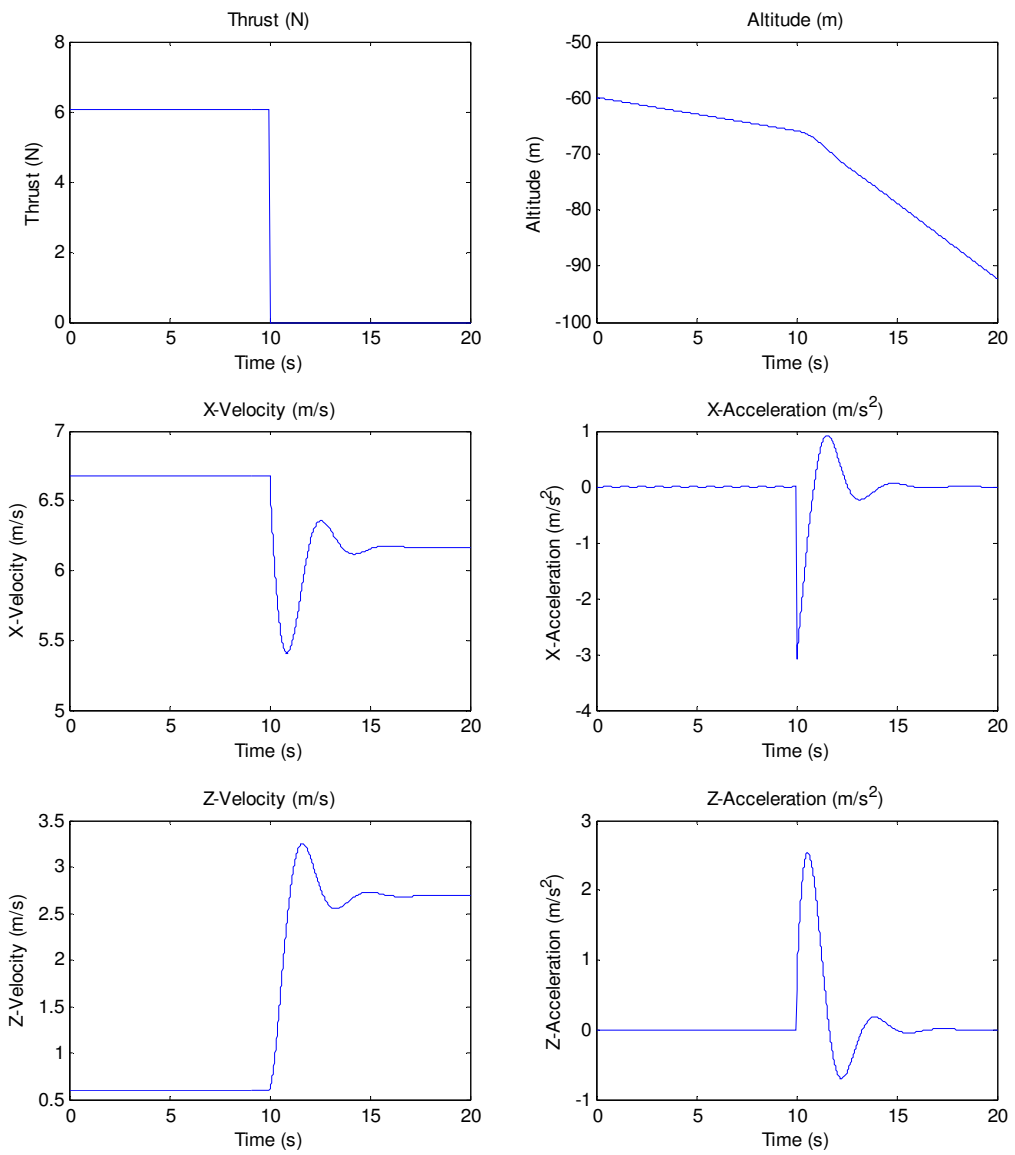
### Simulated Thrust Step Response Plots

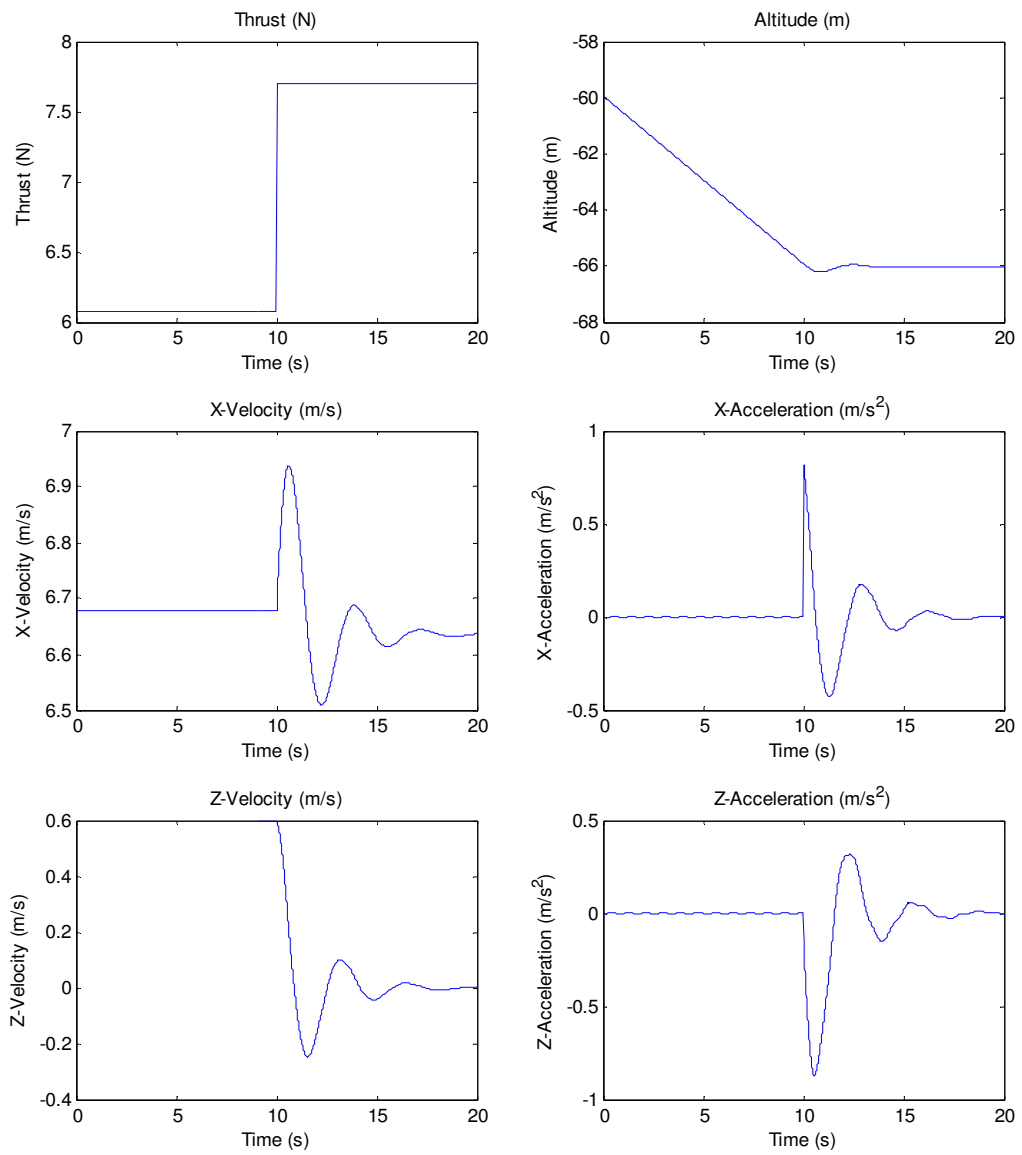
Various thrust step inputs between the values of 0, 6.08, 7.7, and 9.31 N

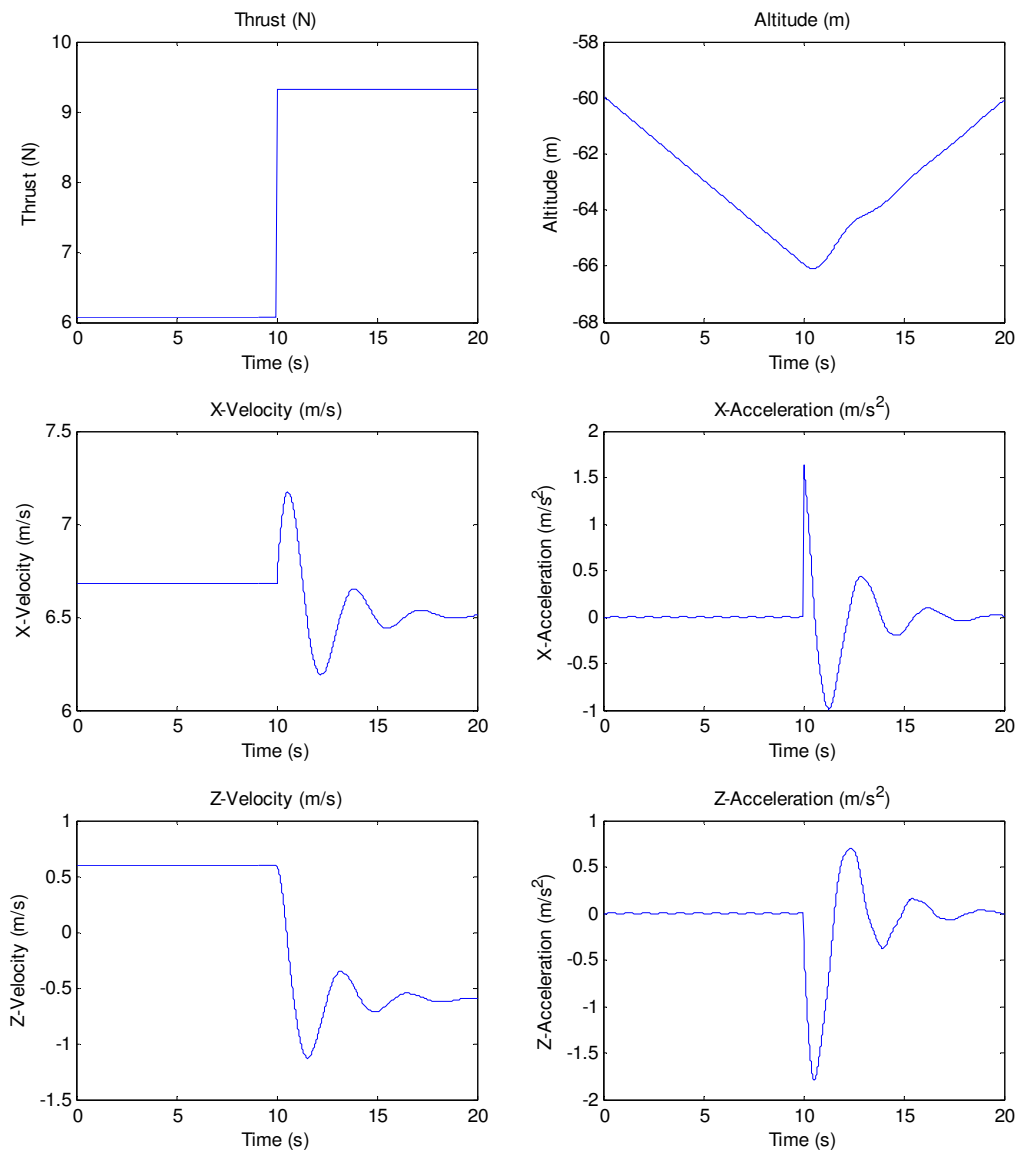


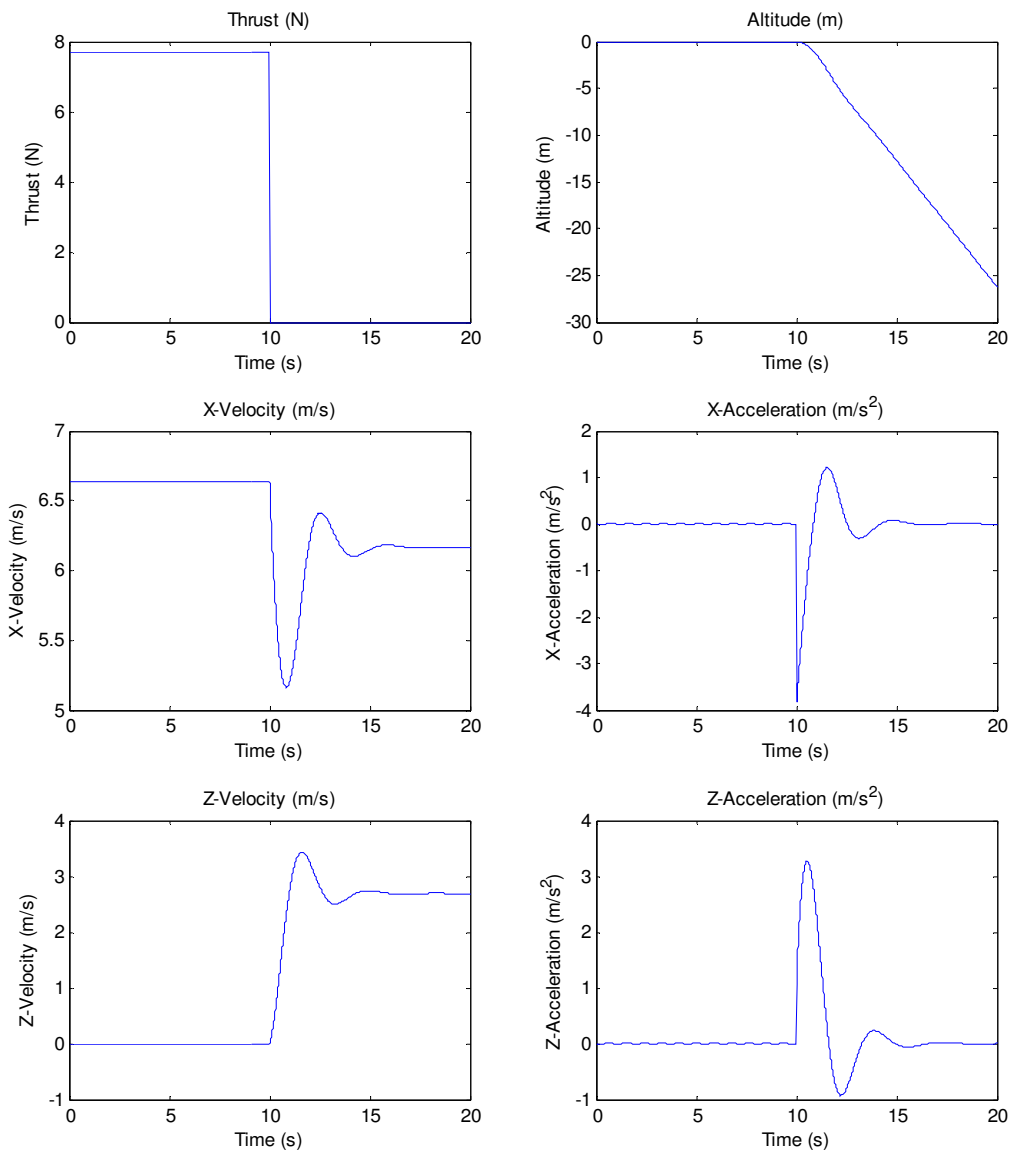


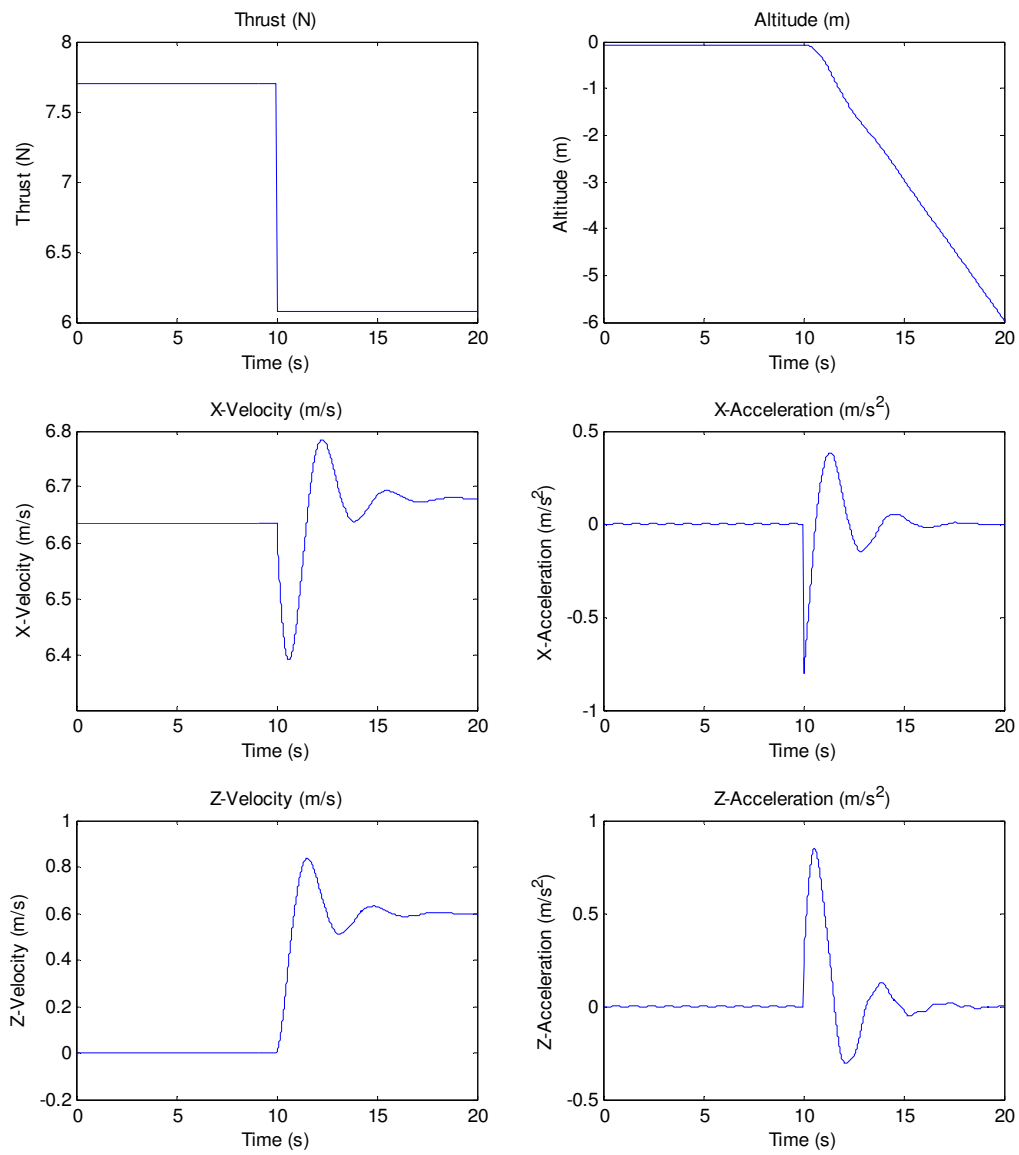


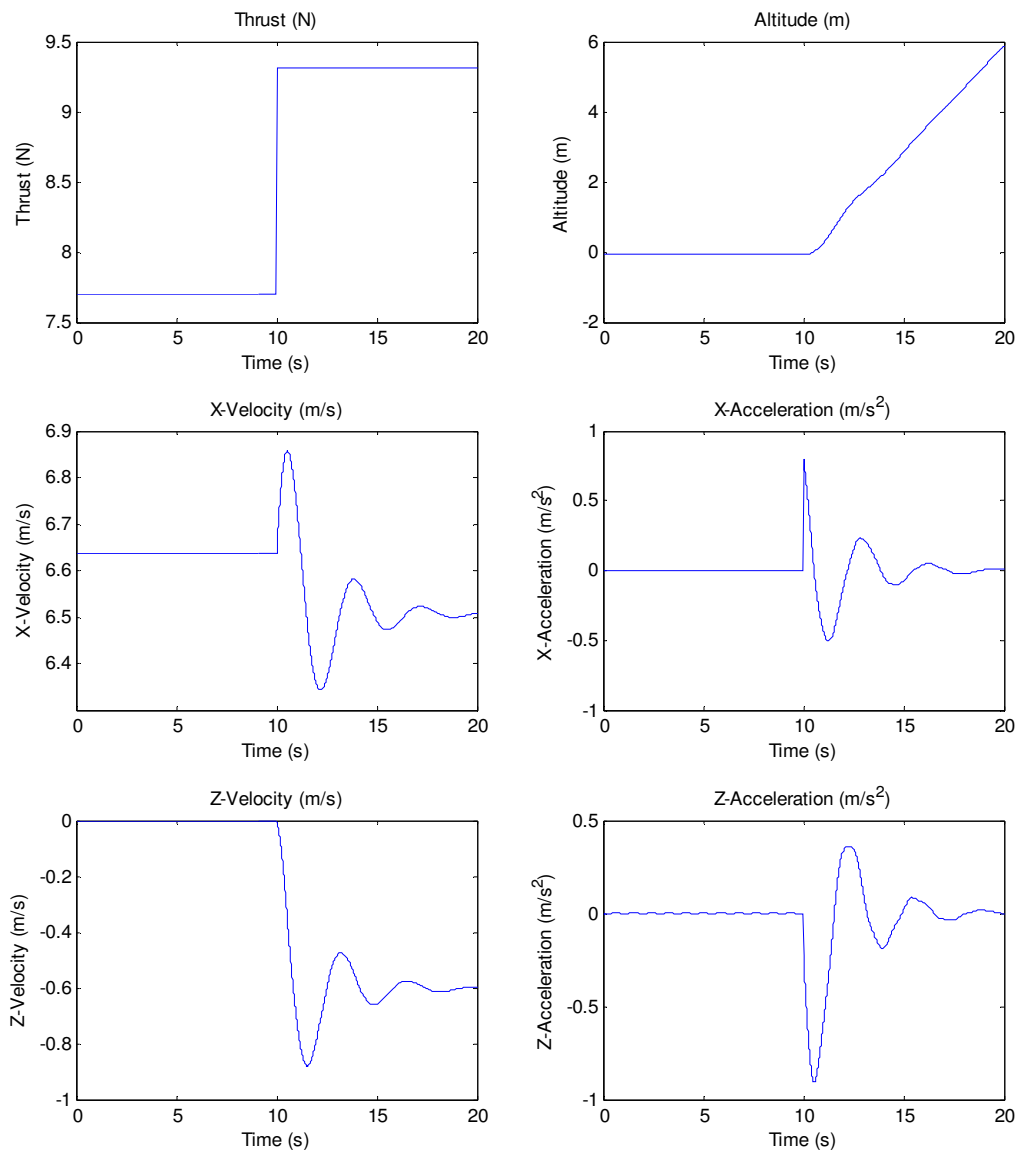


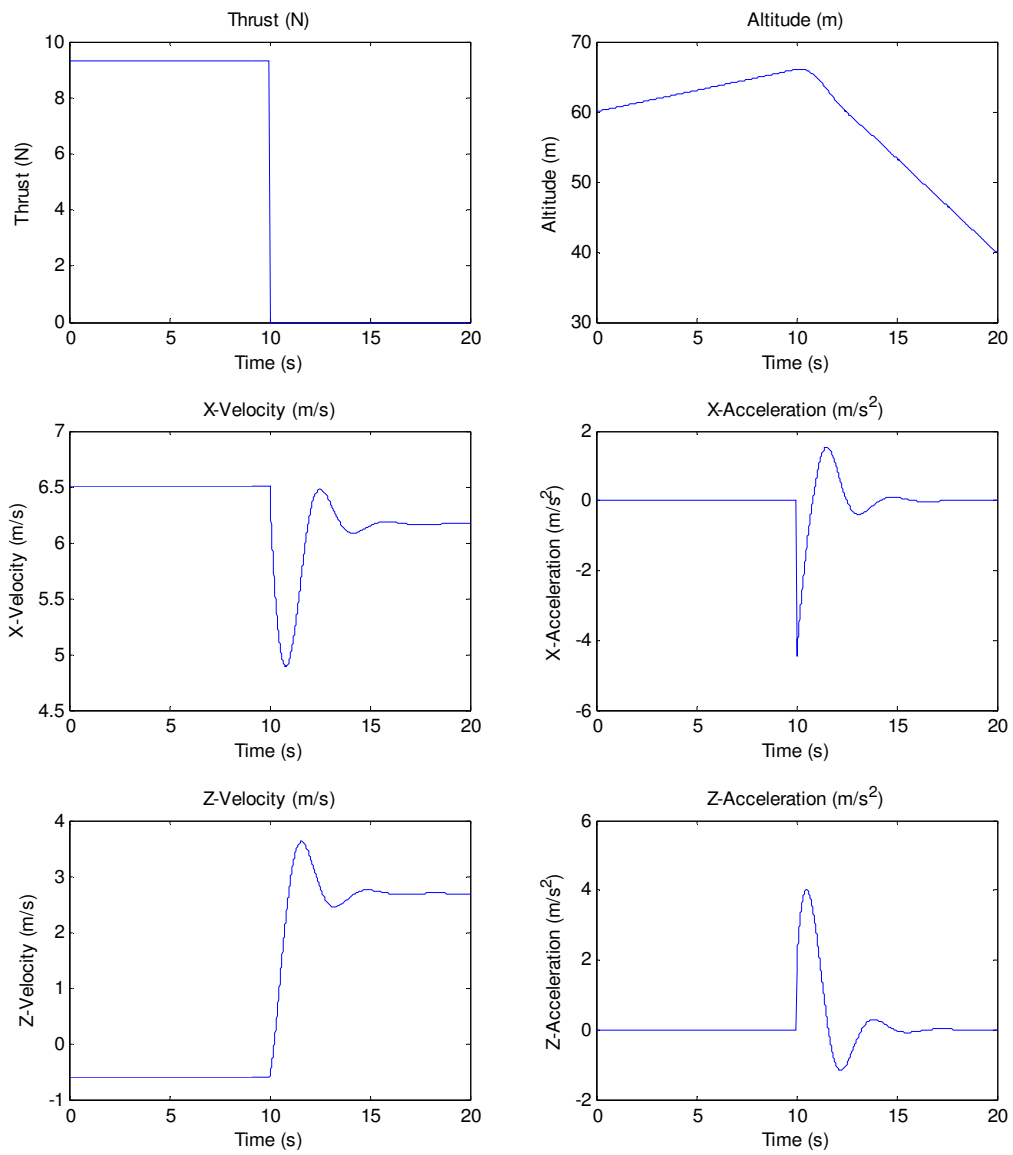


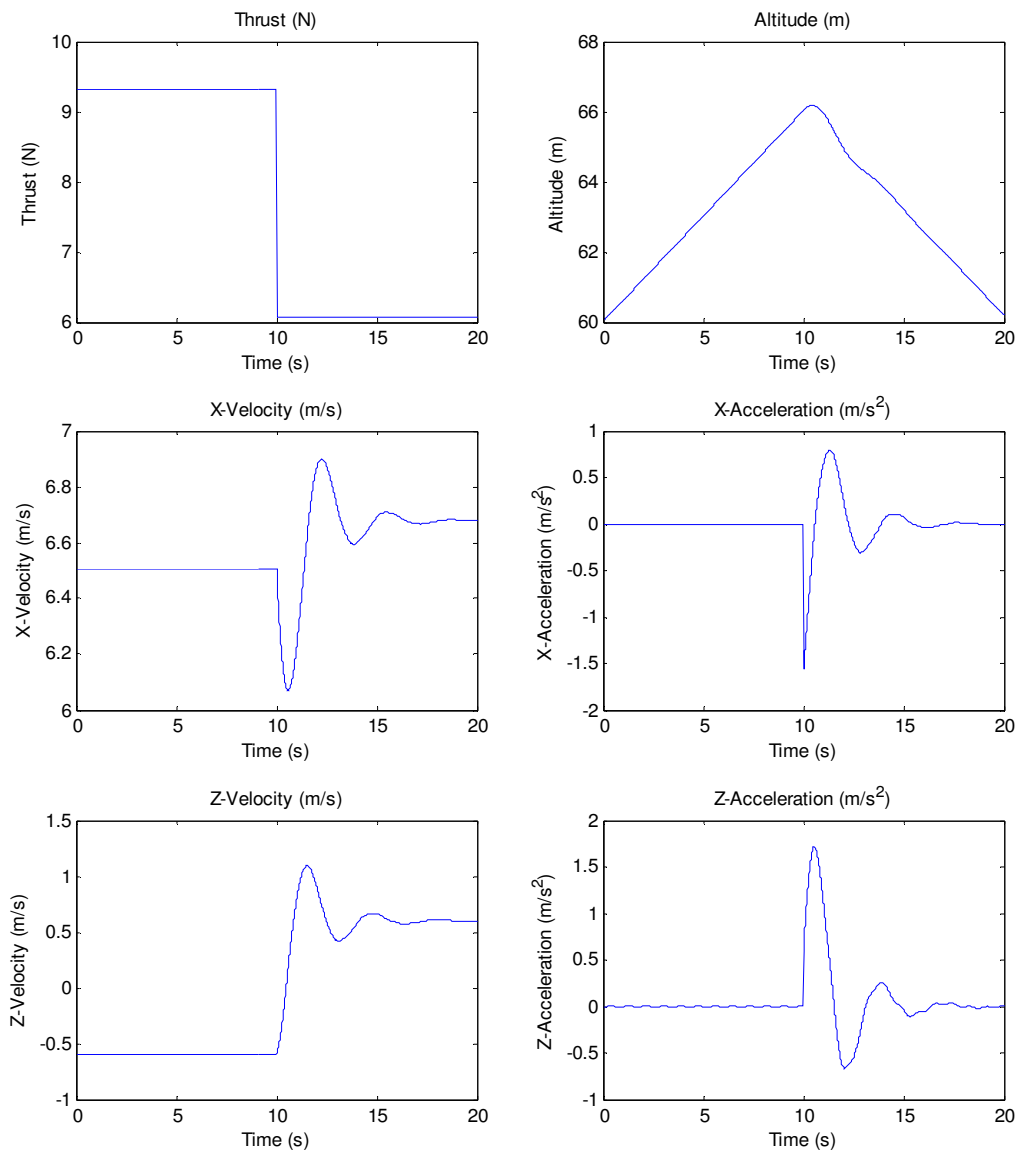


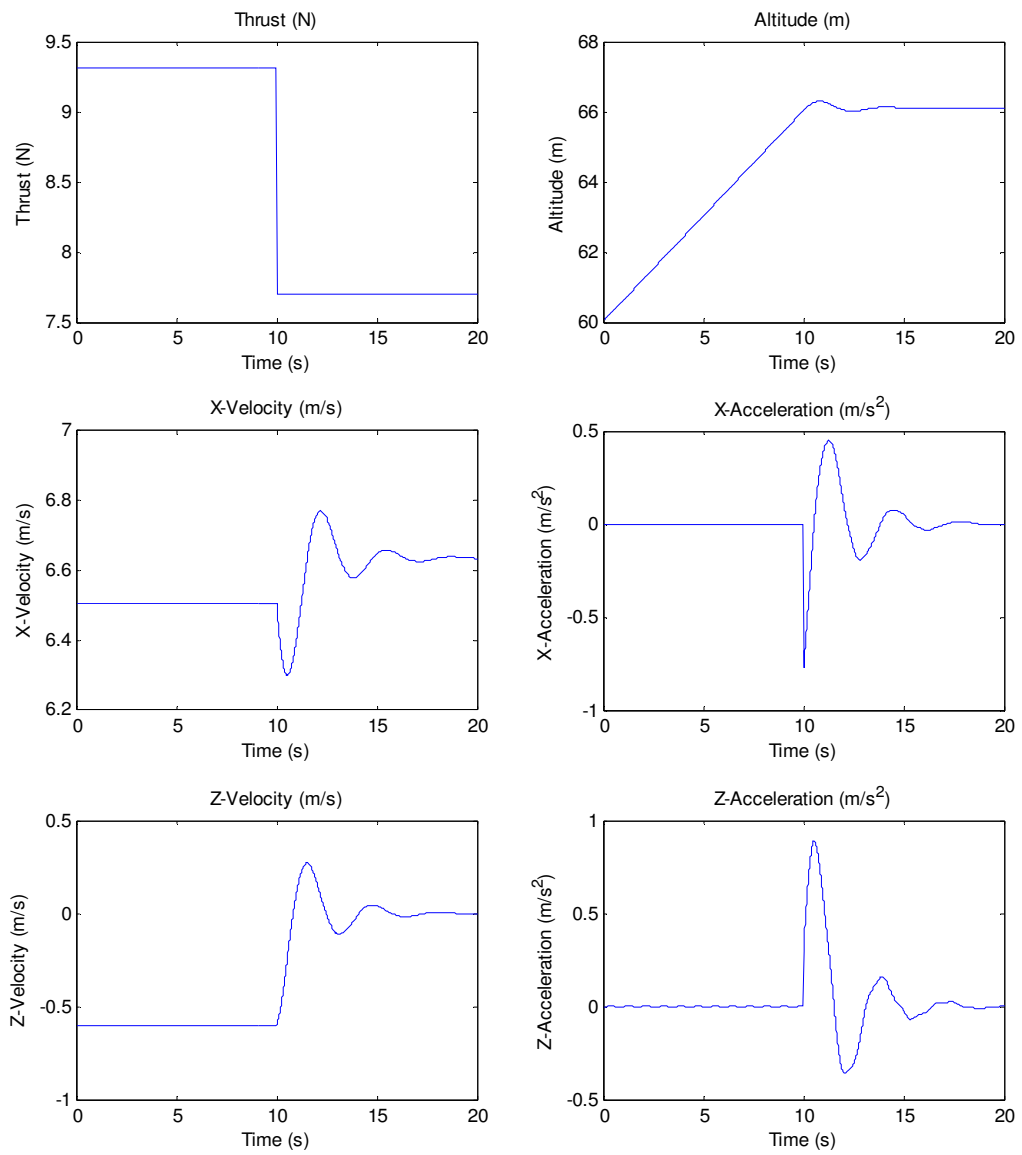












## Appendix B

### Experimental Thrust Step Response Plots

Time (s) shown on the horizontal axis

Vertical axis values and units shown in chart inlay titles

